UNIVERSITY OF CALIFORNIA SAN DIEGO

Topological Physics in Real and Reciprocal Space: Investigations in Electromagnetics

A dissertation submitted in partial satisfaction of the
requirements for the degree
Doctor of Philosophy

in

Electrical Engineering (Applied Electromagnetics)

by

Robert Joseph Benton Davis

Committee in charge:

Professor Daniel F. Sievenpiper, Chair
Professor Prabhakar R. Bandaru
Professor Michael M. Fogler
Professor Zhaowei Liu
Professor Yizhuang You

2023

The dissertation of Robert Joseph Benton Davis is approved, and it is acceptable in quality and form for publication on microfilm and electronically.

University of California San Diego

2023

DEDICATION

To my parents, whose limitless support has allowed my dreams to soar,

and to Nhi, whose smile makes a thousand miles feel like single step

EPIGRAPH

My fingers Emit sparks of fire with Expectation of my future labours

—William Blake, 1800

TABLE OF CONTENTS

LIST OF FIGURES

LIST OF TABLES

ACKNOWLEDGEMENTS

The greatest lesson I have learned from my time at UCSD is that nothing gets done in a vacuum. Theories are built on others, experiments performed with established tools, and research culminated by the collective effort of many people. Bernard of Chartres had the good fortune to coin the defining phrase of the Great Conversation[1], and the giants scholars perch on only grow with time.

My first thanks goes to my Chair, Professor Dan Sievenpiper. His interest and intuitive understanding of many complex physical phenomena inspired me to push the limits of what I knew far beyond anything I had expected. Likewise, I have come to strongly appreciate the value in stripping down the jargon and explaining topics in as easy way as possible, which, I hope, comes across in the pages here. I would like to thank my committee for their input and support. Professor Bandaru's expert and careful reading of many publications I've co-authored with him have sharped much of my eye for detail, always seeking for technical precision. From Professor You's courses I learned much of the theoretical underpinnings of several projects presented here, and I thank him for his excellent teaching. Professors Liu and Fogler have likewise provided helpful technical advice, and I appreciate their time and ideas.

Anyone that has spoken to me about my research knows I value collaboration, and in this regard I am especially grateful to my many colleagues here at UCSD. Dr. Dia'aaladin Bisharat, whose early help in my PhD was invaluable and helped to grow my confidence as a researcher. Prof. Zhixia Xu likewise gave me many opportunities when I was just starting. To Dr. Yun Zhou, I owe thanks for listening to my endless theoretical ideas and helping to chisel them into something that can actually be used. Outside of research, the conversations we've had have been a highlight of my time in San Diego (many 11 minute acoustic measurements in a row made for good times to chat!). To Dr. Sara Kandil, my desk neighbor, philosophical interlocutor, and all-around great friend and labmate, I likewise owe a debt of gratitude. Dr. Shreya Singh, I thank

[1] A good half century and change before the venerable Sir Isaac

you for always being a friend to talk to; your help and advice I have always treasured.

To Dr. Matt Smith, Dr. Kyle Thackston, and Dr. Jiyeon Lee, thank you all for being great lab elders and encouraging us to have events together. To Xiaozhen Yang and Erda Wen, thank you both for your wealth of expertise in many technical topics, not to mention your most excellent cooking. To Feng Li, resident plasma specialist *par excellence*, I'll extend a special thanks for helping share in the innumerable projects and technical impedimenta that research naturally gives rise to.

Beyond the sphere of the second floor of Jacobs Hall, I've likewise had the pleasure to discuss research with many colleagues in and out of UCSD, the echo of which can be seen throughout these pages. Varun Khurana and Ryan Mike, your patience and mathematical insights gave me the sounding board I needed to solve a number of problems. Zach Burns and Luke Herman, I've greatly enjoyed our wide ranging chats, as well as the wide range of waves caught. Nick Pfeufer, who has the distinction of being my longest-running academic collaborator, I thank for all your friendship.

None of the work presented here would have been possible without the endless support of my friends and family. My friends in California, Colorado, and beyond, thank you all for your camaraderie and continuing support through all these years. To Jeff Cavaliere, thank you for getting me in the best shape of my life. My parents instilled in me the desire to learn, to be curious, and to play a positive role on those around me, for which I'm forever grateful. Likewise, my sisters and family, near and far, have kept me grounded and always happy to be where I am, wherever the road may lead. Finally, to the love of my life, and the one who been with me for every leg of the journey, Nhi Phan: it took some time, but I'll see you soon. Just one step to go.

The material in this dissertation is based on the following papers which are either published or preparation for publication:

Chapter 1 and Chapter 2 are based on the following paper: D. J. Bisharat, R. J. Davis, Y. Zhou, P. R. Bandaru, and D. F. Sievenpiper, "Photonic Topological Insulators: A Beginner's

Introduction [Electromagnetic Perspectives]," *IEEE Antennas and Propagation Magazine*, vol. 63, no. 3. The dissertation author was the primary author of this material.

Chapter 3 is based on and is mostly a reprint of the following paper: R. J. Davis, D. J. Bisharat, and D. F. Sievenpiper, "Classical-to-topological transmission line couplers", *Appl. Phys. Lett*., vol. 118, no. 13, p. 131102, (2021). The dissertation author was the primary author of this material.

Chapter 4 is based on and is mostly a reprint of the following papers: R. J. Davis, D. J. Bisharat, and D. F. Sievenpiper, "Spin-Type Photonic Topological Insulators on a Rhombic Lattice" *In Preparation*, 2023; R. J. Davis, and D. F. Sievenpiper, "Robust Microwave Transport via Nontrivial Duality-Based Rhombic Unit Cells," in 2021 IEEE International Symposium on Antennas and Propagation and USNC-URSI Radio Science Meeting (APS/URSI) 619–620 (2021). The dissertation author was the primary author of this material.

Chapter 5 is based on and is mostly a reprint of the following paper: R. J. Davis, Y. Zhou, D. J. Bisharat, P. R. Bandaru, and D. F. Sievenpiper, "Topologically protected edge states in triangular lattices", *Phys. Rev. B* 106, 165403 (2022). The dissertation author was the primary author of this material.

Chapter 6 is based on the following paper: Y. Zhou, R. J. Davis, L. Chen, E. Wen, P. R. Bandaru, and D. F. Sievenpiper. "Helical Phononic Modes Induced by a Screw Dislocation". *In preparation*, 2023. The dissertation author was the primary author of this material.

Chapter 7 is based on the following paper: R. J. Davis, S. Singh, D. J. Bisharat, and D. F. Sievenpiper, "Topological Defects with Both Real and Reciprocal Space Signatures," *In preparation*, 2023. The dissertation author was the primary author of this material.

All material is used with permission by the co-authors.

VITA

2018	B. S. in Electrical Engineering, University of Colorado Boulder
2020	M. S. in Electrical Engineering (Applied Electromagnetics), University of California San Diego
2023	Ph. D. in Electrical Engineering (Applied Electromagnetics), University of California San Diego

PUBLICATIONS

R. J. Davis, S. Singh, D. J. Bisharat, and D. F. Sievenpiper, "Topological Defects with Both Real and Reciprocal Space Signatures," *In preparation*, 2023

R. J. Davis, D. J. Bisharat, and D. F. Sievenpiper, "Spin-Type Photonic Topological Insulators on a Rhombic Lattice" *In Preparation*, 2023

Y. Zhou, **R. J. Davis**, L. Chen, E. Wen, P. R. Bandaru, and D. F. Sievenpiper. "Helical Phononic Modes Induced by a Screw Dislocation". *In preparation*, 2023

R. J. Davis, A. Pal, D. F. Sievenpiper, "The Tight-Binding Method In Electromagnetics and Acoustics," *In Preparation*, 2023

Y. Zhou, N. Zhang, D. J. Bisharat, **R. J. Davis**, Z. Zhang, J. Friend, P. R. Bandaru, and D. F. Sievenpiper. "On-chip unidirectional waveguiding for surface acoustic waves along a defect line in a triangular lattice". *Phys. Rev. Appl.* 19, 024053 (2023)

F. Li, **R. J. Davis**, S. M. Kandil, and D. F. Sievenpiper, "Electromagnetic Non-Reciprocity in Magnetized Plasma Circular," *Phys. Rev. Appl.* 19, 024053 (2023)

R. J. Davis, Y. Zhou, D. J. Bisharat, P. R. Bandaru, and D. F. Sievenpiper, "Topologically protected edge states in triangular lattices", *Phys. Rev. B* 106, 165403 (2022)

E. Wen, D. J. Bisharat, **R. J. Davis**, X. Yang, and D. F. Sievenpiper, "Designing Topological Defect Lines Protected by Gauge-Dependent Symmetry Indicators," *Phys. Rev. Applied*, vol. 17, no. 6, p. 064008, (2022)

R. J. Davis, and D. F. Sievenpiper, "Robust Microwave Transport via Nontrivial Duality-Based Rhombic Unit Cells," in 2021 IEEE International Symposium on Antennas and Propagation and USNC-URSI Radio Science Meeting (APS/URSI) 619–620 (2021).

S. Singh, **R. J. Davis**, D. J. Bisharat, J. Lee, S. M. Kandil, E. Wen, X. Yang, Y. Zhou, P. R. Bandaru, and D. F. Sievenpiper, "Advances in metasurfaces: topology, chirality, patterning, and time modulation," *IEEE Antennas and Propagation Magazine* 2–14 (2021)

Z. Xu, J. Chang, S. Fang, Q. Zhang, **R. J. Davis**, D. F. Sievenpiper, T. J. Cui, "Line Waves Existing at Junctions of Dual-Impedance Metasurfaces", *ACS Photonics*, (2021)

R. J. Davis, D. J. Bisharat, and D. F. Sievenpiper, "Classical-to-topological transmission line couplers", *Appl. Phys. Lett.*, vol. 118, no. 13, p. 131102, (2021)

D. J. Bisharat, **R. J. Davis**, Y. Zhou, P. R. Bandaru, and D. F. Sievenpiper, "Photonic Topological Insulators: A Beginner's Introduction [Electromagnetic Perspectives]," *IEEE Antennas and Propagation Magazine*, vol. 63, no. 3

R. J. Davis, D. J. Bisharat, and D. F. Sievenpiper, "Efficient Transition from a Traditional Planar Transmission Line to a Topological Line Wave," in 2020 IEEE International Symposium on Antennas and Propagation and North American Radio Science Meeting, Jul. 2020, pp. 757–758.

Z. Xu, X. Kong, **R. J. Davis**, D. F. Bisharat, Y. Zhou, X. Yin, D. F. Sievenpiper, "Topological valley transport under long-range amorphous deformation", *Phys. Rev. Research* 2, 013209 (2020)

Z. Xu, J. Shi, **R. J. Davis**, X. Yin, and D. F. Sievenpiper, "Rainbow Trapping with Long Oscillation Lifetimes in Gradient Magnetoinductive Metasurfaces", *Phys. Rev. Applied* 12, 024043 (2019)

A. J. Gasiewski, A. Heymsfield, K. N. Frey, **R. J. Davis**, J. Rapp, A. Bansemer, T. Coon, R. Folsom, N. Pfeufer, and J. Kalloor, "Cloud Forecasting and 3-D Radiative Transfer Model Validation using Citizen-Sourced Imagery," Presented at the 2017 Fall Meeting, AGU, New Orleans, LA, 11-15 Dec.

ABSTRACT OF THE DISSERTATION

Topological Physics in Real and Reciprocal Space: Investigations in Electromagnetics

by

Robert Joseph Benton Davis

Doctor of Philosophy in Electrical Engineering (Applied Electromagnetics)

University of California San Diego, 2023

Professor Daniel F. Sievenpiper, Chair

The interaction between symmetry and topology is deep, and at the heart of both are the dual domains of real and reciprocal space. This dissertation aims to explore and explain the effects that symmetry has on topological phases of matter from both perspectives. To make these problems amenable to calculation and experiment, the platform of periodic engineered media, including photonic and phononic crystals, have been used. They provide a rich and highly efficient means of probing the different behaviors that different topological aspects can have on systems with given sets of symmetries.

Chapter 1

Introduction

Since the beginnings of quantum theory in the 1930s, a cornerstone of condensed matter physics has been the use of reciprocal space. Natural periodicity of solids combined with Bloch's theorem provide an elegant and computationally efficient means of studying materials via band theory in k-space. However, work on the quantum Hall effect and the development of topological physics [1] has revealed the inadequacy of purely reciprocal ideas. No longer is it possible to extract all useful phase information from the eigenvalue-based band structure; information about the the eigen*functions* themselves has become paramount. More recent developments have shown another possibility: information in *real* space can have a profound influence on the properties of systems.

A parallel advancement, largely born out of the landmark work of Kane and Mele on the quantum spin Hall effect in 2005 [2], has been that of topological models constructed in classical wave systems, like electromagnetics and acoustics [3]. The main advantage of these platforms has been their ease of experiment versus the true condensed matter systems. They also reveal that the ideas of topology itself are not limited to purely quantum systems [4]. Furthermore, they allow for a much simpler design to investigate the basic principles of the theory, with greater control over parameters. The advances in finite element method-based full-wave solvers have

eased the difficulty of verifying theory as well.

Much the same way photonic crystals (PhCs) applied the ideas of solid-state physics to photons [5], i.e. electromagnetic waves, the new field of photonic topological insulators [6] (PTIs) finds its origins in the world of electronic systems. In electronic topological insulators (TIs), electrons propagate along certain directions only on the exterior of the system. This explains part of the name: it is an "insulator" insomuch as it acts like a regular electrical insulator within the bulk of a material. "Topological," on the other hand, comes from the global topology of their energy band structure, since it can be categorized by an integer (the "topological invariant") that does not depend on the fine details of the system. The occurrence of electrical current on the surface of TIs—and how it responds to changes in energy—is credited to this topological invariant rather than minor changes to the surface, as in ordinary materials.

TIs found their start in the 1980s with the discovery of the quantum Hall effect (QHE) in a two-dimensional electron gas when subjected to periodic potentials and external magnetic fields [7, 8]. As in the normal Hall effect, applying a magnetic field causes the electrons to spin in cyclotron orbits, with their frequency being determined by the strength of the B field. When the material is strongly confined to 2D and cooled to very low temperatures, the quantization of the energy of these orbits becomes relevant, with the difference between the allowed energies becoming very large as the field strength increases. When the strength of the B field varies enough to permit or remove an energy level, there will be a sudden jump in the transverse conductivity by an exact multiple of fundamental constants. Hence, the QHE shows that conductivity is fundamentally discrete [9]. Importantly, it was found [10] that this discrete behavior could be explained by a special phase (called the geometric, or Berry phase, detailed in the next chapter) that each electron accumulates as it orbits in cyclotron motion in reciprocal (k) space.

How does topology relate to this? As it turns out, the discrete nature of the conductance is highly robust to deformations to the bulk of the material, and it can be shown that the added geometric phase responsible for the quantization is tied directly to the mathematical framework

of topological invariants [7, 10, 11]. This has some important consequences: it gives us a simple means to classify materials (i.e., bandgap materials) by calculating their topological invariant (which is a property of the bulk material), and it results in the technologically useful effects that topological insulators offer.

Materials that have an invariant of zero are "trivial," and act the same as an ordinary material. If the invariant is nonzero, however, then the effects of the geometric phase become relevant, and "non-trivial" effects can be observed. One of the most startling effects is what happens at the edge between a non-trivial material and a trivial material (or another non-trivial material with a different invariant), where a highly robust transport mode can exist [9]. These special modes, called edge modes, exist within the bandgap of the non-trivial material, and can be explained by the sudden change in the invariant across the boundary (e.g., going from 1 to 0). Even more remarkable is that electrons moving along these boundaries must do so in one direction only, with no possibility of scattering back in the other direction [1]. These edge modes are the corollary of the quantization of conductivity in the QHE.

In repeated experiments these edge states are observed regardless of the impurities in different material samples [1]. Since the invariant is resistant to a wide range of distortions to the material, the edge states are said to be topologically "protected," guaranteed to exist so long as the invariant stays the same [9]. This is of technological importance due to the potential to reduce power consumption by eliminating sources of loss, as well as simplify manufacturing by increasing defect tolerances. These discoveries led to the Nobel Prize in Physics being awarded to Thouless, Haldane, and Kosterlitz in 2016.

These systems with topological behavior are a consequence of the wave nature of the electrons, not specifically their quantum interactions [4]. As a result, it is possible to construct classical wave systems with analogous properties to their electronic counterparts. This opens the door to a vast range of theoretical proposals and experimental demonstrations. Replacing the electron with a photon (along with a reinterpretation of some quantities) we arrive at PTIs, which

demonstrate many of the same features of TIs and are the primary subject of this dissertation. However, other classical wave systems, including phononics [12] (considered in Chapter 6), mechanical oscillators [13], and a number of other easily engineered platforms are possible.

In the following chapters, we will examine a range of phenomena that demonstrate topological features in both real space (periodic systems), as well as others that demand analysis in real space. Moreover, we will see how, using these engineered platforms, we can interrogate the physical consequences that symmetries have on the topological character of different systems. Crystallographic symmetries in 2- and 3-D will be used, as well as the internal symmetries of time reversal, spin, and electromagnetic duality will be of relevance, as will more subtle issues of gauge.

In Chapter 2, a brief overview of the mathematical tools and methods used throughout the dissertation is give. This is to both prepare the unfamiliar reader as well as provide clarity to the use of terms used, and may be skipped or consulted as needed.

Chapter 3, an efficient means of coupling into a classical, continuous electromagnetic transmission line to a topological line wave structure is demonstrated and analyzed. The PTI structure employed here will be used extensively throughout later chapters, and so it is recommended to at least read the introductory material of this chapter before moving on.

Chapter 4 explores how the reduction of symmetry of the spin duality structure used in Chapter 3 influences the reciprocal space topology. This chapter begins a greater emphasis on the use of the mathematical methods of Chapter 2.

Chapter 5 shows how simple triangular lattices can host topologically robust edge states under certain symmetry settings. This chapter briefly demonstrates this in a photonic crystal, but the emphasis here is on the underlying physics of gauge dependence and crystallographic symmetry.

Chapter 6 provides a brief introduction to the broader class of symmetry-based methods of classifying matter, before analyzing a specific example in phononics.

Chapter 7 presents a detailed analysis of a model that completely destroys all symmetry, and must instead be understood using methods based in real space alone. The connections between the internal symmetry-based topology of the base structure (identical to that in Chapter 3) and the purely real space topology of the geometry are shown using numerical tools, and measurements are presented.

Finally, Chapter 8 gives a summary and discussion of the major results.

This chapter is partially based on the following paper: D. J. Bisharat, R. J. Davis, Y. Zhou, P. R. Bandaru, and D. F. Sievenpiper, "Photonic Topological Insulators: A Beginner's Introduction [Electromagnetic Perspectives]," *IEEE Antennas and Propagation Magazine*, vol. 63, no. 3. The dissertation author was the primary author of this material.

Chapter 2

Mathematical Preliminaries

This dissertation employs a wide range of mathematical tools and formalisms, some of which may be unfamiliar to readers from different backgrounds. As they often are used in the literature without any prior elaboration to the uninitiated, following the discussion in research papers can be challenging, especially for cases where a tool from one area (condensed matter physics, for example) is employed to another (RF engineering, for example). Throughout the dissertation these concepts will be invoked when needed, but for the sake of brevity will be minimal in the main text. To aid the reader, a more detailed discussion is provided below, which can be skipped or referenced as desired.

2.1 The Tight Binding Method

In many of the projects covered by this dissertation there has been a need to employ the so-called tight binding (TB) method. Originally developed for electronic systems [14], it has nevertheless proven very useful in classical wave systems, as it allows for rapid calculations with analytic forms. Likewise, it permits more direct exploration of symmetry properties of physical systems. This section will detail the basic computational aspects relevant to the topics discussed later. Interested readers can consult a number of helpful textbooks [15, 16].

2.1.1 General Statement

The tight binding method describes the behavior of a particle hopping along a lattice between discrete sites. In the original formulation the particle is considered to be an electron, and the sites are atomic sites and orbitals, but this physical framework is actually not strictly needed. Instead, we may abstract away the assumed physics and begin with the math.

First, for a general eigenvalue problem describing a wave-like phenomenon

$$H\psi = E\psi, \tag{2.1}$$

we have an abstract operator H (termed the Hamiltonian), which has eigenfunctions ψ with corresponding eigenvalues E. Note that the exact representation of H doesn't need to be specified here (e.g., it could be the Schrodinger operator, or the Maxwell operator, or a host of others, so long as it involves the mechanics of wave motion[1]). If we assume periodicity of the Hamiltonian, or, in physics terms, the potential is periodic,

$$V(\mathbf{r}+\mathbf{R}) = V(\mathbf{r}), \tag{2.2}$$

for some vector $\mathbf{R}$, Bloch's theorem tells us that the form of the wavefunctions must also be periodic in the same way:

$$\psi(\mathbf{r}+\mathbf{R}) = \psi(\mathbf{r}). \tag{2.3}$$

This statement leads to the general form of the wavefunction, which is the usual statement of Bloch's theorem:

$$\psi(\mathbf{r}) = e^{i\mathbf{k}\cdot\mathbf{r}}u(\mathbf{r}), \tag{2.4}$$

where $u(\mathbf{r})$ is a function that is periodic with the same period as the potential $V(\mathbf{r})$. We often term

[1] Strictly speaking, we can limit the discussion to systems obeying Hill's equation, which takes the general form $\frac{d^2y}{dt^2} + f(t)y = 0$.

the function $u(\mathbf{r})$ the *cell periodic* part of the wavefunction, and frequently drop the exponential planewave prefactor, as it always has the same form.

To be more notationally complete, we can represent the wavefunction ψ as the so-called Bloch state, given as

$$\psi_{\mathbf{k}} = \frac{1}{\sqrt{N}} \sum_{\mathbf{R},j} c_j(\mathbf{k}) e^{\mathbf{k}\cdot(\mathbf{R}+\mathbf{a}_j)}, \tag{2.5}$$

, where we have introduced the the crystal momentum $\mathbf{k}$, Fourier expansion coefficients c_j, lattice point vector $\mathbf{a}_j$, and system size N. These states can be solved for a given Hamiltonian a number of ways, and contain much useful information. Returning to the physics, the above states represent physical solutions of the underlying system described by H under the assumed wave and periodic conditions. If we can derive a suitable Hamiltonian, we can examine the behavior of the Bloch states as a function of crystal momentum. Atomic sites and orbital information can be encoded, as well as added degrees of freedom for spin.

However, we'll point out here that Eq. (2.5), while general, is far removed from how the method is used in many applications. As we will see, the most useful formulation abstracts away most of the complexities of the prior discussion, and instead relies upon simple matrix operations and definitions. This is most critical for the form that H takes, as the next section will show.

2.1.2 Computational Example

As a basic example, we can build a TB model of a square lattice using a basis of four atoms, with a single spinless particle at each atom. A sketch of this lattice is shown in Fig. 2.1.

Skipping the usual Bloch state analytical description, we can jump directly to the matrix

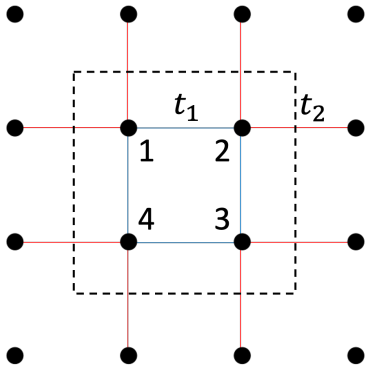

Figure 2.1: A square lattice, with the unit cell choice shown by the dashed lines. Sites are numbered clockwise, and there are two hopping strengths, t_1 and t_2, which correspond to the hopping within a given unit cell and those between unit cells, respectively.

definition, given as

$$H(k_x,k_y,t) = \begin{pmatrix} \delta & t_1+t_2e^{-ik_x} & 0 & t_1+t_2e^{ik_y} \\ t_1+t_2e^{ik_x} & \delta & t_1+t_2e^{ik_y} & 0 \\ 0 & t_1+t_2e^{-ik_y} & \delta & t_1+t_2e^{ik_x} \\ t_1+t_2e^{-ik_y} & 0 & t_1+t_2e^{-ik_x} & \delta \end{pmatrix} \tag{2.6}$$

The hopping amplitude t_1 determines the coupling strength between a given site and its nearest neighbor within the unit cell, t_2 between sites between unit cells, and k_x, k_y are the two reciprocal space directions, which coincide with the real space coordinate system of the figure. Note that we have chosen the period $a = 1$, which simplifies the terms without losing generality. We stress here that the above matrix form of H is not "the Hamiltonian" precisely, but is rather the Bloch Hamiltonian for the chosen basis. By writing it explicitly, we restrict our attention to the layout shown in Fig. 2.1. Moreover, we can see that the entire matrix can essentially be "read off" directly from the figure, each term simply representing the coupling between sites, including the periodic terms (the exponentials) to create periodic boundary conditions via Bloch's theorem. We may use this simple model to examine the bandstructure, calculate symmetries, and compute

many different topological features of interest, detailed in later sections.

2.1.3 Application to Classical Bosonic Systems

It is worth cautioning the reader of the application of TB models to photonics and other classical wave systems involving bosons in artificial crystals. Although the math is quite general, there are some restrictions on the applicability, and certain aspects that it cannot capture completely.

1. **Discreteness**: The lattice assumed by the TB method is inherently discrete. Particles live on infinitesimally small points of the atomic sites, and have zero physical extent. This is a reasonable enough approximation in electronic lattices where the electrons are tightly bound (hence the name ”tight binding”) to their atomic nuclei, but in the cases of photonics and phononics, this is often not the case. Electromagnetic fields are spatially spread out across the unit cell in a photonic crystal, as are acoustic displacement fields in a photonic lattice. The periodicity of the lattice makes Bloch's theorem valid, but the assumption that modes only exist at a lattice point is qualitatively different.

2. **Coupling**: The coupling mechanisms between lattice points is easy to obscure without sufficiently large TB models. This is readily seen in many basic platforms, like the triangular lattice studied later in this dissertation. In the bosonics case, there is a large bandgap for a triangular lattice of rods, whereas the equivalent basic TB mode is gapless. This is a natural consequence of the difference between the underlying ODEs being approximated.

3. **Degrees of Freedom**: Atomic systems are well described by atomic orbitals, which the TB method is custom made to use. The potential degrees of freedom (geometrical or otherwise) can be captured within the framework of the basis choice without much difficulty, provided enough parameters are specified. In the classical wave case, the geometrical freedom to warp the shape of the unit cell infinitesimally implies that the exact behavior can not be

exactly matched. General symmetries can be retained, but, unless a very large number of parameters are included, the eigenvalues and eigenfunctions will only be qualitatively matched to the genuine physical system.

2.2 Reciprocal Space Topological Invariant Calculations

A cornerstone of analysis methods of topological systems involves the use of the periodic functions in reciprocal space. These include the famed Chern number, as well as the more general phenomena of geometric phase and Berry curvatures. Many projects considered in this dissertation will make extensive use of these mathematical tools, which are detailed below.

2.2.1 Berryology: Berry Phase, Berry Connection, and Berry Curvature

Consider a lattice described by a general eigenvalue problem in momentum space,

$$H(k)\psi_n(k) = \lambda_n(k)\psi_n(k) \tag{2.7}$$

where $\lambda_n(k)$ is the eigenenergy and $\psi_n(k)$ is the normalized eigen wavefunction of $H(k)$ at each k for the nth band, which can be determined via Bloch's theorem. In the following, we will make use of the shorthand notation of inner product

$$\langle A(r)|B(r)\rangle \equiv \int A(r)^\dagger \cdot B(r)dr \tag{2.8}$$

to refer to integration of two (possibly vector) functions A and B over a variable r, with † denoting Hermitian conjugation. Hence, normalized in this case means $\langle\psi_n(k)|\psi_n(k)\rangle = 1$. Gradually changing the k along a given energy band will cause a phase accumulation associated with the slow evolution of $\psi_n(k)$. Under most cases when k returns back to where it started this accumulation will result in zero total phase, but special cases can arise where a non-zero phase is added. In the

literature this phase, the **geometric phase**, is referred to by the name **Berry phase**, specifically to recall Berry's formulation in quantum mechanics [17].

To calculate the total Berry phase, we need a means to add up the phase contributions from each small change to the wavefunction. The phase shift between two ϕ_n states infinitesimally separated by Δk can be represented by their inner product [18], expanded as a low-order Taylor series as

$$\langle \psi_n(k)|\psi_n(k+\Delta k)\rangle \approx 1+\Delta k\langle \psi_n(k)|\nabla_k|\psi_n(k)\rangle = \exp(-i\Delta k\cdot A_n(k)) \tag{2.9}$$

Here, we can see that $\Delta k\cdot A_n(k)$ is the phase shift over Δk, and $A_n(k)$ is the rate of change of the phase shift. $A_n(k)$ is called the **Berry connection**, or Berry vector potential,

$$A_n(k) = i\langle \psi_n(k)|\nabla_k|\psi_n(k)\rangle \tag{2.10}$$

Therefore, the Berry phase for the nth band is defined as the integral of $A_n(k)$ over some closed path l in k-space,

$$\phi_n = \oint_l d\mathbf{k}\cdot\mathbf{A}_n(\mathbf{k}) \tag{2.11}$$

The path l is simply a smooth curve of values over the BZ, such as the blue and red lines shown on the right half of Fig. 2.2. If we know what a given wavefunction looks like in the Brillouin zone, we could use the above to calculate the Berry phase for that path. However, there is a catch: the Berry connection $\mathbf{A}_n(\mathbf{k})$ is not uniquely defined. If a phase change $\xi(\mathbf{k})$ is added to the eigen wavefunction $\psi_n(\mathbf{k})$, where $\xi(\mathbf{k})$ is a periodic function with $\xi(\mathbf{k}_{end}) = \xi(\mathbf{k}_{begin}) + 2m\pi$, the new wavefunction $e^{i\xi(\mathbf{k})}\psi_n(\mathbf{k})$ is still an eigen wavefunction of $H(\mathbf{k})$. The Berry connection is then transformed as $\mathbf{A}_n(\mathbf{k}) \to \mathbf{A}_n(\mathbf{k}) - \frac{\partial}{\partial\mathbf{k}}\xi(\mathbf{k})$, where it changes its formula with different choice of

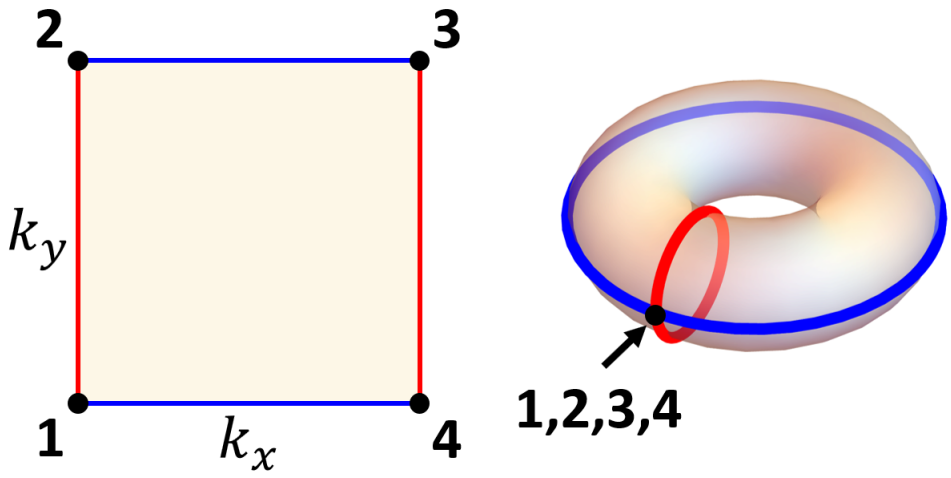

Figure 2.2: The Brillouin zone can be considered as a torus by taking each periodic boundary (red and blue in the figure) and connecting them together.

$\zeta(\mathbf{k})$. The Berry phase, on the other hand, is invariant modulo 2π,

$$\oint_l d\mathbf{k}\cdot\mathbf{A}_n(\mathbf{k}) \to \oint_l d\mathbf{k}\cdot\mathbf{A}_n(\mathbf{k}) - \oint_l \frac{\partial}{\partial\mathbf{k}}\zeta(\mathbf{k})d\mathbf{k} \tag{2.12}$$

$$\to \oint_l d\mathbf{k}\cdot\mathbf{A}_n(\mathbf{k}) - 2m\pi \tag{2.13}$$

This can also be understood qualitatively. As the wavevector k slowly travels around the loop of a band, the wavefunction $\psi(\mathbf{k})$ eventually returns to where it starts and picks up a phase of a multiple of 2π, with most systems picking up zero [19]. Since the Berry connection depends on how we setup the calculation, yet know that the Berry phase should not, it is helpful (especially for numerical purposes) to define a quantity that will be invariant to any arbitrary phase $\zeta(\mathbf{k})$ that we may add.

The **Berry curvature**, or Berry flux, a quantity that is invariant under such transformation, can be constructed by taking the curl the Berry connection,

$$\Omega_n(\mathbf{k}) = \nabla_n(\mathbf{k}) \times \mathbf{A}_n(\mathbf{k}) \tag{2.14}$$

Then, using Stokes' theorem, the Berry phase can be rewritten as the integral of the Berry curvature,

$$\phi_n = \int_S d^2\mathbf{k} \cdot \Omega_n(\mathbf{k}) \tag{2.15}$$

where the integration is over the surface bounded by the path l [16].

2.2.2 The Chern Number

Integration of the Berry curvature over the full BZ gives the "first" **Chern number**

$$C_n = \frac{1}{2\pi} \int_{BZ} d^2\mathbf{k}\Omega_n(\mathbf{k}). \tag{2.16}$$

It is often called the "first" or "magnetic" Chern number, to distinguish it from other formulations of the value.

2.2.3 The $\mathbb{Z}_2$ Invariant and the Spin Chern Number

For fermionic systems with time reversal symmetry and nonzero spin-orbit coupling, the so-called $\mathbb{Z}_2$ **invariant** takes many forms depending on symmetries, but one common formulation can be written as

$$(-1)^{\nu} = \prod_{a=1}^{N} \frac{Pf(w(\lambda_a))}{\sqrt{\det w(\lambda_a)}}, \tag{2.17}$$

where N denotes the number of time-reversal invariant momenta (4 for 2D systems and 8 for 3D), Pf denotes the *Pffafian*, $w(\lambda_a)$ is the overlap matrix between the Bloch states and their time reversed pairs. This definition is general, but is rather formidable to use, and so we will not make further use of it it here. However, we can reformulate the problem into a matrix of Chern numbers [20], which, without Rashba-like coupling terms, becomes a diagonal matrix of "**spin Chern numbers**", one per spin. Numerically, these can be calculated via Eq. (2.2.2) , where the Berry curvature is computed from the *spin-projected* periodic Bloch states. That is, we only compute

those eigenfunctions with a specific spin, ignoring the others. For TRS-invariant systems, the sum of the two spin Chern numbers will naturally equal zero, as required.

2.2.4 The Valley Chern Number

For many forms of system it is possible to generate a large build up of Berry curvature in the vicinity of degeneracies broken by some symmetry breaking. This is the case even for time-reversal symmetric and spinless systems, where all other curvature-related values are zero. To do so, we can compute the integral of the curvature in the vicinity of the Berry curvature at the two TRS-related points K/K' in the BZ, which have equal and opposite accumulation [21]. The resulting value is commonly called the **valley Chern number**.

2.2.5 Wilson Loops, Wannier Centers, and Charge Polarization

In this section we will primarily follow the preliminaries of [22], which has further details for the interested reader. For generic tight-binding Bloch Hamiltonian $H(\mathbf{k})$ with eigenstates $u_n^{\mathbf{k}}$ defined for band n, we first define the non-Abelian Berry[2] connection $\mathbf{A}$ as

$$\mathbf{A}_{mn}(\mathbf{k}) \equiv i\langle u_m^{\mathbf{k}} | \nabla_{\mathbf{k}} | u_n^{\mathbf{k}} \rangle. \tag{2.18}$$

The (continuum) **Wilson loop** can then be described a path ordered exponential

$$\mathcal{W}(l) = T \exp\left(-i \int_l d\mathbf{l} \cdot \mathbf{A}(\mathbf{k}) \right), \tag{2.19}$$

where l denotes a closed loop in reciprocal space and T denotes path-ordering. The eigenvalues of Eq. (2.19) encode the non-Abelian Berry phases of the Bloch bands considered. For calculation

[2]Note that Eq. (2.18) is nearly identical to Eq. (2.10), but with the difference of the subscripted band indices. In the non-Abelian formulation, we consider pairs of modes n and m, rather than just one, as in Eq. (2.10). This alteration is needed to cover cases where there are degeneracies.

purposes, we may determine the Berry phases of a specific TB model by defining a discrete version as

$$\theta(k_i) = -\mathrm{Im}\log\prod_j \det M^{k_i,k_j}. \tag{2.20}$$

Here we have introduced an overlap matrix M to handle cases of degeneracy, whose elements are defined as

$$M_{mn}^{k_i,k_j} = \langle u_m^{k_i,k_j} | u_n^{k_i,k_{j+1}} \rangle. \tag{2.21}$$

The result of computing Eq. (2.20) (normalized by 2π) is the location of the Wannier center for a given k_i.

2.3 Symmetry Indicators

A recent development in topological physics has been the introduction of a wide range of "symmetry indicators". These tools, though not topological invariants in the sense of the Chern number, provide an indication as to the classification of phases. They involve different formalisms, but in general these methods employ details of the symmetry of eigenstates of the system, hence the name. They are often substantially more computationally efficient than pure reciprocal tools, and can provide insight into the physical mechanisms governing the resulting nontrivial behavior.

2.3.1 Rotational Symmetry Indicators for 2D Systems

Computational Aspects of Symmetry Indicators for Tight-Binding Models

The symmetry indicator method employed in Chapter 5 has gained in popularity recently, but is often difficult to follow how authors make use of it, and there are few resources to assist those who wish to perform the calculations themselves. Various rigorous arguments and proofs for these methods can be found in e.g., [23]. This technique is computationally very efficient, as it

does not require diagonalization at all k points (like the Chern number), and less mathematically involved than methods like the $\mathbb{Z}_2$ invariant. This section aims to fill in the more numerical details involved in such calculations, and hopefully make clear what is being presented.

To begin with, for tight-binding models the first step is to calculate the eigenvectors of the Hamiltonian directly at the relevant HSPs of the BZ. For 2D models, this merely involves the diagonalization of at most 3 matrices (e.g., Γ, M, K for triangular and Γ, X, M for square lattices), giving eigenvectors $u_j(\Pi)$ for each HSP Π and band j.

The second step is to then compute the expectation value of the desired rotational operator when acting on each computed eigenvector. Construction of such operators is simple within the TB formalism, and are merely matrices that permute the given orbital sites. The eigenvalues of each rotational operator are always given as

$$\Pi_p^{(n)} = e^{2\pi i(p-1)/n}, \quad p = 1, 2, 3, \cdots, n \tag{2.22}$$

for an n-fold rotational operator. We therefore know in advance that the computation of the given symmetry indicators will involve counting up these values, and any computation that differs from them is likely an error (commonly noticed due to improper handling of degeneracies, which will be covered shortly, or a error, which is described in Sec. 5.7).

Computing the expectation for a single isolated band involves a simple inner product,

$$\langle \hat{r}_n^u(\Pi) \rangle = \langle u(\Pi) | \hat{r}_n | u(\Pi) \rangle. \tag{2.23}$$

In the above, $u(\Pi)$ denotes the eigenvector computed in the first step for the HSP Π, and $\hat{r}_n$ is the matrix representation of the rotational operator of order n, with the size of $\hat{r}_n$ being determined by the number of basis elements of the vectors.

The above equation will give one of the eigenvalues of $\hat{r}_n$, which may then be used for the later steps in computing the invariant. However, it is often the case, especially for more complex

bandstructures, that degeneracies occur the the HSPs in question. The resolution to this is to consider the overlap matrix formulation of Eq. (2.23), given as

$$S(\Pi) = \begin{pmatrix} \langle u_1(\Pi)|\hat{r}_n|u_2(\Pi)\rangle & \langle u_1(\Pi)|\hat{r}_n|u_3(\Pi)\rangle & \cdots & \langle u_1(\Pi)|\hat{r}_n|u_M(\Pi)\rangle \\ \langle u_2(\Pi)|\hat{r}_n|u_1(\Pi)\rangle & \ddots & & \vdots \\ \vdots & & & \\ \langle u_M(\Pi)|\hat{r}_n|u_1(\Pi)\rangle & \cdots & & \langle u_M(\Pi)|\hat{r}_n|u_M(\Pi)\rangle \end{pmatrix} \tag{2.24}$$

for a given manifold of M degenerate bands at HSP Π. The eigenvalues of this matrix provide the desired expectation values of the rotational operator.

Once the expectation values are computed, the final step is to count the number of each eigenvalue and subtract the number located at Γ, written in general as

$$[\Pi_p^{(n)}] = \#\Pi_p^{(n)} - \#\Gamma_p^{(n)} \tag{2.25}$$

This final step is less clear notationally, as indicated by the use of the # sign to mean "count the number of." The above is merely stating that to find the integer valued invariant element $[\Pi_p^{(n)}]$ for an n-fold rotation at HSP Π that has eigenvalue $\Pi_p^{(n)}$, we have to count the number of bands with that same eigenvalue at Π, count the number of bands with that eigenvalue at Γ, and subtract the two counts. Note that in doing so we are forced to decide where to set the Fermi level (or, to extend the discussion to bosonics, the desired frequency), which determines the number of bands we must count the eigenvalues for.

Each calculation of the above results in a single integer. Such integers alone do not constitute the topological invariant per se, here called $\chi^{(n)}$, but rater are the elements thereof. The previous step can be done for any allowed eigenvalue and rotational operator, but, as shown at length in [23], the total number of distinct combinations that are needed to properly define $\chi^{(n)}$ is

much smaller. Specifically, we may write the required values as [23]

$$\chi^{(4)} = ([X_1^{(2)}], [M_1^{(4)}], [M_2^{(4)}])$$
$$\chi^{(2)} = ([X_1^{(2)}], [Y_1^{(2)}], [M_1^{(2)}])$$
$$\chi^{(6)} = ([M_1^{(2)}], [K_1^{(3)}])$$
$$\chi^{(3)} = ([K_1^{(3)}], [K_2^{(3)}]).$$

The above can describe all n-fold rotationally symmetric 2D systems for the allowed $n = 2, 3, 4, 6$. By repeating the above steps, the invariant $\chi^{(n)}$ may be computed efficiently for any Hamiltonian.

The above walkthrough provides the "how" of computing rotational invariants, but does not directly provide insight into what is physically causing the topological distinction. An intuitive means of understanding what a nonzero $\chi^{(n)}$ is to consider a single isolated band. In such a case, the expression for each element of $\chi^{(n)}$ reduces to a single yes-no question on whether the band has the eigenvalue in question, and comparing that to the same question at Γ. For the element to be nontrivial, there necessarily must be a difference between Γ and the chosen HSP. More concretely, the rotational behavior of the eigenvector *must* change as it passes from Γ to a given HSP.

This, then, gives the "topological" aspect: since a symmetry property changes for continuously defined bands at differing HSPs, the introduction of a finite edge (or other suitable termination) results in states that are trapped on that same edge, analogous to the edge states of other topological effects.

Computational Aspects of Symmetry Indicators for Continuously Defined Models

Computing rotational symmetry indicators in continuously defined systems differs from the discrete TB model in the previous section, since systems like photonic or phononic crystals have eigenfunctions that are represented numerically by $N \times M$ matrices, rather than vectors. The

physics is fundamentally the same, but the numerical details must be suitably adjusted to handle this.

For example, the method employed to determine $\chi^{(3)}$ for a continuously defined model is as follows:

1. Numerically solve the eigenvalue problem for the unit cell at the K and Γ HSPs and extract the phase profile over the full real space unit cell boundaries.

2. Multiply these two phase profiles, point by point, by the numerical value corresponding to the 3-fold operator to be considered(e.g., $1, e^{\pm 2\pi i/3}$). This results in three altered profiles for each HSP (6 in total, though two will just be the original, unaltered profiles corresponding to the eigenvalue 1).

3. Compare each of these altered phase profiles to that of the original phase profile rotated by 120 degrees. This is easily done visually, or can be automated via a point-wise comparison. Whichever altered profile matches is the correct eigenvalue corresponding to that operator acting on that HSP.

4. Apply Eq. (2.25) for all modes up to the desired bandgap/eigenfrequency to retrieve the elements for $\chi^{(3)}$.

This process can be readily adapted to any other rotational operator, and is essentially a point-by-point version of Eq. (2.23), amenable to automated numerical computations.

To see how the above procedure is equivalent to Eq. (2.23) mathematically, we can consider that the physical effect of rotation operators R_n is to rotate the locations in 2D space of lattice sites. If instead of a vector of basis sites we have a continuously defined eigenfunction of 2 dimensions $|\psi(x,y)\rangle$, the operator will act on the physical coordinates (x,y). To then compute the desired expectation value, we generalize the inner product definition to the L^2 norm to find

$$\langle \psi(x,y)|R_\theta|\psi(x,y)\rangle = \int_{cell} \psi(x,y)^\dagger R(\theta)\psi(x,y)dxdy = r_\theta, \tag{2.26}$$

where $R(\theta)$ is the rotation matrix and r_θ are its eigenvalues. This definition is not immediately useful in the case of numerically computed eigenfunctions, where instead we have a discretely defined matrix of complex field values ψ_{nm} up to a given resolution δr. We may instead construct a matrix R_θ that performs the rotation on each eigenfield value to enact the rotation numerically, and compute the inner product discretely as

$$\langle \psi_{nm} | R_\theta | \psi_{nm} \rangle = \sum_{nm} \psi^\dagger_{nm} R_\theta \psi_{nm} = r_\theta \tag{2.27}$$

The above is formally equivalent to Eq. (2.23) in the limit of $\delta r \to 0$, under the same symmetry constraints Eqs. (5.9)-(5.10) for the matrix defining the Hamiltonian. However, this definition is cumbersome to apply, as the matrix R_θ is not a simple rotation matrix. The procedure outlined above is essentially working in reverse of this, where we assume the eigenvalue, apply it to the field, then rotate the field visually to compare it.

2.3.2 Symmetry Indicators for 3D Space Groups

When the system to be analyzed is extended to 3D, the relevance of the space group and all possible 3D transformations becomes great. Recent developments [24, 25] have shown just how powerful knowledge of such symmetries are, and many exotic symmetry-protected topological phases may be classified using just information about the space group and details of the group theoretic behavior of a system. The application of these tools to bosonic settings is the main topic of Chapter 6, and so we will defer explanation of them until needed.

2.4 Real Space Invariants

In chapter 7 the use of topological invariants defined in *real* space are used. Such tools, though existing for many years [26], have not been used extensively, and their practical application

has been largely restricted to condensed matter models. In this section we give the mathematical basis for one such tool, here called the Kitaev sum, and elaborate how it can be applied to continuously defined models in electromagnetics and acoustics. The interested reader may consult the excellent supplementary information of Ref [27] for more details.

2.4.1 The Kitaev Sum

For an eigensystem of arbitrary boundary conditions defined by a Hamiltonian H, we may define the **Kitaev sum** as

$$C^{\mu} = 12\pi i \sum_{\alpha\in A,\beta\in B,\gamma\in C} (P^{\mu}_{\alpha\beta}P^{\mu}_{\beta\gamma}P^{\mu}_{\gamma\alpha} - P^{\mu}_{\alpha\gamma}P^{\mu}_{\gamma\beta}P^{\mu}_{\beta\alpha}). \tag{2.28}$$

In the above $P^{\mu}_{\alpha\beta}$ are projector elements from lattice site α to β, defined for band μ. More formally, $P^{\mu}_{\alpha\beta}$ are the elements of the projector operator given by

$$P = \sum_{E\in\mu} |u_E\rangle\langle u_E|, \tag{2.29}$$

where ω denote the eigenenergies[3], and $|u_E\rangle$ are eigenstates of the Hamiltonian H. We can interpret P as the projection onto spatially localized points summed up to a given eigenvalue $\mu : 0 \leq E \leq E_f$. This summation has a number of properties relevant to future discussion:

1. For the limit of $A,B,C \to \infty$, $C^{\mu} \to C_n$, assuming the rest of the bulk lattice is larger than A,B,C. That is, for large enough regions of lattice points included, the Kitaev sum converges to the first Chern number. Hence, the Kitaev sum is a topological invariant.

2. For a finite lattice, when regions A,B,C include all lattice points, $C^{\mu} = 0$. This implies that any nonreciprocal effects described by the bulk must be canceled by surface states on the external boundary of the lattice.

[3]Generically, these are just eigenvalues, which may be energies, frequencies, etc.

3. Lattice points α need not be defined on any regular grid, nor are regions A, B, C required to be regularly shaped. The only restrictions are that the included regions are roughly equivalent in number of included lattice sites. This means we can use the Kitaev sum for amorphous, aperiodic, or quasi-periodic systems.

The prior introduction is general, but in this dissertation we may loosen the abstraction to make the physics clearer. Namely, we are interested in applying this calculation to examples in simulated electromagnetic structures, so we can introduce concrete forms for the projector elements, the simplest of which is

$$P^{\mu}_{\alpha\beta} = \sum_{E_n \leq E_f} \phi(r_\alpha)\phi(r_\beta)^*. \tag{2.30}$$

Here, α and β are both points in the chosen region (e.g., $\alpha = (x_\alpha, y_\alpha)$ on a Cartesian grid), and ϕ are the (scalar) complex field, either electric or magnetic. Within the usual tight binding methods these projectors are simply lattice sites, but for our purposes these projectors are *continuously defined*, since the electromagnetic modes themselves are spatially extended. Hence, within numerical calculations we must choose a sampling of the real space axis that is sufficiently dense to resolve the behavior.

From Eq. (2.30), we can see that the elements included in the Kitaev sum Eq. (7.1) are simply overlaps of finite points of the EM mode in two locations. We can naturally assume that such terms will average to zero for points far apart, while closely separated (and therefore strongly coupled) points will be larger. From this we can then see that each summation in the Kitaev sum is essentially a "circulation" of the electric field for a given eigenmode. Fully reciprocal structures will naturally have each summation value equal to zero, as the coupling in one direction is equal to the opposite direction. Hence, the Kitaev sum is a local measure of nonreciprocity.

This chapter is partially based on the following papers: D. J. Bisharat, R. J. Davis, Y. Zhou, P. R. Bandaru, and D. F. Sievenpiper, "Photonic Topological Insulators: A Beginner's Introduction

[Electromagnetic Perspectives]," IEEE Antennas and Propagation Magazine, vol. 63, no. 3. The dissertation author was the primary author of this material. R. J. Davis, S. Singh, D. J. Bisharat, and D. F. Sievenpiper, "Topological Defects with Both Real and Reciprocal Space Signatures," In preparation, 2023. The dissertation author was the primary author of this material. R. J. Davis, Y. Zhou, D. J. Bisharat, P. R. Bandaru, and D. F. Sievenpiper, "Topologically protected edge states in triangular lattices", *Phys. Rev. B* 106, 165403 (2022). The dissertation author was the primary author of this material.

Chapter 3

Connecting Classical Systems to Nontrivial Systems

Photonic topological insulators (PTIs) are an exciting option for advanced manipulation of electromagnetic modes, but there is a present lack of understanding on how such modes interact with traditional (classical) electromagnetic modes. PTIs, generally implemented via metamaterials or metasurfaces, permit the flow of electromagnetic (EM) energy only along a boundary of a nontrivial bulk [3]. A chief benefit of such modes is their inherent robustness to disorder, where backscattering is effectively eliminated for fabrication defects and sharp bends of the propagation channel. Despite these benefits, there are currently limited means of efficiently coupling energy into any of these topologically protected devices. Standard experimental methods generally rely on local point source excitations placed near the boundary [28][29], or via direct (non-optimal) coupling to waveguides or other transmission lines [30]. This allows for verification of nontriviality, but is incompatible with any practical application and restricts quantitative comparisons to classical devices. This chapter [31] presents a design and general methodology for an optimized abrupt coupler between a classical microwave transmission line and a topological edge mode, with corresponding analyses on loss mechanisms and robustness, which will permit a

greater understanding of how these exotic topological modes interact with ordinary EM modes. It is an expansion of the authors' preliminary results of [32].

3.1 Duality-Based Abrupt Transitions

Previous efforts have been made to couple energy from traditional transmission lines to spoof surface plasmon polariton (SPP) modes [33][34], as well as to 1-D line waves [35], and a recent study [36] has demonstrated a unidirectional source for a parallel-plate waveguide PTI with high efficiency. However, there are as yet no methods for efficient coupling between surface-wave engineered PTI modes, which represent a promising platform for application, and planar transmission lines. In both [33] and [35] adiabatic transitions are used to convert continuously homogeneous transmission lines into spatially periodic modes, which allows for flexibility in matching the transverse mode profile and/or the propagation constant to achieve high transmission. Such methods are attractive for their flexibility to the initial choice of source, but are limited by the length of the transition and by unwanted effects of radiation from flaring ground planes. In [36], the source is judiciously chosen to permit a unidirectional excitation, and impedance matching methods are employed to minimize reflections. Such techniques can achieve very high efficiency, but are complicated by the difficulty in choosing an appropriate definition for impedance, and by the number of potential geometrical degrees of freedom used to match [37].

A particularly attractive option for practical implementation of PTIs is given in [38], which employs a stack of two patterned metallic metasurfaces between a dielectric spacer, easily implemented via standard PCB fabrication methods. Such a platform for PTIs combines two key ideas: 1. EM duality [39] and 2. the pseudospin degree of freedom for photons. As analyzed in [40]-[42], when a 2D material characterized by a capacitive surface impedance Z_c is placed next to another of complementary inductive surface impedance Z_i, there can exist an EM mode at the interface. By necessity, such a mode is tightly confined to the interface and can therefore

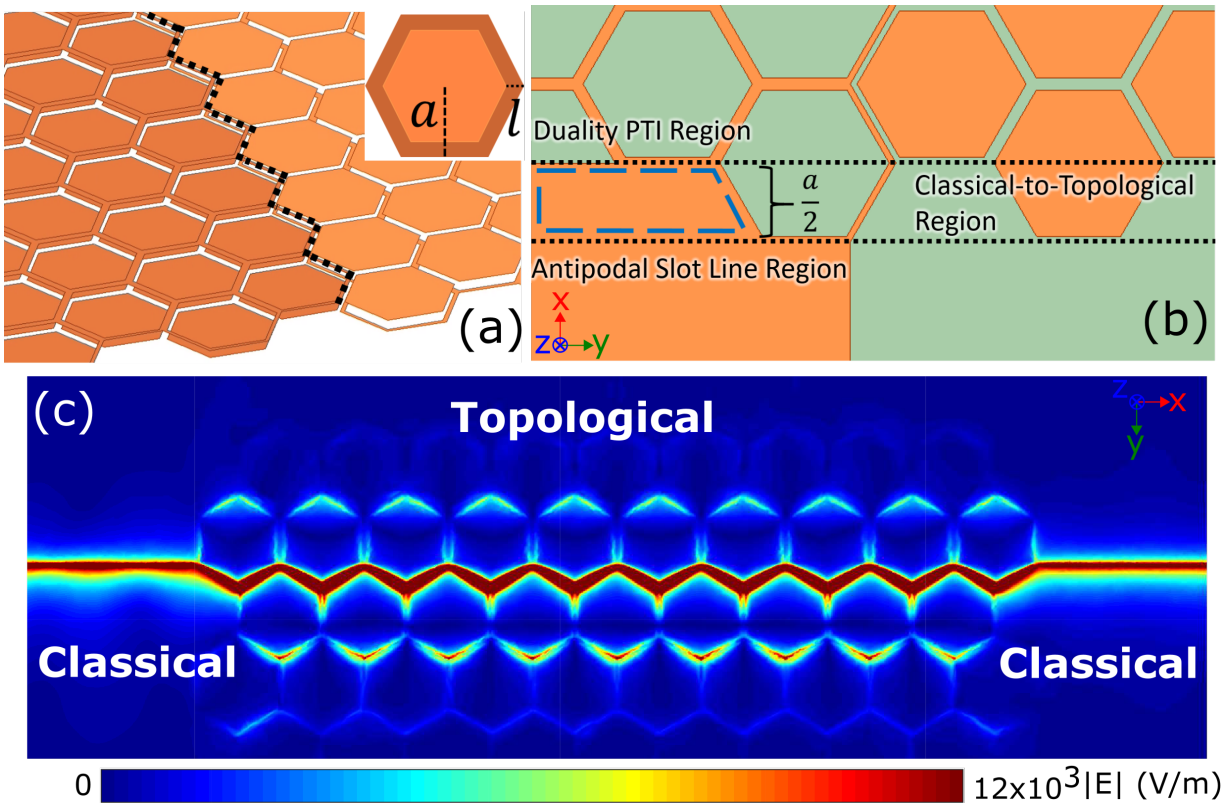

Figure 3.1: (a) EM duality-based spin PTI structure used, with the dielectric removed. The black dashed line shows the path the 1D line wave follows. Inset is the unit cell used, with the lattice period $a = 7$ mm and frame width $l = 1$ mm. (b) Overview of the presented classical-to-topological mode coupling region. Orange denotes metal, while the green is the dielectric support (Rogers RT/duroid R 5880 of thickness $t = 0.787$ mm). The blue dashed region shows the modification to the interface, as discussed in the text. (c) Electric field profile 0.1 mm above the top of the structure (10 unit cells long by 6 wide), with the classical antipodal slot line sections connected at either side.

be considered a 1D mode, or line wave. The condition for complementary surface impedances can be accomplished via EM duality, where $\varepsilon = \mu$, which is possible to implement via Babbinet's principle in metallic surfaces. [40] demonstrates this via a sheet of metal matches (capacitive) interfaced with the dual surface of a connected metal frame (inductive).

Line waves show surprising robustness, but are limited by their lack of a bandgap. The second property, the pseudospin degree of freedom of photons, is where the connection to PTIs comes in. As demonstrated in [38], by bianisotropically coupling modes from two such 1D line waves, it is possible to induce a topologically nontrivial mode at the interface, which emulates the quantum spin Hall effect [2]. To do so, the lattice is chosen to be hexagonal, such that there is guaranteed degeneracy at the K(K') point of the Brillouin zone. To induce the PTI mode, this degeneracy is broken by placing a second sheet of complementary metasurfaces on top of the first, but flipped with respect to the interface (i.e., patches above frames, frames above patches), as shown in Fig. 3.1(a). When the two sheets are close enough to hybridize the TE-dominant patch surfaces and TM-dominant frame surfaces, there is a bianisotropic coupling that opens a bandgap near K(K'), where it can be shown that the hybrid electromagnetic modes $\psi^{\uparrow\downarrow} \equiv E \pm H$ exhibit a non-trivial spin Chern number [43]. Hence, such a structure supports highly robust (though reciprocal) PTI edge modes.

3.2 Mode Behavior and Field Matching

The spatial variation in the unit cell of the PTI gives rise to rapidly varying mode profiles, as depicted in Fig. 3.2. Along the unit cell the electric field changes from highly elongated at the edges to tightly confined vertically between the two inductive layers. This suggests that the location where a traditional transmission line is coupled to the PTI will have a large influence for such structures. A natural choice of traditional transmission line is the antipodal slot line (ASL, the mode profile for which is shown in Fig. 3.2(b)), commonly used for feeding planar

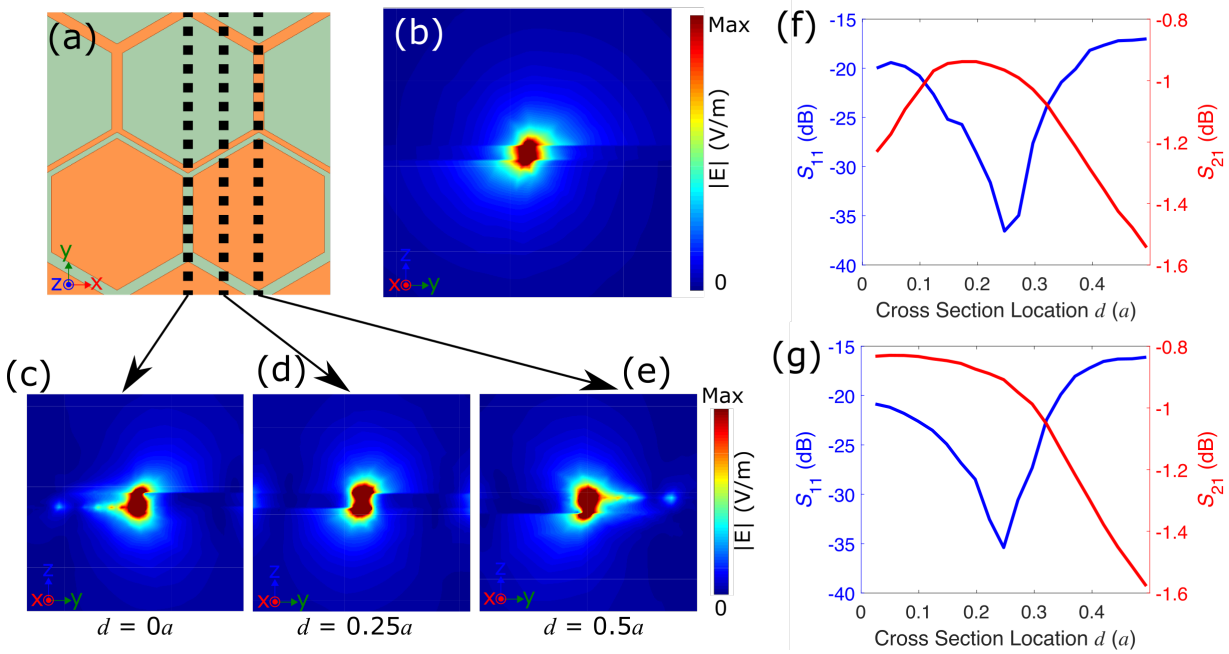

Figure 3.2: Effects of spatial inhomogeneity coupling. (a) Reference plane for (c)-(e), showing the longitudinal locations chosen. Cross sectional electric field profiles of the (b) ASL (uniform along x) and (c)-(e) PTI along half a unit cell, demonstrating high variation. Note that at $d = 0.25a$ the profile is a near match for the ASL shown in (b). (f) Scattering parameters for the ASL directly interfaced with the PTI vs coupling point on the unit cell d. Here, 0 denotes the outer edge of the unit cell. Note that S_{11} is minimized when the field matching condition is closest, at $d = 0.25a$, as predicted by the field profiles. (g) S parameters for the modified interface case, as discussed in the text. Here S_{11} remains unchanged, but S_{21} at $d = 0a$ is improved by reducing edge coupling.

Vivaldi antennas [44]. Such a slot line has the E-field concentrated between the edge of the top and bottom metal layers and closely matches the PTI field profile at 1/4 and 3/4 of a unit cell.

Combining this choice of transmission line with the feed point location as determined by the field profile along the unit cell results in a good match. This is shown in Fig. 3.2(f) by sweeping the connection point between the ASL and the unit cell edge. For all further analysis the results are given for a 10 unit cell long (i.e., along the propagation direction) and 6 cell wide (3 cells on either side of the interface) sample, with the coupler being equal on both sides. Note that 3 unit cells in the "bulk" is reasonable due to the rapid field decay (see later sections). Fig 3.2(f) shows there is a dip in the simulated reflection (S_{11}) at the $d = 0.25a$ connection point, with a corresponding peak in transmission (S_{21}).

Another difficulty is the mismatch that occurs between the hexagonal lattice of the PTI and straight transmission lines. The regions between the abrupt transition create small cavities along the edge, which can be undesirably coupled into by the ASL. This is also the cause of the slight shift in transmission maximum for the case shown in Fig. 3.2(f). To reduce such effects, it is sufficient to metalize a half unit cell past the interface cells, thereby increasing the distance between the first potential edge coupling site and the ASL mode, shown the blue dashed region in Fig. 3.1(b) (the modified interface case). This causes a slight shift in the optimal location from $0.25a$ to $0a$, as indicated in Fig. 3.2(g), where the improvement in S_{21} comes as a result of reducing this unwanted boundary coupling, rather than from the field match. Performing the same procedure on more rows can reduce such effects further, but the exponential decay of the classical mode causes these coupling effects to decrease rapidly with distance, so doing so is unnecessary. Fig. 3.1(c) shows the electric fields 0.1 mm above the top sheet for this case.

The proposed design uses a balanced transmission line to achieve the field match, and as such is readily converted into many other transmission lines. In such cases, an adiabatic transition is frequently used [45]. Alternatives can include stub matches or other impedance transformations. For the purposes of generality the performance here was characterized in terms of the ASL itself,

neglecting contributions from other transmission line conversions. For the experimental data presented, an exponential taper from a microstrip line to the antipodal mode was designed to allow for straightforward connection between the vector network analyzer (VNA, which uses standard SMA connectors) and the device. The taper was partially optimized via a genetic algorithm, but otherwise was not considered further.

3.3 Loss Analysis of the Coupler

To determine the efficiency of the proposed transition, the losses can be broken into several parts and analyzed separately via simulation. Namely, the magnitude of the loss is the sum of the dielectric losses, the radiation losses (both in the PTI and the antipodal sections), and the two transitions,

$$L = L_d + L_{rad,PTI} + L_{rad,anti} + L_{tran}. \tag{3.1}$$

Dielectric losses L_d can be extracted by setting the loss tangent of the material to zero and subtracting the results. To determine the radiation losses of the PTI section the number of cells is swept while keeping the dielectric lossless. Likewise, the radiation loss from the antipodal sections can be found by sweeping their length. After these are found, adding them to the total loss will give the losses incurred by the transitions themselves. Results of this analysis are given in Table 3.1, with details of each component shown in Figs. 3.3(a)-(b).

The current design exhibits a maximum S_{21} of -0.833 dB for the entire structure operating at 16.2 GHz, with a corresponding S_{11} of -21.0 dB. From the loss analysis, the contribution from the classical-to-topological mode conversion L_{tran} is only 0.181 dB (2.1%) per transition.

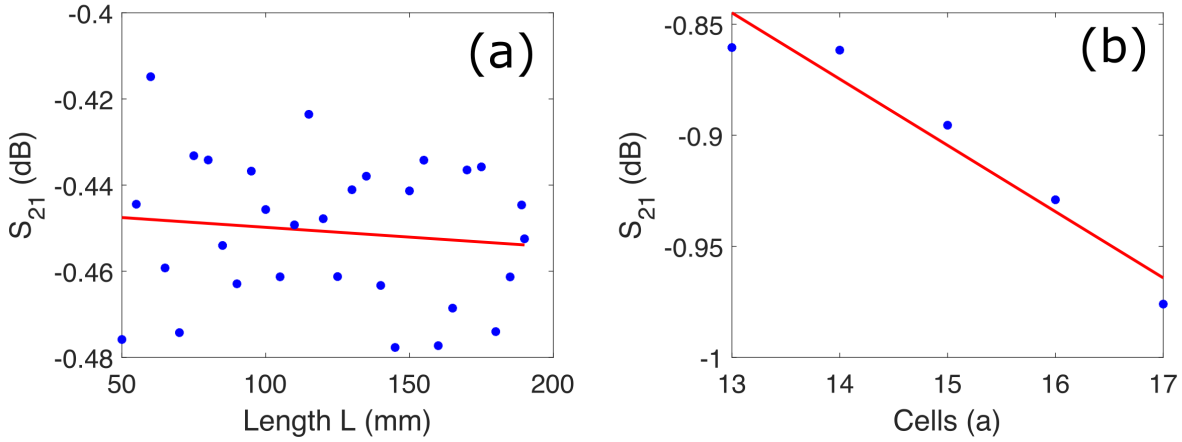

Figure 3.3: (a) Estimated radiation losses of the PTI section $L_{rad,PTI}$, extracted by sweeping the number of unit cells and calculating the slope, assuming a linear relationship. (b) Estimated radiation losses of the ASL, $L_{rad,anti}$, via simulating a length sweep.

Table 3.1: Loss mechanisms and magnitudes

Mechanism	Magnitude
Dielectric (L_d)	0.174 dB
Radiative, PTI ($L_{rad,PTI}$)	0.0298 dB/cell
Radiative, Antipodal ($L_{rad,anti}$)	0.000454 dB/cm
Transitions x2 (L_{tran})	0.181 dB

3.4 Experimental Verification

To verify the design, a sample of the structure was fabricated and measured, using the same parameters as given previously (with the addition of the aforementioned exponential taper to microstrip line, shown in Fig. 3.4(b)). Fig. 3.4(a) shows the comparison between simulated and measured scattering parameters, where the agreement is strong for the majority of the bandgap. Note that the simulation (solid lines) is for the antipodal fed structure (including all forms of loss), while the experimentally measured data shows the full structure with taper, minus the contribution from the taper. When the taper is included, an additional 2 dB of loss is added to the shown values. Near 16.2 GHz, the transmission is above -1 dB, in close agreement with the simulated values.

For visual confirmation, the near field electric fields were measured via a 2D scanner with the probe tip placed $\sim$1 mm above the surface. Fig. 3.4(c) and (d) show the comparison between the simulated and measured real electric fields. Even with the tight vertical confinement it is clear that the desired nontrivial edge mode is strongly excited.

3.5 Analyzing the Robustness of Topological Features

As discussed previously, a chief interest in PTI designs is their immunity to backscattering when presented with a wide class of defects and deformations to their propagation channel. Examples of these are sharp bends, removal of unit cells, and deformations to structure. However, it is often not clear to what extent these robust features present a practical benefit over more common transmission lines and waveguiding technology. With the utility of the efficient transition presented here, it is possible to quantify the performance vs backscatter presented in many implementations.

The most common test for robustness in a PTI is the sharp bend, where the waveguide follows along the 60 or 120 degree bends present in the lattice [30]. In ordinary transmission lines such angles present substantial backscatter, and must be dealt with individually via miter or other bend engineering. Such methods frequently work in microwave devices by reducing the capacitance of the bend, and there are various empirically derived rules of thumb to compute the needed parameters [46]. However, PTIs present an interesting design possibility, as such bends are automatically ”immune” from scattering at any angle that fits within its lattice, as such modes cannot smoothly convert into those moving in the other direction.

Fig. 3.5(a) shows a model of the duality PTI with the presented coupler to a classical ASL, with its field profile shown in Fig. 3.5(c). There is no major scattering visible, but the presented transition enables further analysis of the losses. Using the values in Table I we can calculate the losses incurred by the bends separately. For the model shown we calculate a loss

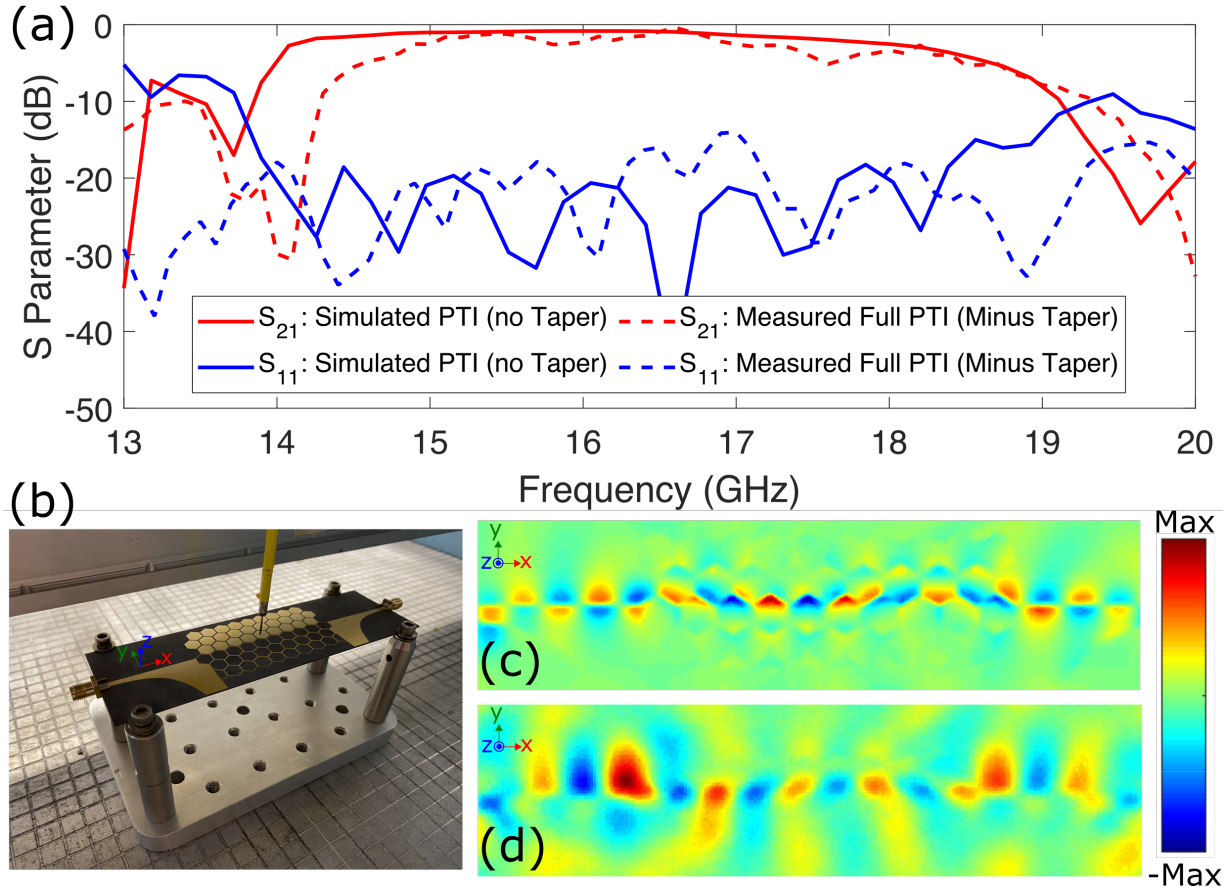

Figure 3.4: (a) Classical-to-topological conversion performance vs frequency. For the experimental result, an exponential taper was used to connect to the SMA connectors of the VNA (shown in (b)), but to isolate the actual mode conversion performance, the simulation was performed without the taper, and the experimentally measured response of the taper subtracted from that of the full structure. Both simulated and measured data include all forms of losses otherwise. The measured transmission is better than -3 dB within 15-18 GHz, and above -10 dB for the whole bandwidth of the bandgap. (b) Experimental setup used for measuring the near fields. Simulated (c) and measured (d) real electric field $\sim$1 mm above the structure.

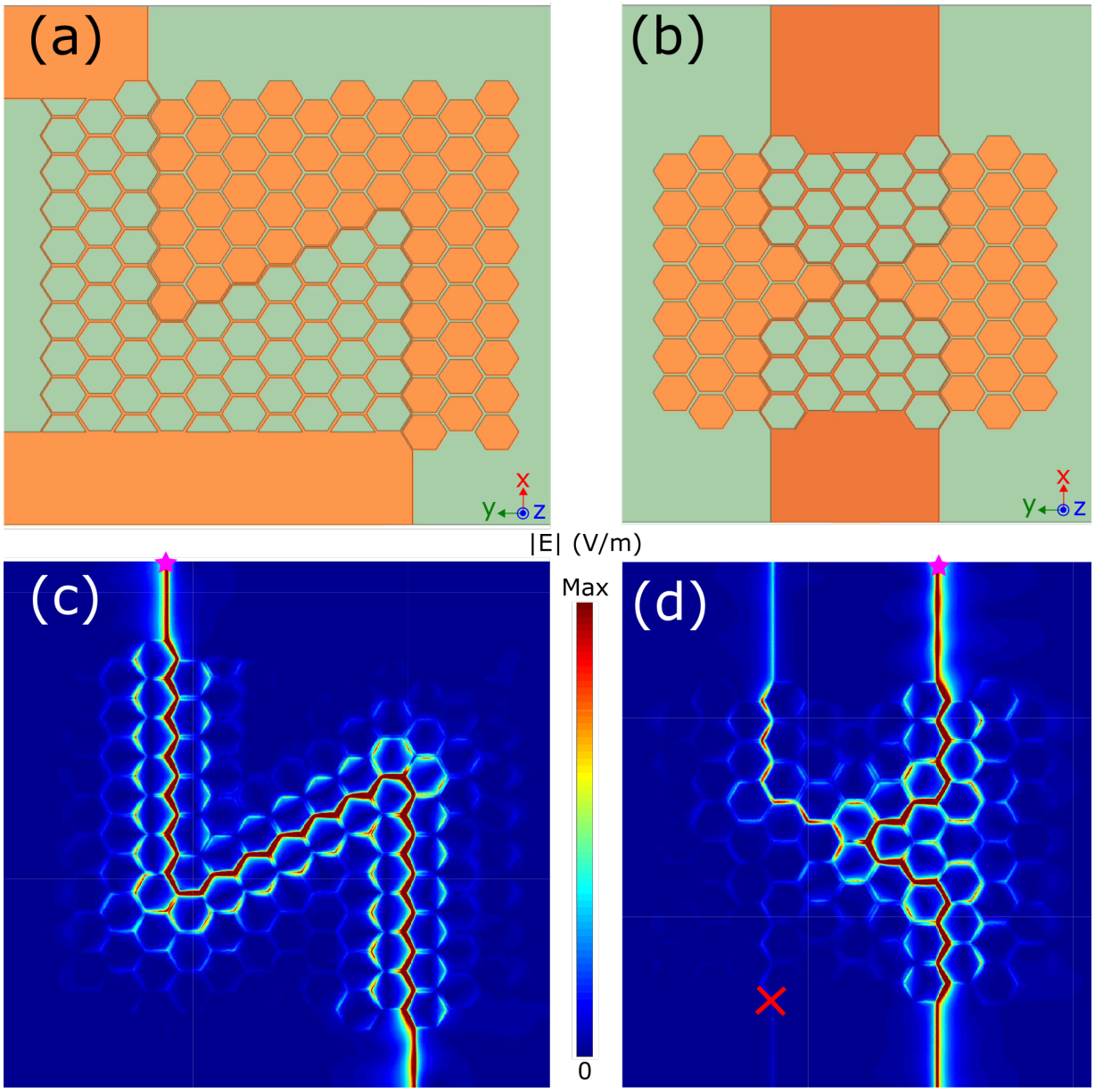

Figure 3.5: (a) Simulated sharp bending path, with two 120 degree turns. (b) Simulated magic T structure, with four input/output ports. (c) Electric field profile for (a), showing negligible losses. The excitation is marked with a pink star. (d) Electric field profile for (b), with port 1 (denoted by the pink star) excited. The downward side has high transmission, while there is practically zero in the "forward" channel. The asymmetry at the gap causes the upward side to have lower transmission, but still well above the "forward" channel.

of 0.036 db per bend (0.073 dB for both). Since the bending losses are close to the simulation accuracy, they can be considered negligible compared to other sources (i.e., dielectric, radiation, and transition). Being an inherent property of topological protection, such a device can be scaled to much higher frequencies (e.g., into the the mmWave band of 5G telecommunications systems) without changing the device design. This is in contrast to classical waveguides, where increasing frequency often degrades the performance of sharp bend compensation methods, thus requiring re-engineering.

The other major demonstration of PTI devices is the so-called "magic T," which is a four-way junction of non-trivial waveguides [47]. In a classical rectangular waveguiding system, such a junction results in equal energy splitting between the two side channels and no transmission through the forward channel. It is significantly harder to form such a junction in planar transmission lines without careful engineering [48]. Due to the spin-momentum locking feature of PTIs, however, such behavior is intrinsic to such structures, even in the case of large mismatches of the propagation direction [49].

Such a setup is shown in Fig. 3.5(b), with the corresponding electric field profile for port 1 activated shown in Fig. 3.5(d). Note that the hexagonal unit cells cause there to be a jump in the left-right symmetry of the waveguiding channel at the interface, which causes a drop in signal across the gap. Nevertheless, there is more than a 20 dB difference in transmission between the forward channel and the oppositely-oriented side channel. The transmission into the forward channel is close to -30 dB, despite being well matched to the direction of propagation compared to the side channel, which is -11 dB. It is possible to manually modify the interface region (e.g., via collapsing the center cell) which allows for greater similarity of the energy split to each side channel, but comes at the expense of increased signal in the forward (forbidden) port. This is due to spin flip processes that allow for energy coupling between the two pseudo-spin modes. See the further sections for further details.

3.6 Field Decay and Finite Effects of Various Bulk Sizes

The model analyzed in the main text employs only 3 unit cells on either side of the interface mode. This may seem surprising, considering the overall approximation being made is of the infinite bulk used to derive the topological behavior of the band structure, but it is well supported by considering the practical effects of the system. Physically, the metallic elements present a very high contrast for the photonic crystal-like structure, which implies a rapid decay into the bulk [5].

To see this, Fig. 3.6 shows the simulated magnitude of the electric field 0.1 mm above the surface of a 10-cell long and variable width sample, excited via a wave port on the bottom of the plot. Fig. 3.6(a) shows the fields with a bulk size of 10 unit cells on either side of the interface (20 total), while Fig. 3.6(b) shows the fields using only 3 cells on either side. They appear visually identical. However, if we then consider fewer bulk cells, the situation changes. Fig. 3.6(c) shows a 2-cell bulk, and Fig. 3.6(d) shows a single cell bulk. The 2-cell case appears to still work, but there is now a visual difference appearing along the outer edges of the sample. As expected, the single cell case hardly works at all, with considerable field concentration at the transition region between the antipodal feed and the interface. The mode that is propagating here is no longer topological, but rather closer to a modified form of antipodal twin line, which has large scattering at each zig-zag bend.

For a more quantitative verification, we can also observe the scattering parameters as a function of bulk width. Fig. 3.7(a) shows S_{11} and S_{21} of the results of Fig. 3.6. As expected, we see that there is essentially no difference in insertion loss for more than 3 unit cells, and negligible difference in return losses. Likewise, we see a rapid decrease below 3 cells.

A general way of characterizing this from a fields perspective (without needing to know the S parameters) is given in Fig. 3.7(b), where we plot the estimated minimum number of cells required to contain 90% of the total fields in the plane of propagation as a function of the

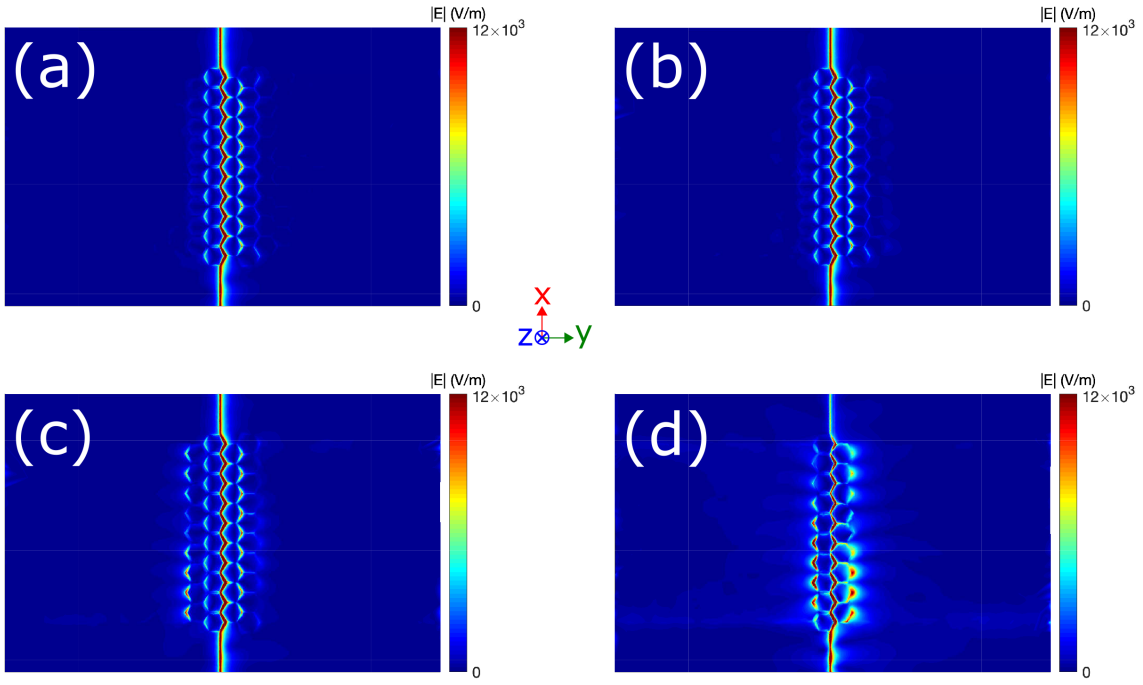

Figure 3.6: Simulated electric field effects of finite bulks. Panels (a), (b), (c), and (d) show the magnitude of the electric field 0.1 mm above the top layer of the PTI for a lateral bulk side of 10, 3, 2, and 1 cells on either side of the interface, respectively. Note that there is no visual difference between the 10 and 3 cell case, supporting the choice of using 3 cells. Further, the 2 and 1 cell cases show larger and larger deviations from the ”infinite” case, leading to field build up and deterioration of the PTI mode, supporting the lower bound of 3 cells.

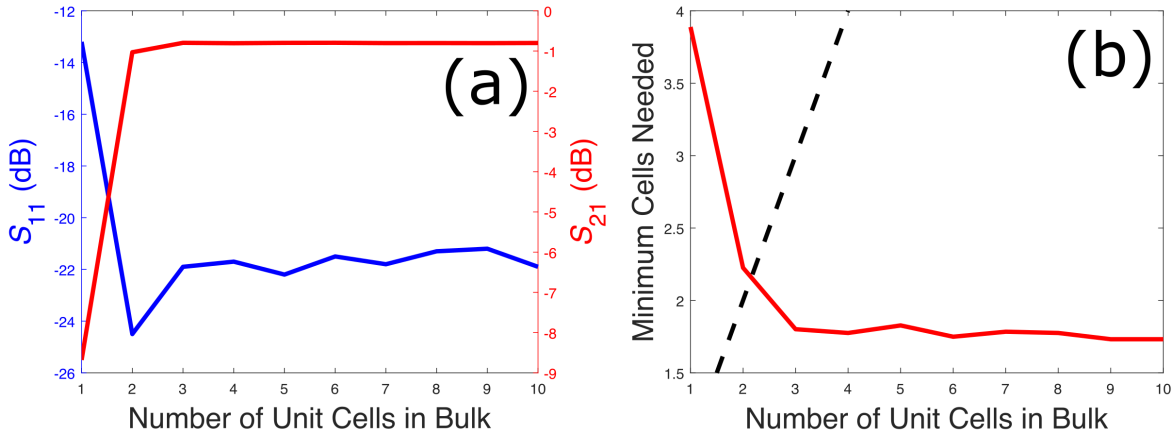

Figure 3.7: Quantitative effects of finite bulk width. Panel (a) shows the simulated scattering parameters of the 10-cell long device as a function of the number of lateral bulk cells. We see that there is essentially no transmission for 1 cell, slightly higher transmission for 3 than 2 cells, and negligible change for larger bulks. (b) shows a general description of the required number of cells needed to contain 90% of the E field as a function of the number of cells simulated. The dashed line represents the point where the required cells matches the simulated cells, which we see is satisfied beginning at 3 cells (points below the line).

total number of unit cells simulated. This is determined by integrating the fields along a line l stretching from the interface outwards laterally as a function of distance x, and taking the first point where the the value is greater than or equal to the threshold τ,

$$Cf(l) \equiv \frac{\int_{l_{min}}^{l} |E(x)|^2 dx}{\int_{l_{min}}^{l_{max}} |E(x)|^2 dx} \geq \tau \tag{3.2}$$

When $Cf(l) > 0.9$, 90% of the total fields are therefore contained within the distance, the result of which is given in Fig. 3.7(b). The dashed line is simply the value when the number of cells required is equal to the number simulated, which we see is first reached when three cells are included. For this case the line of integration is placed in the middle of the sample (5 unit cells in) at the $0.25a$ point of the cell, and at the zero point between the two complementary layers, stretching out from the interface to the right hand side. By symmetry the result is the same if we flip it to the left hand side as well. Note that this last analysis is easily applicable to other interface-mode systems as well.

3.7 Sharp Turns and Magic T Frequency Responses

Fig. 3.8 presents the full simulated frequency response of the ”torturous path” sharp turning model presented in the main text, which includes all forms of loss. It can be seen that the behavior closely matches the straight path case of the main text, with the overall reduction in transmission coming primarily as a result of the extra propagation length, rather than scattering from the sharp turns. This is one of the attractive features of PTI-based designs, for the symmetries of their system cause there to be essentially zero coupling between forward and backward propagating modes.

Likewise, Fig. 3.9 presents the simulated frequency response of the ”Magic T” presented in the main text, broken down into the four different active channel configurations. Part (a), (b), (c), and (d) show the relevant S parameters for an excitation for ports 1, 2, 3, and 4, respectively. In each case we can observe that 1. the reflection is below -10 dB for the full bandwidth of the device, 2. the ”forward” channel, which is the direction that requires a spin-flip process to couple and is therefore expected to be very small, is indeed below -20 dB for most of the bandwidth, 3. side channel 1 is above -2 dB for most of the bandwidth, much the same as a straight configuration, and 4. side channel 2, which is across the symmetry gap, is around -10 dB for most of the bandwidth. As discussed in the text, the lack of symmetry right at the junction between the two channels caused by the triangular lattice results the difference between the two side channels. Nevertheless, the ”forbidden” forward channel is still more than -10 dB lower than the lowest of the two side channels, proving substantial isolation even in the most basic case.

3.8 Discussion and Summary

The coupler presented here compares favorably with similar slow-wave devices. The SPP designs of [33], [34], and [50] report S_{21} values of -0.6 dB, -1.5 dB, and -2.0 dB, respectively, for most of their bandwidth, which are all close to or below the -0.866 dB reported here. Moreover,

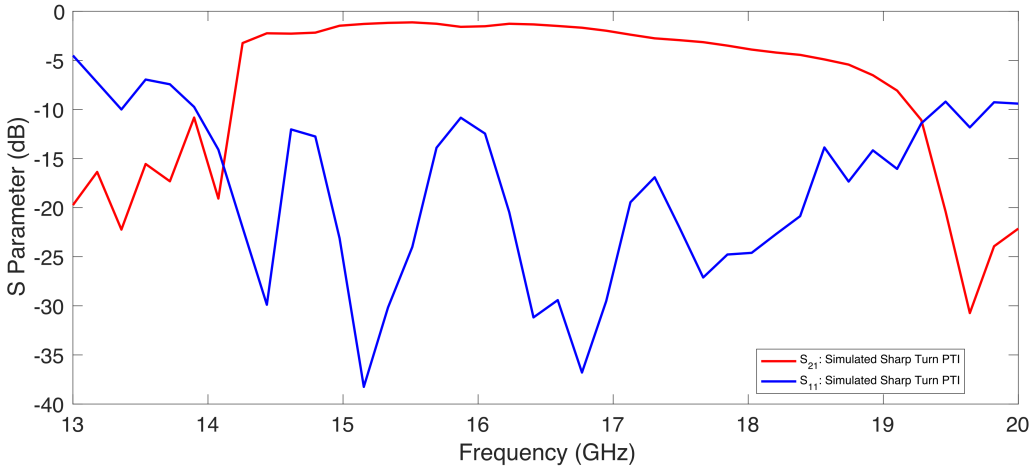

Figure 3.8: Frequency response of the 2-turn "torturous path" sharp turn simulation. All losses are included. Note that the behavior is nearly identical to the straight path, with the decrease in S_{21} caused primarily by the extra propagation losses.

the topological protection afforded to the design allows for negligible losses under sharp bends like those of Fig 3.5(c), which would otherwise cause substantial scattering for SPP designs. Likewise, the propagation losses reported for the PTI structure itself are comparable to those of standard microwave devices (e.g., a 50 Ω microstrip would have ∼0.032 dB/cm vs the ∼0.031 dB/cm for the PTI design with both at 16.2 GHz and equal material settings [51]), all without the need for gradual bends or engineered corners [46].

This chapter presents a compact transition for efficiently coupling energy from a traditional planar transmission line to a topologically protected line wave. An antipodal slot line was used as the initial transmission line, which displays a field profile closely related to the PTI structure. Since the PTI's E-field distribution varies substantially along a unit cell, the exact coupling point is chosen for the greatest match to the antipodal line. Additional alterations to the abrupt transition to account for lattice mismatch and edge coupling effects improve the design further. Use of such a design permits quantitative analyses of many popularly reported structures that rely upon topological phases in waveguiding applications. The resulting transition allows for less than 2.1% /transition of added loss, bringing topologically robust structures closer to integration in practical

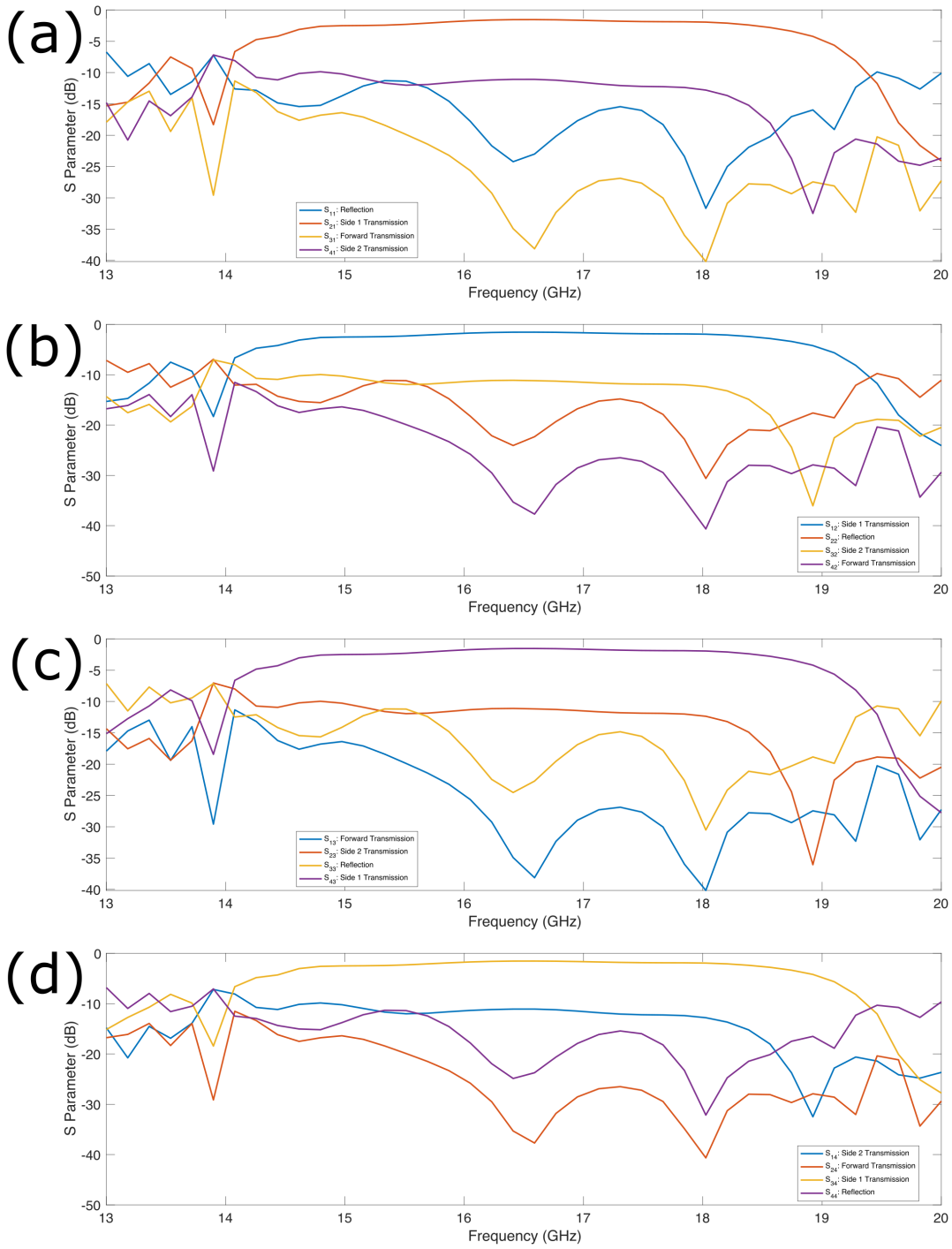

Figure 3.9: Frequency response of the simulated magic T presented in the main text. (a): Port 1 excited, (b): Port 2 excited, (c): Port 3 excited, (d): Port 4 excited. As expected, all four situations result in identical behavior, with the ”forbidden” forward channel being as low as -30 dB, the lowest side channel (across the gap) being close to -10 dB, and the highest side channel being above -2 dB.

applications.

This chapter is based on and is mostly a reprint of the following paper: R. J. Davis, D. J. Bisharat, and D. F. Sievenpiper, "Classical-to-topological transmission line couplers", *Appl. Phys. Lett*., vol. 118, no. 13, p. 131102, (2021). The dissertation author was the primary author of this material.

Chapter 4

Reduction of Symmetry: Hexagons to Rhombi

Symmetry breaking has wide sweeping consequences across physics, and are the foundation underlying the modern theories of topological classification of matter. For the original studies involving the quantum Hall effect, the crucial symmetries are time reversal symmetry ($\mathcal{T}$ symmetry), and for the later discoveries of the quantum spin Hall effect inversion symmetry was included. It was further shown that crystallographic symmetries can also have a profound effect on topological phenomena in condensed matter systems. The ready application of these symmetries onto the experimentally simpler bosonic platforms (photonics and phononics in particular) have led to wide sweeping discoveries with myriad practical applications, including nonreciprocal waveguides for $\mathcal{T}$-breaking systems, spin-filtered routers, and robust cavity modes.

One electromagnetic platform in particular, which employs the additional symmetry of duality of the electric and magnetic fields to generate pseudospin pairs, is especially useful for introducing topological behaviors inside practical waveguiding systems. From the original conception of the idea for waves in pure 2D systems came a version that employs surface waves instead, thereby allowing for a platform readily tested in the lab with traditional PCB fabrication

techniques. They also offer a simple model by which to test how the different symmetries ($\mathcal{T}$, inversion, duality, crystallographic) influence the derived behavior of the edge states.

In this chapter, we show how the reduction of the point group symmetry from C_{6v} (hexagons) down to C_{2h} (rhombi) maintains the same robust edge states, while possessing a number of unexpected properties with regards to its topological features. As such a unit cell can define edges that are straight lines, it also provides a considerably easier to use system for applications in waveguiding.

The chapter is organized as follows: In Section 4.1 we introduce the model, and analyze its topological features in reciprocal space numerically. We show how the reduction in point group symmetry has consequences on the Berry curvature, and prove via group theory how this comes about. Then in Section 4.3, we show how altering the angle of the rhombus (thereby reducing the symmetry further still) changes the band structure as well as the topological behavior. In Section 4.2 we derive an effective Hamiltonian of our model and show how it relates to the Kane-Mele Hamiltonian. Then in Section 4.4 we showcase a range of finite lattices that show how the topological features discussed can be exploited into practical devices. Finally, we provide some conclusions and suggestions for future work.

4.1 Model and Nontrivial Topology

For the original studies of spin-type photonic topological insulators (spin PTIs), the basic models assume a direct mapping to the Kane-Mele Hamiltonian [2] as their basis, and consist of a honeycomb lattice of cells that possess an internal degree of freedom owing to bianisotropy [39]. This mapping retains as much symmetry as allowable, namely the crystallographic symmetry and time reversal symmetry for spin 1/2 particles. The former is achieved by geometry (e.g., selecting a hexagonal unit cell obeying C_{6v} point group symmetry), while the later is enabled by the hybridized electromagnetic polarizations. In this chapter, we retain the electromagnetic duality

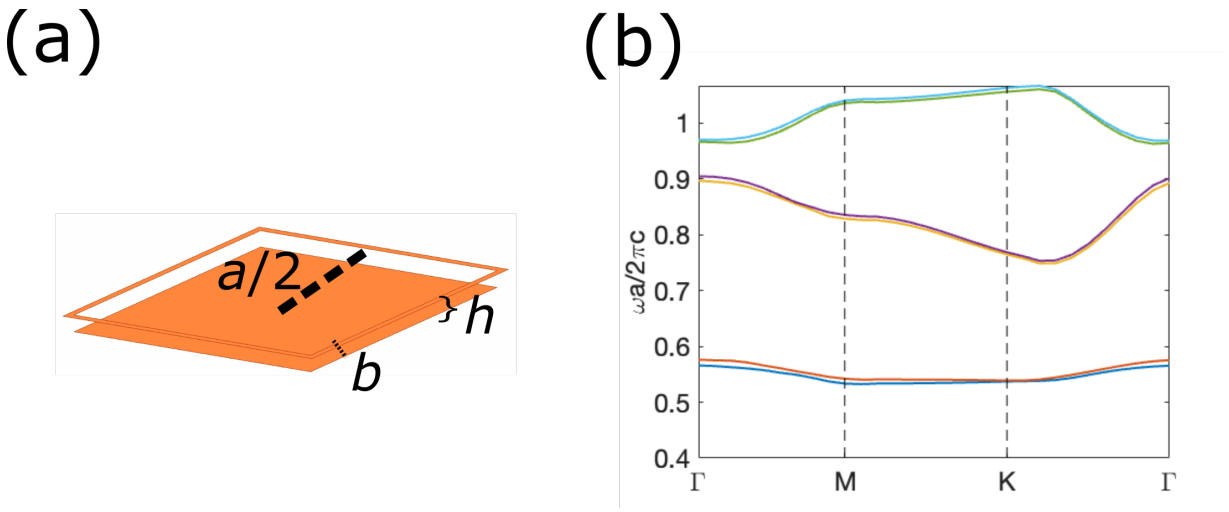

Figure 4.1: Rhombic unit cell and related band structures. (a) The basic unit cell chosen, where the period $a = 20$ mm, thickness $h = 1.57$ mm, and cell boarder width $b = 0.43$ mm. (b) The photonic band structure of the full duality cell seen in (a).

(and therefore the pseudospin degree of freedom), while reducing the point group symmetry.

The unit cell used is shown in Fig. 4.1(a), with corresponding band structure shown in Fig. 4.1(b). We can observe that the EM duality leads to doubly degenerate bands throughout the BZ, as expected. However, we note that, as the point group of the unit cell (here C_{2h} when considering the dual modes) does not omit 2D irreducinble representation, and therefore will not have any enforced Dirac cone at K. This differs from the hexagonal case of Ref. [38].

4.1.1 Chern Number and Berry Curvature

The (spin-projected[1]) Berry curvature for the C_{6v} symmetric model studied in [38] possesses two spikes at the K/K' HSPs, each of which contribute a Berry phase of $\pm\pi/2$, or a spin Chern number of $\pm 1/2$. The location of these points is fixed by the symmetry of point group: in the absence of bianisotropic coupling there is a Dirac cone pinned to the K/K' points by the C_{6v} rotational symmetry of the unit cells [52]. The introduction of bianisotropy induces a bandgap, which causes the Berry curvature to accumulate in the region of the gapped Dirac

[1] As in Ref [38], the definition of the spin-projected modes is given by the hybrid electromagnetic fields $\psi^{\pm} = \sqrt{\varepsilon_0}E_z \pm \sqrt{\mu_0}H_z$

crossing. Integration of the Berry curvature across the whole BZ yields a spin Chern number of ± 1 for the upper and lower bands [6].

However, as a rhombic unit cell lacks the initial rotational symmetry and associated degeneracies, it naturally does not permit the same Berry curvature. To see this concretely, Fig. 4.2 shows the Berry curvature for the first spin-projected band, calculated using the methods of Ref [6]. We note two key features:

1. There is an accumulation of Berry phase near the K/K' points, as in the C_{6v} model.

2. There is equal and opposite accumulation at the *interior* BZ points Σ/Σ'.

The latter feature distinguishes the rhombic cells from the hexagonal cells, and results in a spin-Chern number of 0 for all bands, which would nominally indicate triviality. However, a non-zero accumulation of curvature localized around the K/K' in valley-Hall phase systems leads to nontrivial edge states [21], provided the two valleys are well separated in reciprocal space. Noting that propagation is along the K/K' direction regardless, we may integrate the curvature show in Fig. 4.2 just near those points, which yields a spin-Chern number of +1. Likewise, the second band below the bandgap properly flips sign, yielding a spin-Chern number of -1, satisfying the requirements for time reversal symmetry $C_n = C^+ + C^- = 0$.

4.2 Hamiltonian Description and Symmetry Breaking

The previous sections have examined the behavior of the specific EM dual unit cell numerically, and we have seen the non trivial topology appear. However, to see the generality of these results it is informative to consider a pared down model, namely the original Kane-Mele Hamiltonian. The tight binding description of the model is given by

$$H_{KM} = \sum_{\langle i,j\rangle\alpha} t c^{\dagger}_{i\alpha} c_{j\alpha} + \sum_{\langle\langle ij\rangle\rangle\alpha\beta} i t_2 \nu_{ij} s^z_{\alpha\beta} c^{\dagger}_{i\alpha} c_{j\beta}, \tag{4.1}$$

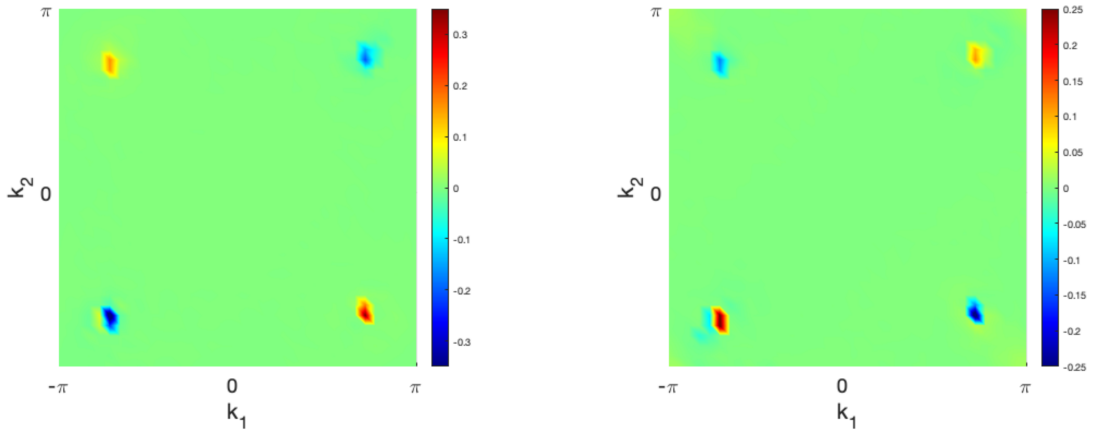

Figure 4.2: Berry curvatures of the rhombic cells. Left panel shows the first spin-projected band, while the right shows the second spin-projected band.

with the first summation covering hopping from nearest neighbor (1NN) atoms, and the second sum covering second nearest neighbor (2NN) hopping between spins. t denotes the hopping amplitude between atomic sites i and j with spin α, t_2 is the 2NN hopping amplitude, ν_{ij} is the spin-dependent term that selects between spin states depending on direction, and $s^z_{\alpha\beta}$ is the spin.

To connect the model of Fig. 4.1(a) to H_{KM}, we will need to appropriately alter the crystallographic properties to match. In Eq. (4.1), the first sum has equal hopping amplitudes among first nearest neighbor lattice sites (e.g., between the two sublattices). Before the 2NN terms are added, we have a simple model of graphene, which has point group C_{6v}, which naturally possesses an enforced degeneracy at the K point due to the existence of the 2D irrep. To force this into C_{2v}, we can simply alter one of the three 1NN bonds, which preserves the two mirror symmetries. This texture is easier to see via the real space arrangement, which is shown in Fig. (4.3). The single altered 1NN bond is shown in the light blue, and the 2NN spin-hopping terms are included as well. Note that without the 2NN terms the model has a continuous bandgap.

This modified model, given again as

$$H_{KM} = \sum_{\langle i,j\rangle\alpha} t_1 c^\dagger_{i\alpha} c_{j\alpha} + \sum_{\langle\langle ij\rangle\rangle\alpha\beta} i t_2 \nu_{ij} s^z_{\alpha\beta} c^\dagger_{i\alpha} c_{j\beta}, \tag{4.2}$$

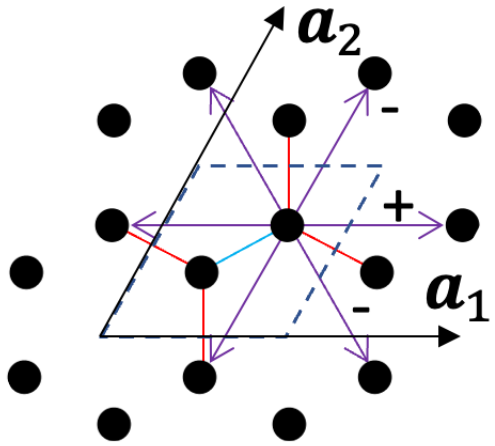

Figure 4.3: Unit cell and hopping arrangement of the modified Kane-Mele Hamiltonian. The unit cell is shown in the dashed blue rhombus, with two atomic sites inside. The black lines denote the first nearest neighbor hopping terms, which are all equal. The red and blue lines denote the imaginary, spin-dependent second nearest neighbor hopping terms. The blue terms are equal, but when the red terms do not equal the blue terms, the model drops to C_{2v} symmetry.

where we have the site-dependent 1NN hopping amplitude t_1, has a representative tight binding band structure shown in Fig. 4.4. Note that here we have not included on-site potential terms, and as such the two spin bands above and below the bandgap are fully degenerate at all $\mathbf{k}$.

To check the topological properties of this reduced symmetry model, we can compute the Wilson loop spectra, which is shown in Fig. 4.5. We see that the two spin bands wind oppositely, and cover the full BZ range, indicating a $\mathbb{Z}_2 = 1$, identical to the standard Kane-Mele result. We can also compute the surface band structure for this model, which is given in Fig. 4.6.

From these, we can see that the reduction in symmetry does not destroy the expected topological insulator behavior. It's worth noting that the mapping from TB model and the electromagnetic model in Fig. 4.1 is not exact; the detailed energetics of the system differ, and the tight binding approximation used does not fully capture the physics that the PTI model possesses. Nevertheless, the fact that we can break the requisite symmetries in the idealized Kane-Mele model without destroying the expected topological surface states is indicative of the effect that switching from a hexagon to a rhombus has on the topology.

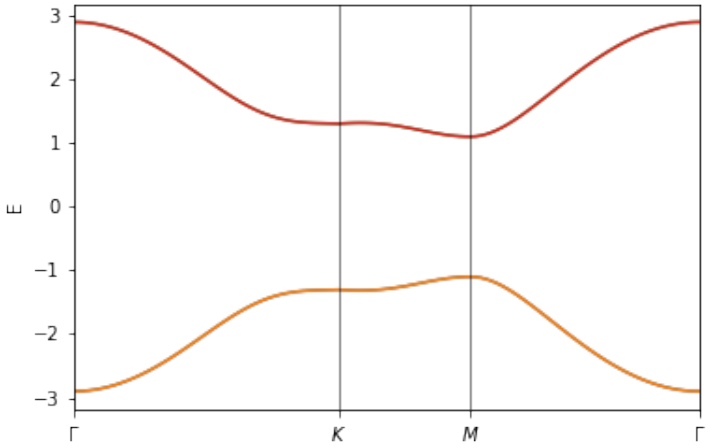

Figure 4.4: Representative band structure for the modified Kane-Mele Hamiltonian, Eq. (4.2). The 2-band TB model used has $t_1 = 1$ for intercellular hopping terms (red in Fig. 4.3), $t_1 = 0.9$ for intracellular hopping, $t_2 = 0.25$, and the spin texture as shown in Fig. 4.3. Note that the spin bands are doubly degenerate at all momenta.

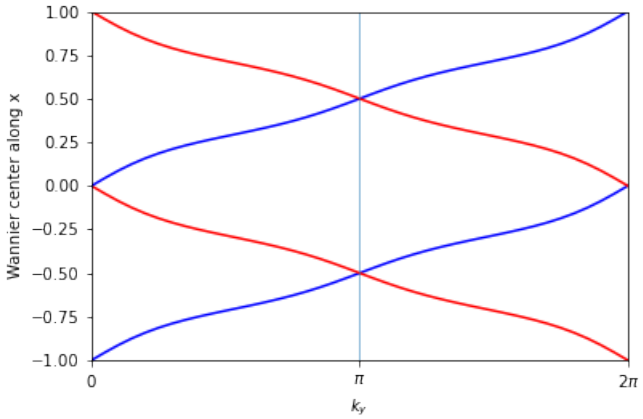

Figure 4.5: The Wilson loop spectra of the modified C_{2v}-based Kane-Mele Model of Eq. (4.2). The blue and red lines are the spin up and spin down modes.

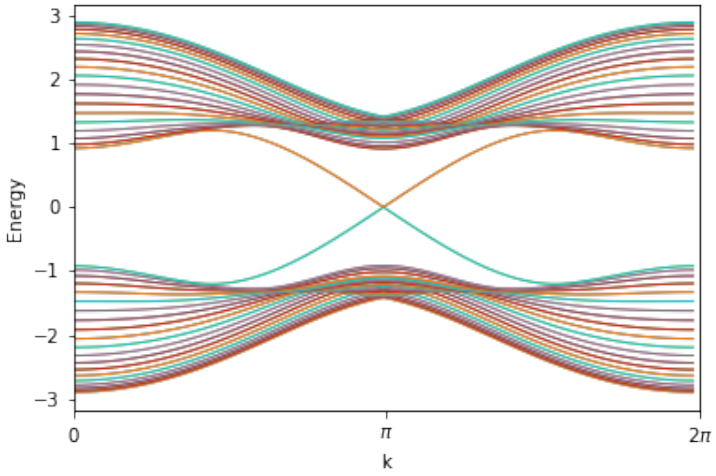

Figure 4.6: Surface band structure for a finite ribbon of unit cells of Eq. 4.2.

4.3 Altering Rhombic Angle

From the prior analysis we can see that the primary symmetry required for the nontrivial surface states to exist is EM duality. To see how far we can push the basic rhombic unit cell, we can alter the angle from the nominal 60 degrees (which lives on the triangular lattice) to any arbitrary angle. This includes the square lattice of $\theta = 90$ degrees. The alteration of symmetry implies differing properties for the Berry curvature accumulation, but we may predict that robust edge states will persist under a wide range of angles, as the bandgap remains open. At 90 degrees, we effectively have a duality spin version of the ”line wave” concept of Ref. [40], though a more detailed analysis is required to understand its robustness.

4.4 Device Implementations

Beyond the topological features observed in reciprocal space, there is a practical benefit to the rhombic unit cell as presented: it is straightforward to construct robust waveguides from them. In Chapter 3 a coupler design was presented, which required carefully adjusting the field

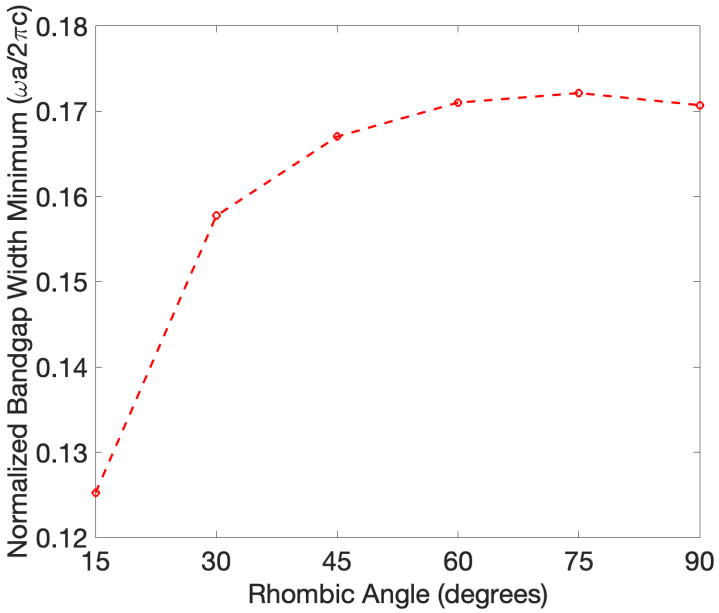

Figure 4.7: Normalized bandgap width as a function of rhombic angle. Here 60 degrees corresponds to the main model under study in this chapter.

match. This was complicated by the hexagonal unit cell, which moves laterally as you move along the propagation path (the ”zig-zag” path). In the rhombic case, the propagation path is a straight line, significantly easing this difficulty. This may also prove useful for topological-based antenna designs [53].

An example of unidirectional excitation of the pseudospin states is shown in Fig. 4.8 [54]. The pink star denotes a hybrid dipole source of electric and magnetic dipoles, the sign of which determines the propagation direction by the usual spin definitions [39]. We see the mode is tightly confined, and negligible field propagates in the opposite direction. Similarly, Fig 4.9 shows a simulation of a model with several sharp bends. The pseudospin mode propagates without scattering, despite the sharp turns.

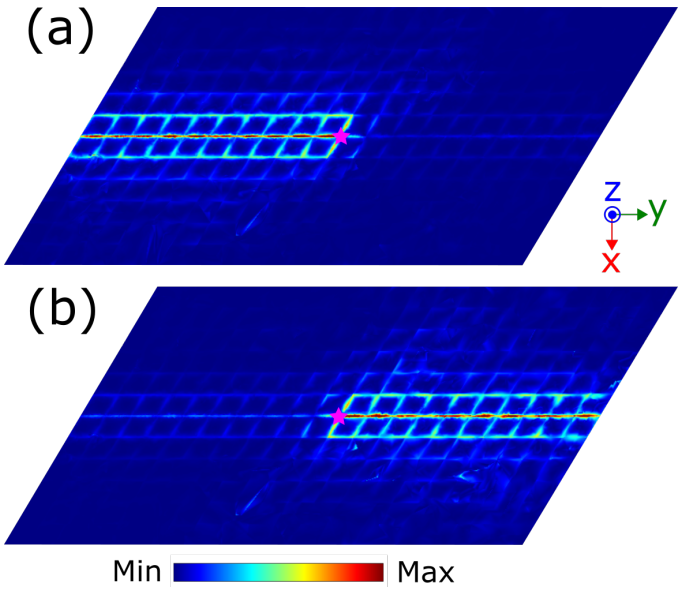

Figure 4.8: Demonstration of unidirectionally excited spin PTI modes, with a Hertzian dipolar excitation of (a) $E_z + Z_0 H_z$ and (b) $E_z - Z_0 H_z$, both placed in the center (pink stars), at 6.25 GHz. The structure is the same as shown in Fig. 4.1(a), with simulated electric fields plotted at the same height.

4.5 Conclusions

In this chapter we have demonstrated and analyzed a platform for studying photonic spin states in a rhombic lattice, which displays surprising topological features. The nontrivial nature of the bulk material was computed via Berry curvature calculations from full-wave simulations, as well as via modifying the Kane-Mele Hamiltonian. The impact of altering the rhombic angle and relevant bandgap closing behavior was also presented. Finally, device implementations were shown, which provide a simple experimental platform useful for applications.

This chapter is based on and is mostly a reprint of the following papers: R. J. Davis, D. J. Bisharat, and D. F. Sievenpiper, "Spin-Type Photonic Topological Insulators on a Rhombic Lattice" In Preparation, 2023. R. J. Davis, and D. F. Sievenpiper, "Robust Microwave Transport via Nontrivial Duality-Based Rhombic Unit Cells," in 2021 IEEE International Symposium on Antennas and Propagation and USNC-URSI Radio Science Meeting (APS/URSI) 619–620 (2021). The dissertation author was the primary author of this material.

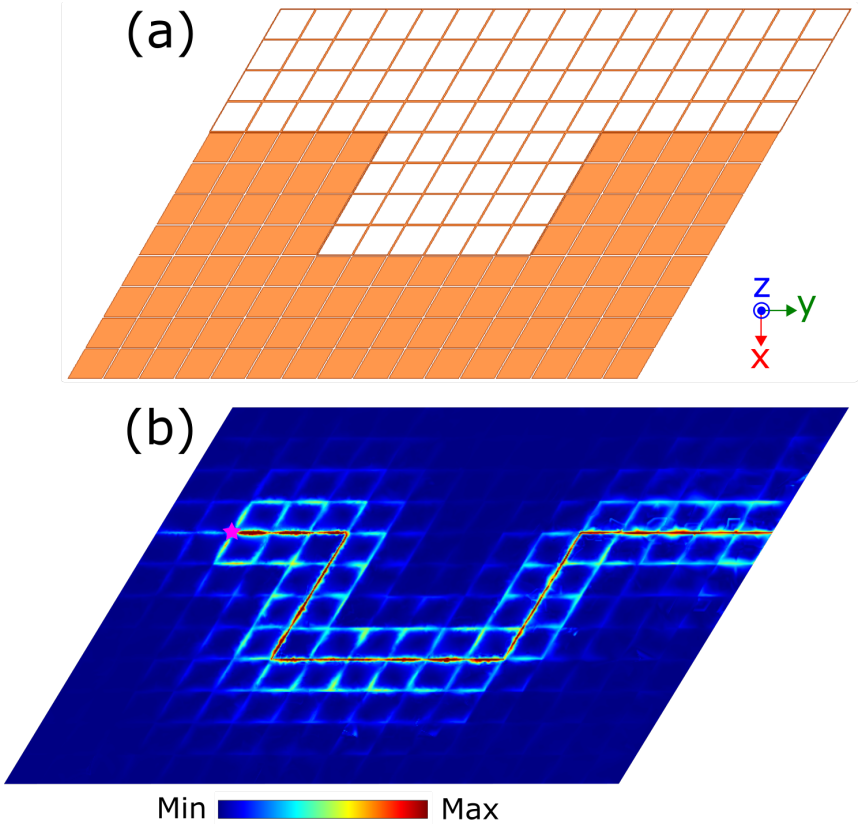

Figure 4.9: Demonstration of the spin modes' robustness to backscatter at sharp turns. (a) top half of the dual structure, with metal shown in orange, (b) simulated electric field in the middle between the two metasurfaces. The excitation is a Hertzian $E_z + Z_0 H_z$ dipole (pink star) at 6.5 GHz

Chapter 5

Topological Crystalline Insulators and Symmetry Indicators

Recent advances in topological physics have revealed a wide class of nontrivial phases that can exist in condensed matter systems, each relying upon maintaining or breaking various symmetries [9]. These studies began with the quantum Hall effect [7] and related time reversal symmetry ($\mathcal{T}$) broken systems, but later were generalized to spin-based platforms that preserve $\mathcal{T}$ symmetry [2]. Still more recently, many experimental demonstrations have explored the use of various crystalline symmetries to create topological insulators (TIs) [55], owing to their simplicity of implementation in bosonic systems. Such crystalline symmetry-protected phases have been demonstrated for systems in square lattices [56] and Kagome crystals [57, 58, 59], and can be well characterized by their various rotation eigenvalues at high symmetry points in the Brillouin zone (BZ). In each case, such phases require a minimum of orbital sites within a unit cell to define the given rotational symmetry (e.g., 4 four the square lattice, 3 for the Kagome, etc.); as such non-primitive cells are required for each.

These crystalline phases stand in contrast to the earlier Chern [7], spin [2], and valley [21] phases, which are defined by topological invariants computed in reciprocal space, as they

instead involve information of the real space defined configuration of the system. The earliest example of Ref. [55] showed how point group symmetries can induce a phase possessing gapless surface states, which are otherwise trivial in the framework of earlier topological classification systems [60, 61]. More recent studies into the influence of crystalline symmetries has yielded a plethora of new phenomena, including higher order topological insulators [62] and surface rotation anomalies [63, 64]. These demonstrations have been recently unified under more general notions of symmetries based on point and space groups, commonly referred to as symmetry indicators [65, 66, 67, 24, 23], which rely on information of the real space configuration as well as knowledge of the wavefunctions at various high symmetry point in the BZ. These techniques reveal a broad class of topologically nontrivial structures in real material systems, which have been efficiently tabulated [68, 69].

Such phases are frequently referred to as topological, insofar as they define a global property of the band structure and can be described by an invariant that changes discretely [65]. This naturally leads to a gauge-dependence for the various topological invariants that characterize them, in sharp relief to those in other systems. This can be seen even in the 1D Su-Schrieffer Heeger model, where the Zak phase depends on the choice of unit cell, though the difference of two such choices is unique [70]. Throughout the paper we will refer to "topologically protected" to include such gauge-dependent systems, as well as obstructed atomic orbital states [23].

Recently, a number of physical systems in photonics [71, 72] and phononics [73] have demonstrated a form of unidirectional propagation for bosons on triangular lattices within a defect line. Such platforms have zero Berry curvature [56, 74], and as such appear trivial from the spin and valley perspectives. We will show via a tight binding model that these systems can in fact be described by a non-trivial topology based on a specific flavor of symmetry indicator that focuses on rotational symmetries [23]. Specifically, in this chapter [75] we demonstrate that a triangular lattice with C_{3v}-symmetric hopping terms can lead to topologically protected edge states.

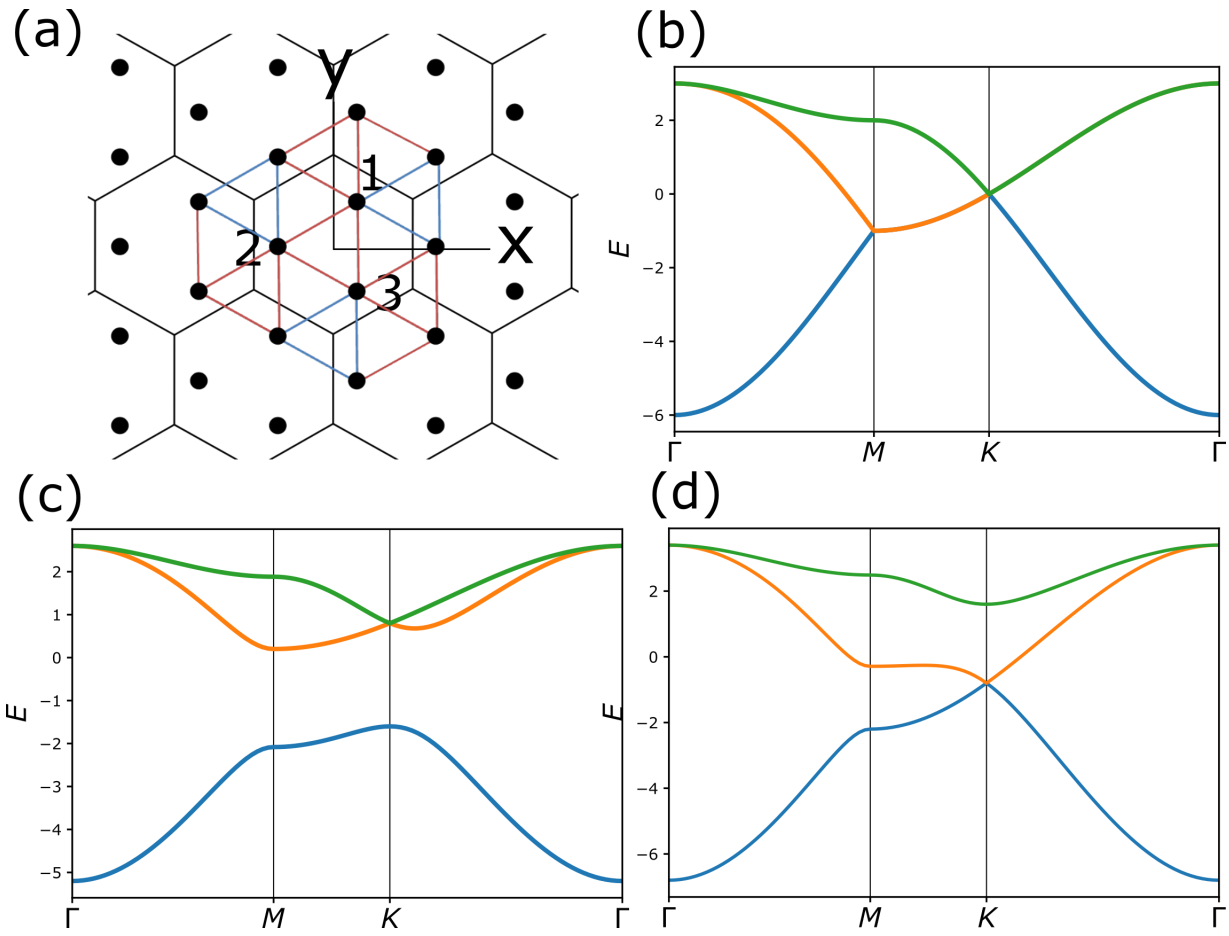

Figure 5.1: Triangular Lattice in a three-band model. (a) Diagram of unit cell in chosen basis, with t_+ bonds shown in blue and t_- bonds in red. (b)-(d) Band structure of the first three bands of the (b) pure triangular lattice with equal hopping $\delta = 0$ ($t_+ = t_-$), (c) nontrivial gapped hopping $\delta < 0$ ($t_+ > t_-$), and (d) Dirac-cone hopping $\delta > 0$ ($t_+ < t_-$).

5.1 Tight Binding Model and Reciprocal Space Characteristics

We adopt a Hamiltonian on a triangular lattice with the hopping texture as shown in Fig. 5.1(a), given generically as

$$H = -\sum_{\langle ij \rangle} t_{\pm} c_i^{\dagger} c_j + \text{H.c} \tag{5.1}$$

Here, $\langle ij \rangle$ denotes nearest neighbor hopping from site i to site j, and $t_{\pm} \equiv 1 \pm \delta$ describes the texture of the hopping terms. We will initially set the onsite potential to zero and limit the analysis to the region of $-1 \leq \delta \leq 1$. We adopt a three-site basis as illustrated in Fig. 5.1(a) with kernel

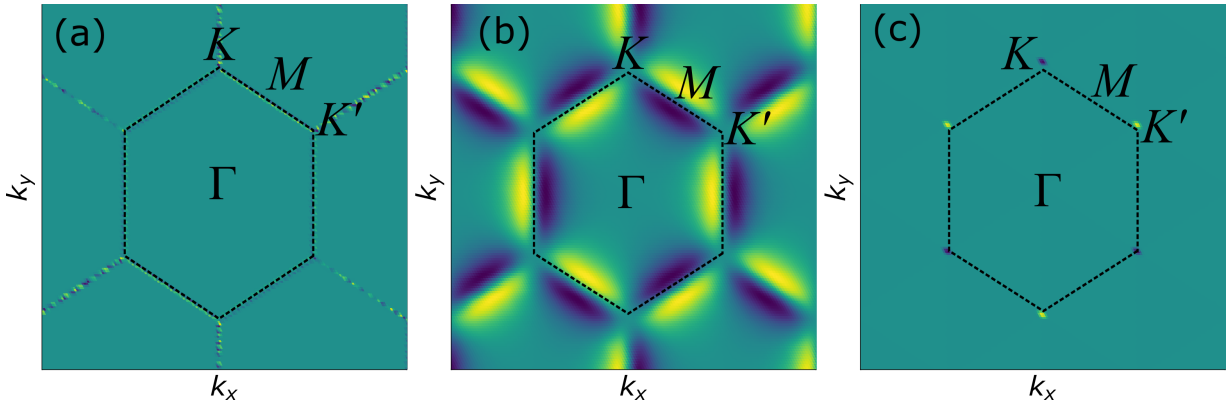

Figure 5.2: Berry curvature distributions for the (a) pure triangular, $\delta = 0$, (b) nontrivial triangular, with a typical gapped value $\delta = 0.4$, and (c) Dirac cone-like, $\delta = -0.4$ cases. In (a) there is rapid fluctuations along the degeneracies at boundary of the reduced BZ (noted by the black dotted line) which average to zero. For (c), a small staggered on-site potential of 10^{-3} was added so the sign of the singularities at K/K' were uniquely defined.

of the Bloch Hamiltonian

$$H(\delta) = \begin{pmatrix} 0 & h_{12}^* & h_{13}^* \\ h_{12} & 0 & h_{23}^* \\ h_{13} & h_{23} & 0 \end{pmatrix}. \tag{5.2}$$

where

$$h_{12} = t_- + t_+ e^{ik_x} + t_- e^{i(k_x/2+\sqrt{3}/2k_y)}$$

$$h_{13} = t_- + t_+ e^{i(k_x/2+\sqrt{3}/2k_y)} + t_- e^{-i(k_x/2-\sqrt{3}/2k_y)}$$

$$h_{23} = t_- + t_+ e^{-i(k_x/2-\sqrt{3}/2k_y)} + t_- e^{-ik_x}$$

The model obeys time reversal symmetry, and falls into class AI of the Altland-Zirnbauer classification [60, 61]. Note that the form of H is similar to Kagome lattices [57], but here each site has 6 nearest neighbors, rather than 4. This has an important consequence in that the low energy band structure is degenerate at all $\mathbf{k}$ values along the $M-K$ boundary for $\delta = 0$, rather than the Dirac degeneracy seen in Kagome models. These extra band degeneracies are not protected by rotational symmetry, as the little group of the wave vector at the M point for

the lattice (C_{2v}) does not permit any 2D irreducible representations [52] (See Section 5.6 for more details). Nevertheless, this difference from Kagome or honeycomb models manifests in the symmetry properties of the Berry phase and how they determine the existence of edge states.

In the ideal triangular lattice with unity potential, $\delta = 0$, we have the degenerate band structure seen in Fig. 5.1(b). If we modify the hopping such that $\delta > 0$, a band gap is opened for the lowest band, as shown in Fig. 5.1(c). For the opposite case of $\delta < 0$, a C_{3v}-protected Dirac cone is found, shown in Fig. 5.1(d). In the following sections we analyze these three cases individually, and show how the latter, gapped case posses an interesting question not readily solved with reciprocal space techniques.

5.1.1 Ideal $\delta = 0$ Case

The ideal triangular lattice under a tight binding (TB) formalism, Fig. 5.1(b) does not have a bandgap, and therefore cannot demonstrate any edge states independent from bulk states. However, as we will further detail in Sec. 5.4.2, such systems do in fact posses a fundamental bandgap within bosonic systems.

Fig. 5.2(a) shows the Berry curvature distribution for Eq. 5.2 under this case. From the combination of $\mathcal{T}$ and inversion symmetry I, the curvature is pinned to zero for all values within the Brillouin zone, except those along the points of degeneracy, where the non-Abelian form of the curvature must be used to determine the values. Here we employ the Abelian form, and as a result we observe rapid numerical fluctuations along the BZ edges that average to zero [56].

5.1.2 Dirac $\delta < 0$ Case

The Dirac case, Fig. 5.1(d) is reminiscent of the valley Hall physics of graphene [21], but here a difference arises in how a gap can be introduced. Namely, if a staggered onsite potential is applied, a gap will appear near K/K', but in doing so the point group is lowered to C_s, rather

than the C_{3v} of a valley-like model. This causes the location of the Berry curvature singularity to shift from K/K', deteriorating any resulting edge states as the "valleys" are no longer at $\mathcal{T}$-linked locations in the BZ. To show this in reciprocal space, Fig. 5.3 shows the evolution of the Berry curvature as the alternating on-site potential is increased. Here the definition for "alternating" is $0, +d, -d$ for sites 1, 2, and 3 of the unit cell as labeled in Fig. 1(a).

It can be observed that as soon as the on-site potential d is non-zero, the Dirac cone is gapped and the singularities form well-defined peaks at the K/K' valleys (Fig. 5.3(a)). However, as d is increased, Fig. 5.3(b)-(d), we see the two peaks drift from the valleys, destroying the valley-like behavior and the valley-projected Hamiltonian will not have a well-defined valley Chern number [76].

5.1.3 Gapped $\delta > 0$ Case

The gapped case, with $\delta > 0$, is different. It is clear that doing so reduces the point group from C_{6v} down to C_{3v}, which permits nonzero Berry curvature via breaking of inversion symmetry (Fig. 5.2(b)). Unlike effective Hamiltonians defined near the K/K' point in valley models, however, the degeneracy being lifted is along the outer boundaries of the BZ rather than the point degeneracy at K/K', and so the resulting Berry phase accumulates along the $M-K$ path with a 3-fold rotational symmetry, provided the correct gauge is chosen [77] (see Section 5.7 for details). As such, standard valley-polarized states cannot appear in this case either. As we will see, however, such a situation does indeed give rise to surface states, but of a different nature.

5.2 Symmetry Indicators of Rotational Invariants

As the Berry curvature of the gapped ($\delta > 0$) phase does not reveal the topological properties, we turn instead to the symmetry properties of each band by the behavior of their eigenstates at the high symmetry points (HSPs) when acted on by various rotation operators

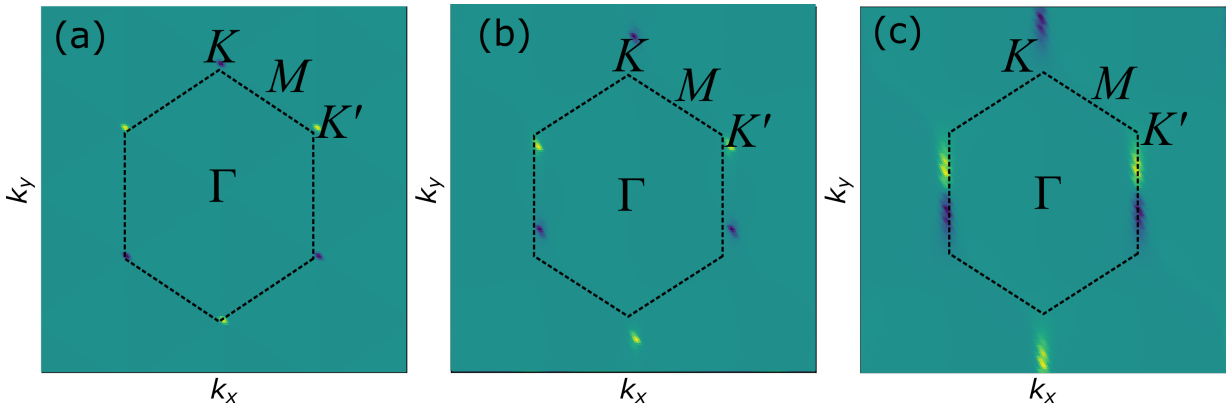

Figure 5.3: Berry curvature distribution for the Dirac-like case of $\delta < 0$ with variable staggered onsite-potential d for (a) $d = 10^{-4}$, (b) $d = 0.5$, (c) $d = 1.5$. In each figure a representative value of $\delta = -0.4$ is used. We see that as the staggered potential is increased, the distribution becomes asymmetric, with K/K' singularities becoming poorly defined.

[23]. Importantly, unlike the gauge-invariant behavior of the Berry curvature, such symmetry behaviors can be influenced by transformations to the real space configuration of the system. More specifically, for a given n-fold rotation operator $\hat{r}_n$, we seek the expectation $\langle \hat{r}_n^u(\Pi) \rangle = \langle u(\Pi)|\hat{r}_n|u(\Pi)\rangle$ for an eigenstate u evaluated at the HSP Π. In the ideal triangular lattice the relevant rotations are $\hat{r}_3$ and $\hat{r}_6$, but within the modified hopping terms (which break C_{6v} symmetry) we will only need $\hat{r}_3$ [65].

In the chosen basis, the three fold rotation operator $\hat{r}_3$ can be represented as

$$\hat{r}_3 = \begin{pmatrix} 0 & 0 & 1 \\ 1 & 0 & 0 \\ 0 & 1 & 0 \end{pmatrix}. \tag{5.3}$$

To evaluate the topology, we must calculate $\langle \hat{r}_n^u(\Pi) \rangle$ for each occupied band at certain HSPs, which we here set to the lowest band only (1/3rd filling), as we are concerned with edge states within the first bandgap. From the theory of [65] and [23], we can then evaluate the topological invariant associated to this rotation operator, given as a vector of two integers

$$\chi^{(3)} = ([K_1^{(3)}], [K_2^{(3)}]), \tag{5.4}$$

where $[K_1^{(3)}]$ and $[K_2^{(3)}]$ are given as

$$[K_p^{(3)}] = \#K_p^{(3)} - \#\Gamma_p^{(3)}, \tag{5.5}$$

and $\#\Pi_p^{(3)}$ is the number of occupied bands with eigenvalue $\Pi_p^{(3)} = e^{2\pi i(p-1)/3}, \quad p = 1,2,3$, for the HSPs $\Pi = K, \Gamma$.

For the sake of generality, we note that to include the degenerate cases of $\delta \leq 0$, we may evaluate $\chi^{(3)}$ by determining the eigenvalues of the overlap matrix $S_{jk}(\Pi) \equiv \langle u_j(\Pi)|\hat{r}_n|u_k(\Pi)\rangle$, where $j,k = 1,2,3$ are the band indices. However, this will naturally give the n-band manifold's invariant, which is not of interest here (see Section 2.3.1 for further details).

In our case we have simplified the expressions from [23] to the case of 3-fold symmetry. In the case of the 6-fold symmetric case of Fig. 5.1(b) (valid only at $\delta = 0$) the rotational invariant is instead $\chi^{(6)} = ([M_1^{(2)}], [K_1^{(3)}])$, which can be found to be trivial by considering an expanded 6-site basis TB model. Likewise, any symmetry properties for other invariants on this basis are also trivial for the 1/3rd filling case. At the critical point of $\delta > 0$, however, we observe a phase transition where $\chi^{(3)} = (-1,1)$, indicating a nontrivial topology. We note here that such a phase is topologically equivalent to the $h_{2b}^{(3)}$ primitive generator Hamiltonian from Ref. [23], which possesses an identical $\chi^{(3)}$.

If we rotate the site assignments of the Bloch Hamiltonian Eq. (5.2) by C_2, or, equivalently, perform a C_2 rotation on the Brillouin zone which swaps the K and K' points, the band structure remains identical to that shown in Fig. (5.1)(d). The difference manifests when considering the symmetry indicator: in this new rotated basis, we find $\chi^{(3)} = (-1,0)$ from the differing phase of the K' point. This new Hamiltonian is topologically equivalent to the $h_{2c}^{(3)}$ primitive generator of Ref. [23]. This implies that a geometrical rotation can result in differing topological phases, which is the mechanism that several recent studies [72, 71, 73, 78] have exploited to realize unidirectional modes in bosonic platforms, which will be discussed in Section 5.4.2.

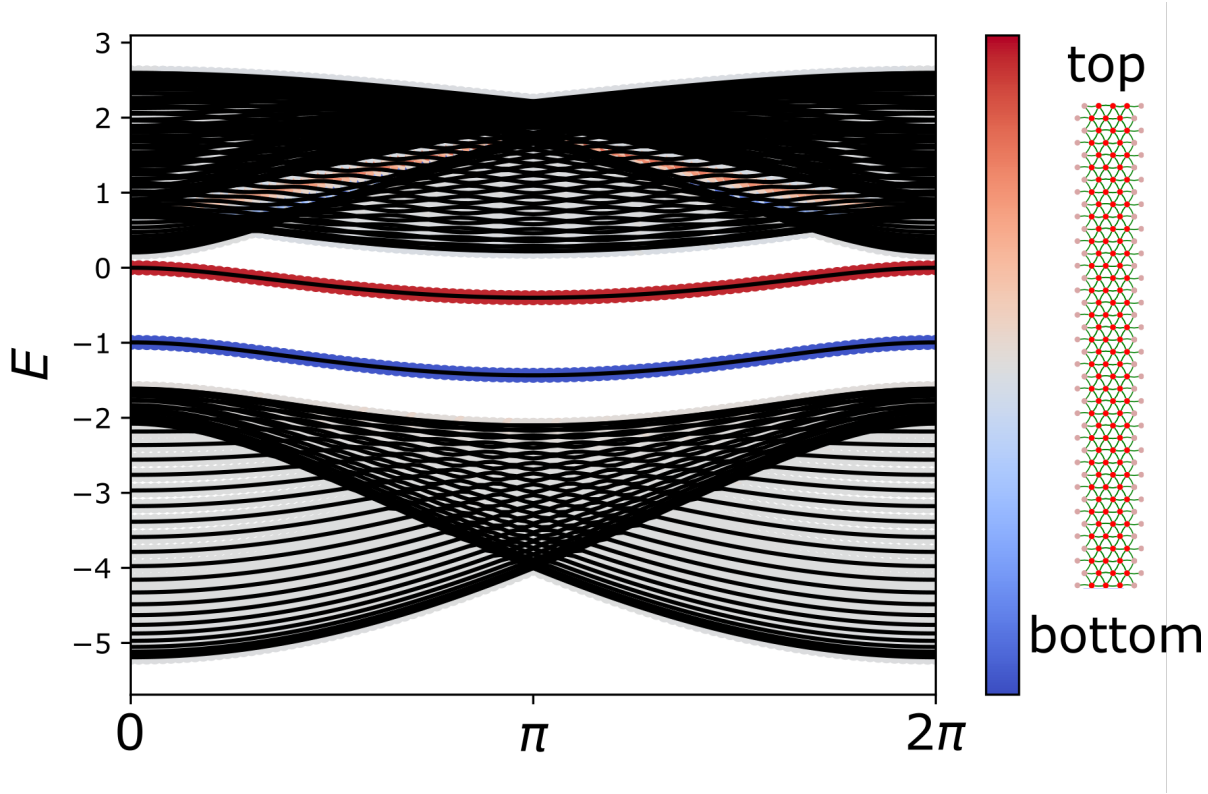

Figure 5.4: Ribbon spectrum of the modified triangular lattice with open boundaries on the top and bottom, showing edge modes within the bulk bandgap, using a normalization of $a = 1$. The color bar shows the expectation value of the position operator in the vertical (y) dimension with with red (blue) denoting modes localized on the top(bottom) of the ribbon. Bulk bands appear black, being fully delocalized.

5.3 Edge States on Finite Lattices

The symmetry indicators show that the Hamiltonian Eq. (5.2) is that of a nontrivial phase protected by C_3 rotation, but it does not guarantee the existence of edge states for all finite edges. Namely, the non-zero value of the $\chi^{(3)}$ indicator here denotes a protected fractional charge per unit cell which can exist along suitably chosen boundaries, rather than the existence of edge states pinned within the bulk band gap (see also Sec. 5.5) Finite boundaries that break the straight-line edge geometry will not support nontrivial edge states. This is important as the existence of the edge states is therefore gauge-dependent, being removable by a change in coordinate system or redefinition of the finite boundary, similar to those seen in Kagome lattices [58]. Fig. 5.4 shows

the spectrum of a finite ribbon of the triangular lattice with $\delta = 0.4$, a boundary that maintains the required symmetry along the top and bottom, and open boundary conditions. We see two edge modes appearing within the bulk bandgap, caused by the non-zero topological invariant $\chi^{(3)}$. The modes are pinned to the top and bottom of the ribbon. The two edge states are here shown at differing energies, which is a natural result of the edge termination being different (i.e., the unit cell is not C_2-symmetric, so the top and bottom edge must necessarily have differences in the hopping texture).

We note here that at $\delta = 0$ there can be no edge states at any energy, but for finite $\delta \neq 0$ they will emerge from the bulk spectrum, including the Dirac-like $\delta < 0$ case. In such cases, as well as the nontrivial $\delta > 0$ case studied here for small δ, the edge states exist within a continuum of bulk states. Only when the finite dispersion of the nontrivial $\delta > 0$ case permits a complete bandgap (here for $\delta = 0.16$) will fully isolated states [1] bound to the edges appear from the continuum (see Section 5.8). Fig. 5.5 gives an energy diagram as a function of δ for a finite lattice, showing these isolated modes appearing for $\delta > 0$.

5.4 Symmetry Indicators for Bosonic Implementations

5.4.1 Numerical Example in Photonics

A key benefit of the symmetry indicator methods used here is that they are readily applied to other physical systems via simulation. This is detailed in [73], where a surface acoustic wave platform results in the same indicators for phonons. As a further demonstration of this, here we show the results for a 2D photonic crystal model, similar to those studied in [72] and [71].

As a computational aside, to transfer the idea of symmetry indicators to such a platform where the wave function is defined continuously over the simulation domain, the definitions for

[1] The states themselves can be removed by a surface perturbation, forced back into the bulk, as they are not required by symmetry to exist at a fixed energy in the bandgap. However, they will emerge under the circumstances presented in the model

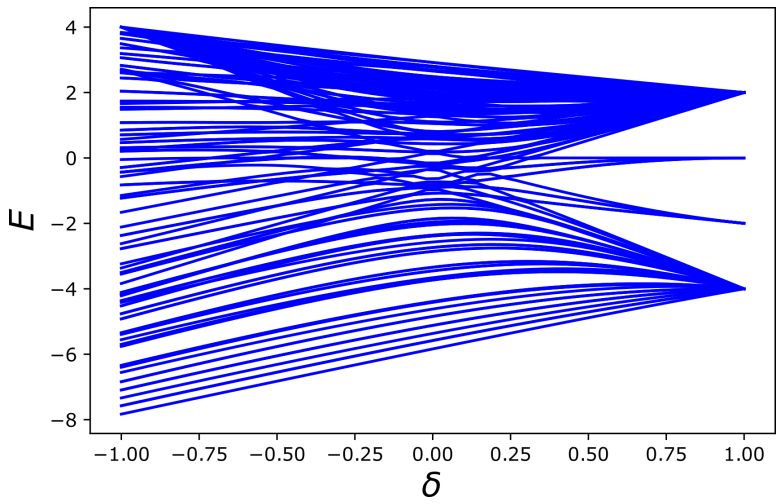

Figure 5.5: Edge mode existence as a parameter of the difference in hopping strengths δ for a finite triangular lattice. Pairs of modes emerge from the bulk band once the bandgap is opened large enough.

the symmetry indicators must be suitably altered. Namely, to compute the various rotational eigenvalues, the procedure can be simply performed via a scalar multiplication of the 2D eigenfield by the relevant complex number corresponding to the rotational eigenvalue. This results in another 2D eigenfield, and the value of the indicator element becomes a sum of each of these fields that match the original eigenfield. For additional details and a walkthrough of this process, see Sec. 2.3.1.

For a 2D photonic crystal in a triangular lattice composed of circular holes (for TE modes) or rods (for TM modes), we may define the unit cell first by placing the circular hole/rod at the center of a hexagon, as show in the inset to Fig. 5.6, which shows a representative photonic band structure calculation; note the high degree of similarity to the nontrivial case analyzed in the main text. The simulation results are done using Ansys HFSS FEM solver using a unit cell size of $a = 20$ mm, air hole radius $r = 4.6$ mm, and a thin ($\ll \lambda$) height of $h = 0.2$ mm, with the background material being silicon ($\varepsilon_r = 11.9$). By symmetry, an equally valid choice of unit cell is one where the hole/rod is shifted, which will keep the bandstructure visually unaltered. Such a choice along with the original symmetrical choice is illustrated in Fig. 5.7.

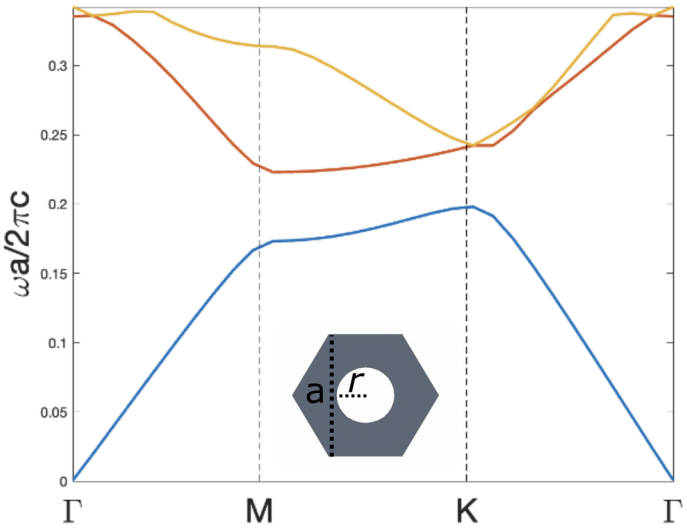

Figure 5.6: Photonic band structure for the first 3 bands of a 2D silicon ($\varepsilon_r = 11.9$) photonic crystal in a triangular lattice. Inset is the structure, where here $a = 20$ mm, $r = 4.6$ mm. The gray indicates silicon, while the white is air.

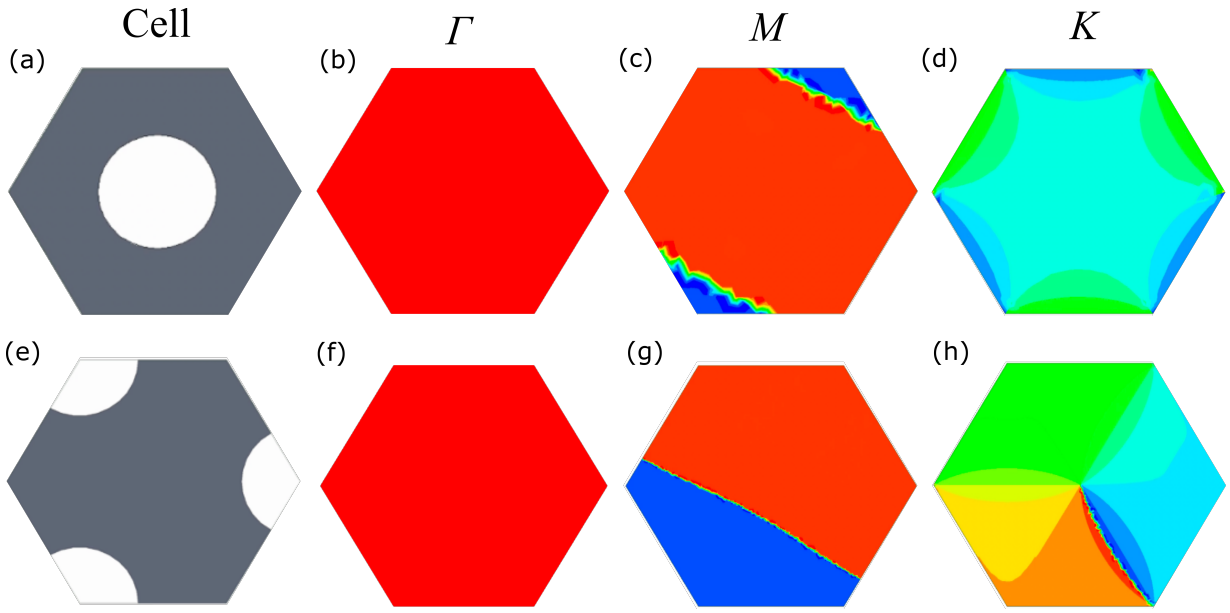

Figure 5.7: Computation of symmetry indicators from 2D photonic crystal phase plots. For the two definitions of unit cell (a), (e), the right three columns plot the 2D phase of the H_z eigenfield at the indicated HSPs.

For the first case, the unit cell has point group C_{6v}, which by symmetry constraints on the Berry curvature is trivial. Likewise, under this orientation the 2D charge polarization (see Section 5.5) is trivial. To compute the symmetry indicator, Fig. 5.7 shows the H_z phase profile at Γ, M, and K, which are C_6, C_2, and C_3-rotationally symmetric, respectively. From these, we compute the symmetry indicators (which can intuitively be seen by visualizing the rotation of the phase plot) and find $\chi^{(6)} = (0,0)$, giving a trivial phase. Hence, from this unit cell definition we do not expect any nontrivial behavior, analogous to a pure triangular lattice on a single site basis, with the difference of the existence of a bandgap.

For the second case, we shift the unit cell center, thereby placing the phase vortex observed from the edges to the center. This shift results in the point group reducing to C_{3v}, and we find the resulting symmetry indicator to be $\chi^{(3)} = (-1,+1)$, matching that found for the nontrivial case of the TB model. Performing a C_2 rotation on the unit cell results in $\chi^{(3)} = (-1,0)$, again matching the TB case.

5.4.2 Connections to Recent Experiments

The TB Hamiltonian Eq. (5.2) describes an idealized spinless particle on a triangular lattice, where topological bandgaps can be induced by tuning of the hopping amplitudes. Despite this idealization, the phenomenon of greatest relevance to experiments is the influence of the crystalline symmetry upon surface states. From the previous section, it can be seen that analogous surface states can be introduced into a photonic system, where the symmetry of the array of holes results in edge states along suitable boundaries.

These numerically predicted edge states have been demonstrated experimentally in both photonic [72] and phononic [73] platforms. In these and other triangular lattice systems, the usual definition of the unit cell is the high-symmetry choice of Fig. 5.7(a), with crystalline C_{6v} symmetry, which would naively map to the $\delta = 0$ gapless case of Eq. (5.2). However, as seen in the previous section, the gauge-freedom in unit cell choice permits a lower-symmetry unit cell

(Fig. 5.7(e)), which reveals a non-trivial topology in analogy to the C_{3v} models analyzed here. An important difference between Eq. (5.2) and such systems, however, is the atomic orbital basis used in TB models does not include the influence of the non-localized nature of classical waves [79], which are instead faithfully represented by a basis of generalized Wannier functions [80].

Despite these differences, such a basis possesses distinct symmetry properties that match those of the atomic orbital basis employed here [81], and the Hamiltonian Eq. (5.2) yields a similar band structure to that of 2D photonic crystal realizations [71]. The only major physical difference is that in the bosonic implementations a flipped copy of the lattice is used to form an interface, rather than open boundaries; as shown here such a rotation results in gauge-dependent phases, and as such also leads to edge states. Such an arrangement also provides a bandgap material on both sides of the finite edge, useful for experiments.

Furthermore, the symmetry indicator method employed here has been extended to the phononics case in a similar system [73], and even to photonics on surface wave metallic systems [78]. Similar ideas have been applied in other photonic platforms, but using different theoretical explanation [82]. These platforms have illustrated the high degree of robustness to perturbations of the system, including sharp angle turns and defects along the boundary.

Care must be made when applying Eq. (5.2) to directly model such bosonic systems for the aforementioned issues of the basis choice. Similarly, within the experimental models in Refs. [72, 73] the states manifest as propagating edge states, though the symmetry indicators used here merely protect the accumulation of edge charges. Propagating states can be expected in such experimental platforms by the inherent setting of a fixed k-vector by the excitation source used, coupled with the non-zero group velocity observed in their band structure. Such states can therefore be removed from the bandgap or have their propagation direction flipped by a continuous surface perturbation, and can be compared to those seen in Fig. 5.4. Nevertheless, the numerical example of the previous section shows a strong connection behind the symmetries involved and the resulting behavior of finite systems. To construct a more direct mapping between

the physics of the bosonic systems and Hamiltonians on triangular lattices as studied here, it would be possible to define a triplet of orbitals on the same lattice site, which can open a bandgap without reducing the symmetry in real space [83].

5.5 Wilson Loop Spectra and 2D Charge Polarization Description

The discussion in prior sections employs the use of symmetry indicators as an efficient and general means of understanding the topology of the system, but this is not the only technique. Alternatively, the Wilson loop spectra can be used to determine the location of the Wannier centers, which gives the fractionalized charge of the lattice. This approach, like the Berry curvature, requires diagonalization of the Hamiltonian for all values within the BZ, and as such is much more computationally demanding for large systems. Unlike the curvature, however, the Wilson loop allows for another topological invariant, the charge polarization [84], to be computed. Here the principle is that displacement of the Wannier center from the center of the (real space) unit cell indicates a charge imbalance that is compensated by edge states on a finite sample. This section will illustrate how the Wilson loop spectra can be alternatively used to explain the behavior of the triangular lattice system studied here.

For the nontrivial $\delta > 0$ case of the triangular lattice, we find the Berry phase as shown in Fig. 5.8. It is important to note that here the coordinate axes are selected such that the lattice sites are displaced symmetrically about the origin (e.g., as in Fig. 5.1(a)). The charge polarization depends on the choice of unit cell, but the location of the Wannier center with respect the physical lattice does not (see Section 5.7 for more details).

We can see that the first band is pinned to $+1/3$ a full BZ winding. As we are concerned with the first bandgap, the important behavior is contained in the fractionalized nature of the first band alone. This indicates a nontrivial topology, which we may formalize via the 2D charge

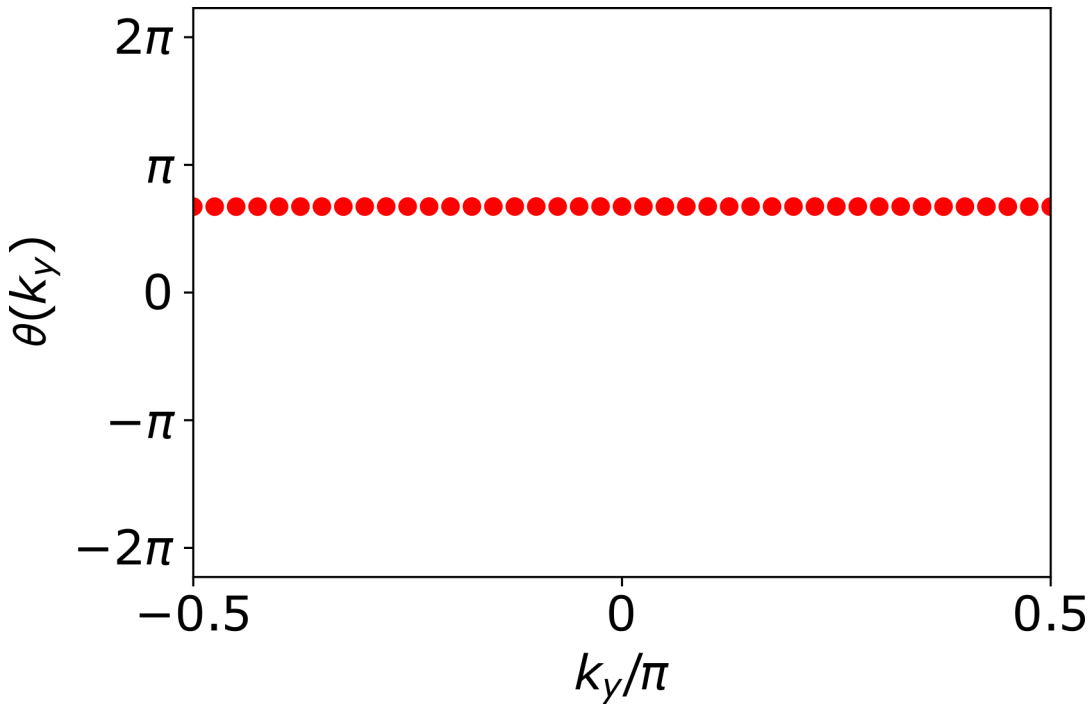

Figure 5.8: The Berry phase computed from the Wilson loop spectra of the $\delta > 0$ TB model. It is pinned to $1/3$rd the full winding for all values across the BZ.

polarization given by

$$P = \frac{1}{2\pi L_{\mathcal{W}}} \int_{L_W} W dl \tag{5.6}$$

Here we have defined the polarization normalized by the electric charge e, and, based on symmetry constraints, reduced the 2D polarization to a single term (as it is equal in both directions for our case). In what follows, we have chosen the lattice vectors $\mathbf{a_1} = \hat{\mathbf{x}}$, $\mathbf{a_2} = \frac{1}{2}\hat{\mathbf{x}} + \frac{\sqrt{3}}{2}\hat{\mathbf{y}}$. From this, we find the nontrivial band to have charge of $+1/3$ for the configuration in Fig. 3.1(a) (e.g., corresponding to $\chi^{(3)} = (-1,+1)$). For the C_2-rotated version (corresponding to $\chi^{(3)} = (-1,0)$), we instead get $-1/3$.

As expected, we recover the same topological protection as that found via the symmetry indicators, albeit with greater computational expense. However, the usefulness of the indicators extends still further, as there is a strong connection between the symmetry indicators found and

the bulk charge polarization itself. Namely, for $\chi^{(3)}$, we may consider the polarization as given by [23]

$$P^{(3)} = \frac{2}{3}([K_1^{(3)}] + 2[K_2^{(3)}]). \tag{5.7}$$

Noting again that we have dropped the vector component here (as both elements will be equal), and that we are still defining the polarization normalized to e, we can now quickly compute the polarization for our model without the full BZ information used in the Wilson loop approach. We find a polarization of $+1/3$ for the $\chi^{(3)} = (-1,+1)$ case, and $-1/3$ (or, equivalently, $+2/3$) for the $\chi^{(3)} = (-1,0)$ case.

Such a connection to the charge polarization makes the existence of the edge states seen in Fig. 3.3 clearer: the states arise due to the fractionalized charge per unit cell, which are pinned to specific locations within the unit cell. When the boundary is chosen such that the charges align, a surface state can appear, but can be removed by a surface deformation.

Lastly, we note that higher order states can be induced within the triangular lattice model presented here using suitable modifications to the hopping structure, in an analogous fashion to those seen in Kagome lattices. This can be predicted by the corner charge (normalized by e) [23],

$$Q^{(3)}_{corner} = \frac{1}{3}[K_2^{(3)}] \mod 1, \tag{5.8}$$

which is equal to $+1/3$ and 0 for the $\chi^{(3)} = (-1,+1)$ and $\chi^{(3)} = (-1,0)$ cases, respectively. As the bulk charge polarization of Eq. (5.2) is non-zero for the gapped phase there can be no fractionalized corner charges, but the Hamiltonian can nonetheless can be combined with other crystalline models that cancel the polarization (the so-called *nominal corner charges*). Under such a combination, we expect to see localized corner states appearing for finite lattices with the arrangement shown in Fig 1(a) of the main text, but not its C_2 rotated copy. This can be understood by considering the edge geometry of a finite lattice with C_3 symmetry, which naturally leads to the Wannier centers appearing on the corners for only one orientation of the unit cell (see

the supplementary info of [23] for further details).

5.6 Group Theoretic Constraints for Ideal Triangular Lattices

Here we give a brief derivation of the constraints on the triangular lattice states based on group theory, much of which can be found in [52].

If we consider a Hamiltonian on a triangular lattice (Eq. (5.2)), the space group is P6mm. To understand the allowable states for the periodic case, we can impose a potential that retains the 6-fold rotational symmetry, as in the case of $\delta = 0$ of the main text. In such cases we can then analyze the behavior of the little group of the wave vector at the various high symmetry points (HSPs) [85].

At the Γ point, the little group coincides with the point group, which is C_{6v}. This group contains 1D and 2D irreducible representations (irreps), and as such implies at Γ we expect isolated as well as doubly degenerate modes. Likewise, at K the little group is C_{3v}, which has both 1D and 2D irreps. Conversely, at the M point the little group becomes C_{2v}, which only contains 1D irreps, and therefore any degeneracy is not required by symmetry.

From the above, we may conclude that the degeneracy along the $M - K$ path shown in the main text is not protected by symmetry, and may be broken by considering differing models of the potential. Indeed, employing perturbation theory to the nearly-free electron model with finite potential will separate the bands at the M point [52]. Nevertheless, a key aspect to the symmetry indicator method used here is that the resulting topological invariant is maintained for these alternative models, as it only requires eigenvectors at HSPs and the preservation of rotational symmetry.

5.7 Gauge Choices for Symmetry Indicator Methods

For the application of the symmetry indicators from e.g., [23], it is worth digressing on the importance of the gauge condition required, particularly for simple TB models like those employed here. Namely, there are two characteristics required to compute the values, the first being the generalized symmetry constraint

$$\hat{r}_n h(\mathbf{k}) \hat{r}_n^\dagger = h(R_n \mathbf{k}) \tag{5.9}$$

where h is the (Bloch) Hamiltonian, $\hat{r}_n$ is the desired n-fold rotational operator, and R_n is the corresponding 2D rotation matrix acting on the crystal momentum $\mathbf{k}$. The second constraint is that placed by the HSPs Π for which the relation

$$R_n \Pi = \Pi \tag{5.10}$$

holds within the periodic BZ. The combination of the above two conditions can be combined to show that, in order for the symmetry indicators to be defined, the rotational operator must commute with the Hamiltonian, $[\hat{r}_n, h] = 0$.

The above conditions are innocuous enough, but there is some subtly with respect to "gauge choices," which can result in unexpected or erroneous conclusions. By "gauge," here we mean both with regards to the gauge choice of the Hamiltonian in the Bloch basis, as well as the "physical" gauge of the real-space Hamiltonian.

The first issue, the Hamiltonian's gauge choice, is seldom discussed, but has genuine consequences, particularly in tight-binding models [86]. When defining a TB model, there are two main methods, the so-called "periodic gauge," wherein the wavefunction is expanded as a sum of Bloch functions, each containing their own phases,

$$\psi_{\mathbf{k}} = \frac{1}{\sqrt{N}} \sum_{\mathbf{R},j} c_j(\mathbf{k}) e^{\mathbf{k}\cdot(\mathbf{R}+\mathbf{a_j})} |\phi_{\mathbf{R},j}\rangle, \tag{5.11}$$

where $\mathbf{a_j}$ denotes the atomic location of orbital site j, and the "Bloch" gauge, where the all atomic sites are considered together with a single phase,

$$\tilde{\psi}_{\mathbf{k}} = \frac{1}{\sqrt{N}} \sum_{\mathbf{R},j} \tilde{c}_j(\mathbf{k}) e^{\mathbf{k}\cdot\mathbf{R}} |\phi_{\mathbf{R},j}\rangle. \tag{5.12}$$

The "Bloch" choice is the one most familiar from textbook examples, as it is both simpler to write down (hopping terms within the unit cell are real numbers) and has the benefit of being periodic in the BZ, $h(\mathbf{k}+G) = h(\mathbf{k})$ for reciprocal lattice vector G. However, the "periodic" choice is often more physical with respect to features like the Berry curvature [77] (in the main text this gauge was used for Figs. 5.2-5.3 for this reason). It is likewise often more natural for calculations involving electrical polarization, as in the Wilson loop spectra. The conventions are related by a unitary transformation, but there are added consequences depending on what further calculations are desired.

For the purposes of symmetry indicators, the Bloch gauge is necessary, as condition (5.10) cannot be met without the periodicity of the wavefunctions. As different numerical software packages for creating TB models differ in their gauge choice, the user may arrive at incorrect answers if the wrong gauge is chosen. This can also lead to great confusion since the initial symmetry constraint (5.9) will hold regardless of gauge choice, as will all physical observables.

The second issue, the "physical gauge" is more easily understood pictographically, but is no less important for the proper investigation of a given model. By "physical," we mean the coordinate system chosen in real space, and the resulting arrangement of the atomic sites. This is often not an issue for most studies, but in cases like the triangular lattice studied here, there can be a great difference between two otherwise identical models.

For example, suppose instead of the unit cell chosen in the main text (Fig. 5.1(a)), the

choice shown in Fig. 5.9 is made. This unit cell has (in the Bloch gauge), the Hamiltonian kernel

$$H(\delta) = \begin{pmatrix} 0 & h_{12}^* & h_{13}^* \\ h_{12} & 0 & h_{23}^* \\ h_{13} & h_{23} & 0 \end{pmatrix}. \tag{5.13}$$

with $h_{12} = t_+ + t_- e^{ik_x} + t_- e^{i(k_x/2+\sqrt{3}/2k_y)}$, $h_{13} = t_+ + t_- e^{-i(k_x/2-\sqrt{3}/2k_y)} + t_- e^{i(k_x/2+\sqrt{3}/2k_y)}$, and $h_{23} = t_+ + t_- e^{-i(k_x/2-\sqrt{3}/2k_y)} + t_- e^{-ik_x}$.

This Hamiltonian, being related to the one used in the main text by a translation of the real space coordinates, has identical eigenspectra as Eq. (5.2). However, a significant difference distinguishes them: Eq. (5.13) has fully trivial symmetry indicators for all δ.

This can be understood by referring the the Wilson loop spectra as analyzed in Sec. 5.5. As the Wilson loop spectra gives the charge polarization, we can see that the center of charge for this model resides at the midpoint between the three lattice sites linked by blue bonds. For the model considered in the main text, this results in the charge polarization being split between three locations on the outer edge of the unit cell, while in the case of Eq. (5.13), it is symmetrically located at the center. From Eq. (5.7), we can conclude that this immediately gives trivial symmetry indicator values. This latter gauge dependency was also exploited recently for waveguiding applications [78].

The above discussion illustrates that, while powerful, symmetry indicators are sensitive to gauge/unit cell decisions, and can cause issues when care is not made in their use. It is also worth stressing here that this gauge-dependence may seem to contradict the notion of "topological protection" in the traditional sense of the quantum Hall effect. Systems as discussed here differ from these others in a number of ways (particularly on the termination structure), but the key feature that permits the "topological" nomenclature here is that they are still a phase defined by a *global* behavior, and can be characterized by a discretely changing parameter linked to the existence of edge states.

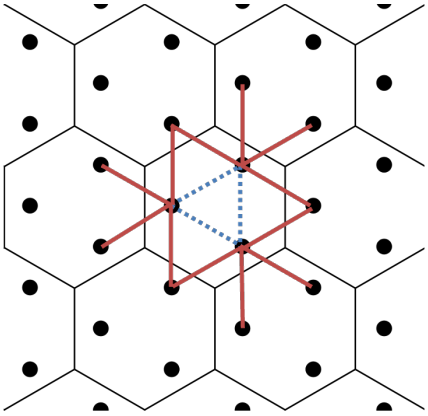

Figure 5.9: Alternative choice of unit cell, with identical eigenspectra but differing symmetry indicators

5.8 Surface States in the Dirac ($\delta < 0$) Case

In the case of the gapless Dirac case, with $\delta < 0$, there is no bandgap, but nevertheless states exist that are localized at the edges of the system. Without a bandgap they naturally coexist with bulk states, which is shown via a ribbon spectra for a semi-infinite model shown in Fig. 5.10. As discussed in Sec. 5.3, as δ is tuned to the transition point of $\delta = 0$, a bulk bandgap is opened, which permits these localized states to be isolated from the continuum under the parameter regime given in Fig. 3.4. Such states cannot be naively classified as topological (as there is no bandgap), but are still related to the symmetry-enforced existence of Dirac cones (see Fig. 5.1(d)).

5.9 Conclusions

We have demonstrated that a triangular lattice chosen with a 3-site basis and a specific hopping texture is topologically nontrivial, and can support states bound to finite edges that maintain a straight line termination. The model does not possess nonzero valley or inversion-symmetry topological invariants, and is instead described by a symmetry indicator arising from rotational eigenvalues. Our model deepens our understanding of a number of recent experimental demonstrations related to anisotropic wave/energy propagation and verifies their real space

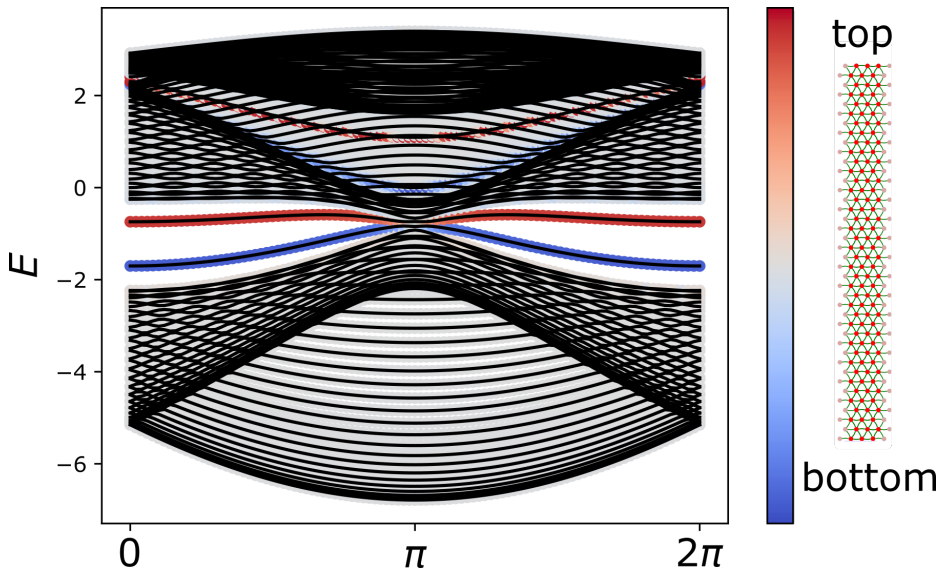

Figure 5.10: Ribbon spectrum of the modified triangular lattice with open boundaries on the top and bottom for the Dirac ($\delta < 0$) case, showing edge states, using a normalization of $a = 1$. The color bar shows the expectation value of the position operator in the vertical (y) dimension with with red (blue) denoting modes localized on the top(bottom) of the ribbon. Bulk bands appear black, being fully delocalized.

topological origin.

This chapter is based on and is mostly a reprint of the following paper: R. J. Davis, Y. Zhou, D. J. Bisharat, P. R. Bandaru, and D. F. Sievenpiper, "Topologically protected edge states in triangular lattices", *Phys. Rev. B* 106, 165403 (2022). The dissertation author was the primary author of this material.

Chapter 6

Symmetry Indicator Analysis for 3D Systems

The tools of symmetry shown in the previous chapters are only a small subset of possible tools to evaluate the topology of different systems. In particular, they have focused on 2D systems, where the relevant symmetry groups are those of point groups and the 17 wallpaper groups. In 3D systems, a large number of new symmetries appear, and with them a huge number of possible crystallographic-protected phases. In this chapter we show an example of the application of one recent tool, the so-called symmetry indicator method for space groups [24]. Specifically, we will show an analysis of the topological properties of a phononic lattice, where the introduction of a screw dislocation induces a pair of unidirectional helical modes propagating within the bulk bandgap.

6.1 Symmetry Indicators and Band Representations for Space Groups

Symmetry indicators [24] are a recent development that draws on earlier works on the combinatorics of band structures [87, 66, 67]. Parallel developments using alternative mathematical methods have also proven useful for classifying symmetry-protected systems [25]. The critical insight to all such methods is the relationship between the symmetry properties of a given system's eigenfunctions and the set of possible *atomic insulators* corresponding to a given space group and collection of internal symmetries (spin, time reversal, etc.). In brief, the theory permits a rapid diagnosis of the potential topological surface states on symmetry protected boundaries, using just the knowledge of irreducible representations (irreps) of the bands up to a given bandgap at the various high symmetry points, expanded onto a basis of symmetry allowed atomic insulators. The later have been exhaustively computed for all 230 space groups, with and without time reversal symmetry and spin-orbit coupling [68, 69], which are simply unimodular matrices. The calculation of the irreps is also a standard process, though in the case of vector-valued fields in 3D (as the phononic example shown here is) require slight modification, as detailed in Sec 6.2.

We will now give a brief overview of the relevant mathematical tools. For greater details, Ref [88, 89] provide a wealth of examples.

6.1.1 Symmetry Eigenvalues and Irreducible Representations

For a given periodic system under question, modeled as an eigenvalue system with Bloch Hamiltonian H, $Hu_n(\mathbf{k}) = E_n u_n(\mathbf{k})$, we have a set of bands $n \in \mu$, up to a bandgap[1]. With a closed Brillouin zone (BZ), we may associate each separate eigenmode $u_n(\mathbf{k})$ with a set of high symmetries points, dictated by the space group [90, 91].

[1]The theory summarized here works for gapless systems as well [24], but we will not concern ourselves with such cases here.

For each of these eigenmodes at HSPs, we may compute the set of symmetry eigenvalues for each by the same method employed in Chapter 5, via

$$\chi_g = \langle u_n(\Pi|g|u_n(\Pi)\rangle, \tag{6.1}$$

where the inner product computes the eigenvalue of mode u_n at a given HSP Π under the action of a given symmetry element g of the little co-group of the space group. Concretely, we may think of this as the behavior of the mode when we apply a symmetry (rotation, mirror, etc) that is allowable by the symmetries the wave vector may have at that HSP, which in turn set by the symmetries of the space group, all of which may be readily found from tables [90].

Once the χ_gs have been calculated for all g, the irrep may be found by the "magic formula" of character orthogonality [91], given as

$$m_p = \frac{1}{||G||} \sum_{g \in G} \chi_p^*(g)\chi_g, \tag{6.2}$$

where m_p is the multiplicity of an irrep p of the little co-group $G_{\mathbf{k}}$, $||G||$ denotes the cardinality of the little co-group, and χ_p is the characters for irrep p. The latter can be found via tables [90]. m_p will be zero for all but one choice of p, and the remaining nonzero m_p will give the dimension of the correct irrep that the mode u_n corresponds to (e.g., $m_1 = 1$ implies the mode is a 1D irrep, $m_p = 2$ implies a 2D irrep, etc). This allows a quick means of checking the irrep of a particular eigenmode.

6.1.2 Compatibility Relations

Once the given irreps have been computed for all modes u_n at all HSPs up to a given bandgap, we may consolidate this information, along with the number of bands ν, into a "vector"[2],

$$\mathbf{n} = (\nu, n^1_{\mathbf{k}_1}, n^2_{\mathbf{k}_1}, \cdots, n^1_{\mathbf{k}_2}, n^2_{\mathbf{k}_2}, \cdots). \tag{6.3}$$

Each value $n^j_{\mathbf{k}_i}$ is the sum of all modes at HSP $\mathbf{k}_i$ transforming as irrep j. This vector contains all the symmetry content of the band structure, taken as a whole. As was shown in Ref [67], such a vector is closely related to the so-called compatibility relations of the given space group. Such relations can be likewise found tabulated [90].

6.1.3 Atomic Insulator Basis

For a given space group, a set of vectors $\mathbf{n}$ can be likewise computed, which are a general consequence of the imposed symmetries of the space group itself. These vectors have been exhaustively computed [68], and interested readers may consult Ref. [24, 88, 68, 69] for full details on their methods. For our purposes, we will simply read off the vectors, consolidated into the matrix A for a given symmetry setting (space group and related internal symmetries).

With the matrix A of atomic insulators, we may then simply expand the specific system's band structure behavior $\mathbf{n}$ onto this set,

$$A\mathbf{q} = \mathbf{n}, \tag{6.4}$$

where we have expansion coefficients $\mathbf{q}$. The above may be computed via the pseudo-inverse of A, such that $\mathbf{q} = A^{-1}\mathbf{n}$. Based on $\mathbf{q}$, there are two main possibilities:

1. All elements of $\mathbf{q}$ are integers: The system is trivial, as far as the symmetry indicator method

[2]This object is not a true vector, as it is not a member of a vector space, but its has properties very similar to one [88]

is concerned. That is, the band structure can be represented by a set of atomic insulators. This does not preclude all topological phases, but merely that other, more specialized tools must be used.

2. Some of the elements of $\mathbf{q}$ are fractions: The system is either topologically nontrivial, or possesses at least one degeneracy (e.g., is in a semi-metal phase). We can distinguish these two cases by the largest common factor of the columns of matrix A, C_i, which, when multiplied by the corresponding value of $\mathbf{q}$, q_i, will be either integral (implying the nontrivial first case), or fractional (giving the semi-metal second case) [69].

As shown in Ref [24], the atomic insulators bases A possess an algebraic structure of a finitely generated Abelian group, and as such can be

6.2 Aspects of Indicator Theory for Bosonic Systems

The above discussion applies to a general eigenvalue system, but there are certain subtleties when using it to analyze bosonic systems like the phononic lattice studied here. Namely, unlike fermions, bosonic structures do not have Kramer's degeneracy under time reversal symmetry. Likewise, their eigenmodes are *vector* valued fields, rather than the scalar fields of the Schrodinger equation. Finally, the vector nature of the fields implies a polarization degree of freedom, which gives rise to different constraints at the Γ point [92].

Regarding time reversal invariance, we will simply note that the systems under study here, phononic and photonic alike, belong to the AI group of the usual Altland-Zirnbaur classification [60, 61]. This setting is naturally more limited in possible topological phases, as the lack of spin-orbit coupling shrinks the set of nontrivial atomic insulator bases [88].

The second difference, the vectorial nature of the fields, simply requires an alteration of the calculation of the symmetry eigenvalues χ_g. Namely, a scalar field $u(\mathbf{r})$ transforms under a

symmetry group element g as

$$gu(\mathbf{r}) = u(R^{-1}\mathbf{r}). \tag{6.5}$$

In the above, R is the matrix representation of the group element g. For vector fields $\mathbf{u}$, the transformation must also consider the basis of unit vectors, giving

$$g\mathbf{u}(\mathbf{r}) = (g\mathbf{u})(R^{-1}\mathbf{r}), \tag{6.6}$$

where the term $(g\mathbf{u})$ denotes that we must apply the symmetry on the basis vectors ($\mathbf{a}_x, \mathbf{a}_y, \mathbf{a}_z$ for what follows).

The last feature of the bosonic implementation of symmetry indicators, that of the polarization, has been studied at length in Ref. [92]. The primary conclusion is that the polarization vortex that occurs at the Γ point leads to difficulties with clearly defining the irrep content $\mathbf{n}$, but can be removed via suitably introducing a fictitious zero mode. Moreover, for phononic systems, which possess both longitudinal as well as transverse wave solutions, this vortex does not occur, and we may safely compute the irreps as usual.

A perk of such tools is there computational simplicity and efficiency. Requiring only a small number of unit cell simulations for periodic boundary conditions, the topological classification can be very simple [69]. However, as should also be clear, the number of group-theoretic steps is somewhat large, and there are currently few tools to perform these symmetry operations in a general, 3D vector fields setting. To help alleviate this, we have written a software package [3] which automates many of these tedious operations. The software simply takes in a set of eigenvalue data and corresponding space group information, and computes symmetry data and indicator.

[3] Available soon on the Applied Electromagnetics GitHub page, https://github.com/Applied-Electromagnetics-Lab

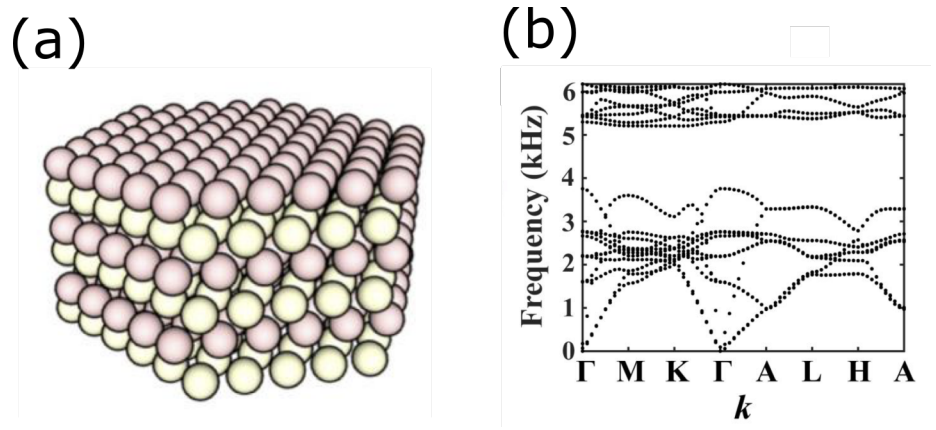

Figure 6.1: The phononic HCP lattice. (a) The HCP lattice structure, with layers A and B colored separately. (b) The phononic bandstructure of the model under study. Adapted from [93].

6.3 Application of the Method to 3D Phononic Crystal in a HCP Lattice

With the tools available, we may now proceed to analyze the example system, which is a hexagonal close packed (HCP) lattice of metal spheres embedded in an elastic medium, shown in Fig. 6.1(a). The phononic bandstructure is given in Fig. 6.1(b). Full details of the system will be provided in a future publication [93]. For our purposes, we will merely summarize the key features of this system, then proceed with the symmetry indicator analysis as an example:

- The system has a bulk phononic bandgap near 5 kHz
- The system (space group 196) has both inversion symmetry and time reversal symmetry, implying triviality of the Berry curvature and related Chern numbers.
- 2D sheets of the material are likewise trivial as far as the usual topological classification is concerned.
- When a screw dislocation of Burgers vector $\mathbf{B} = c\mathbf{z}$ (a full period in the z direction) is induced in the lattice, unidirectional modes are found within the bulk band gap. These have

been found both in simulation as well as in measured samples.

The above properties raise a question: if the system is otherwise trivial, how do the helical modes appear in the screw dislocation? Past studies have shown that screw dislocations do indeed result in nontrivial modes [94], but these efforts have focused mostly on spinfull systems in the AII Altland-Zirnbaur class, and critically hinge on the existence of spin-orbit coupling. Likewise, many past studies have shown that stacks of nontrivial 2D topological insulator models, even in class AI, may possess nontrivial modes at dislocations [95, 96], but still require the 2D system's nontriviality. In the present HCP lattice, such is not the case, being fully trivial for all 2D surfaces.

Since the unidirectional modes appear only via the inclusion of the screw axis, the next question is whether the model possesses a nontrivial symmetry indicator which is left unbroken by the screw axis. Such a case would then explain the observed modes. To check, we may compute the vector **n** for the model using the tools of the previous section. We find it as

$$\mathbf{n} = [0,2,2,0,4,4,6,6,2,2,8,6,6,2,2,8,4,4,4,0,0,0]. \tag{6.7}$$

If we then expand this onto the AI basis A for space group 194, we find all values of $\mathbf{q}$ are integers, implying triviality. Moreover, we can predict this in advance, given knowledge that the symmetry indicator group for spinless systems with TRS in space group 194 is given by $\mathbb{Z}_1$, which is automatically trivial [24]. Hence, we see that the specific HCP phononic bulk crystal is trivial by a wide range of classification tools, implying a special feature of the screw dislocation.

6.4 Screw Discontinuities and Modification of the Atomic Insulator Basis

Since symmetry indicator (as well as all other topological markers) imply triviality of the bulk crystal, we must examine further how the introduction of a screw dislocation influences the

system. In Ref. [94], a special index was derived that links the Burgers vector $\mathbf{B}$ with the weak index $\mathbf{G_v}$ to determine the existence of nontrivial modes along the screw axis, given as

$$\Theta = \frac{1}{2\pi}\mathbf{G_v} \cdot \mathbf{B}. \tag{6.8}$$

They showed that when this value is nonzero, a pair of helical modes will be trapped in the bulk bandgap. However, this index assumes a nonzero value of the weak index, which, in the case of systems in AI with time reversal symmetry, are automatically zero.

We may instead observe that the introduction of the screw discontinuity into the otherwise trivial crystal structure acts to lower the allowed symmetries of any mode near the defect line. Specifically, we can see that the there is an induced chirality, in the sense that all rotational eigenvalues must necessarily follow the helicity of the screw discontinuity. This is most relevant at the A point in the BZ, which corresponds to the top hexagonal surface. At this point, the structure factor vanishes, and there is an enforced "sticking together" of bands (see Table 6.4). Along the path $\Gamma \to A$ the C_3 eigenvalue must be maintained, but the resulting bands combine once the A point is reached.

Inducing the screw, the C_3 operation splits into the two values, one corresponding to a positive Burgers shift, the other to a negative Burgers vector. As the two bands at A can no longer maintain the same degenerated eigenvalue, the chiral mode "splits", leading to a band inversion. As a result, there will necessarily exist two helical modes trapped at the screw dislocation, with their direction locked to the direction of the screw and which span the bandgap.

Such modes are robust insofar as the two helical directions cannot directly couple, provided the bulk bandgap is maintained, although they naturally obey time reversal symmetry. This is also clear from the inability of a mode to discontinuously flip its C_3 eigenvalue without sufficiently large energy. In fact, this behavior has been shown numerically as well, see Ref. [93].

6.5 Discussion

This chapter has considered the application of symmetry indicator methods to a specific system in bosonics. Using theoretical considerations of the symmetry properties, as well as direct numerical calculations of the phononic bands, that such a system appears trivial at first glace, but the introduction of a screw discontinuity results in topologically robust modes along the defect line. This is in sharp contrast to previous efforts [94], where there is always an assumption of either weakly coupled 2D systems possessing inherent topology, or the requirement of a spin-orbit coupling, neither of which is the case here.

6.6 Appendix: Symmetry Eigenvalues and Irreps of the HCP Phononic Lattice

In this section we provide the full listing of calculated symmetry eigenvalues and resulting irrep classifications of the HCP phononic lattice examined in the previous sections. Note that the number of bands, 12, matches the expected minimum band connectivity as predicted by Ref. [92].

This chapter is partially based on the following paper: Y. Zhou, R. J. Davis, L. Chen, E. Wen, P. R. Bandaru, and D. F. Sievenpiper. “Helical Phononic Modes Induced by a Screw Dislocation”. In preparation, 2023. The dissertation author was the primary author of this material.

Table 6.1: Symmetry eigenvalues and corresponding irreps for the 12 modes below the bandgap at the Γ HSP, which has D_{6h} symmetry.

Element Mode	$\{E\|0\}$	$\{C_2\|\tau\}$	$\{C_3^+\|0\}$	$\{C_6^+\|\tau\}$	$\{C_2'^A\|\tau\}$	$\{C_2''^A\|0\}$	$\{i\|\tau\}$	$\{\sigma_h\|0\}$	$\{S_6^+\|\tau\}$	$\{S_3^+\|0\}$	$\{\sigma_d^A\|0\}$	$\{\sigma_v^A\|\tau\}$	Irrep
1	1	1	1	1	-1	-1	-1	-1	-1	-1	1	1	Γ_2^-
2 3	2	-2	-1	1	0	0	-2	2	1	-1	0	0	Γ_5^-
4 5	2	2	-1	-1	0	0	2	2	-1	-1	0	0	Γ_6^+
6 7	2	2	-1	-1	0	0	-2	-2	1	1	0	0	Γ_6^-
8	1	-1	1	-1	1	-1	-1	1	-1	1	-1	1	Γ_3^-
9	1	1	1	1	-1	-1	1	1	1	1	-1	-1	Γ_2^+
10 11	2	-2	-1	1	0	0	2	-2	-1	1	0	0	Γ_5^+
12	1	-1	1	-1	1	-1	1	-1	1	-1	1	-1	Γ_3^+

Table 6.2: Symmetry eigenvalues and corresponding irreps for the 12 modes below the bandgap at the M HSP, which has D_{2h} symmetry.

Element Mode	$\{E\|0\}$	$\{C_2\|\tau\}$	$\{C_2'^A\|\tau\}$	$\{C_2''^A\|0\}$	$\{i\|\tau\}$	$\{\sigma_h\|0\}$	$\{\sigma_d^A\|0\}$	$\{\sigma_v^A\|\tau\}$	Irrep
1	1	1	-1	-1	1	1	-1	-1	M_2^+
2	1	-1	1	-1	1	-1	1	-1	M_3^+
3	1	-1	1	-1	-1	1	-1	1	M_3^-
4	1	1	-1	-1	-1	-1	1	1	M_2^-
5	1	-1	1	-1	1	-1	1	-1	M_3^+
6	1	1	-1	-1	1	1	-1	-1	M_2^+
7	1	-1	1	-1	-1	1	-1	1	M_3^-
8	1	-1	-1	1	1	-1	-1	1	M_4^+
9	1	1	-1	-1	-1	-1	1	1	M_2^-
10	1	1	1	1	-1	-1	-1	-1	M_1^-
11	1	-1	-1	1	-1	1	1	-1	M_4^-
12	1	1	1	1	1	1	1	1	M_1^+

Table 6.3: Symmetry eigenvalues and corresponding irreps for the 12 modes below the bandgap at the K HSP, which has D_{3h} symmetry.

Element Mode	$\{E\|0\}$	$\{C_3^+\|0\}$	$\{C_2'^A\|\tau\}$	$\{\sigma_h\|0\}$	$\{S_3\|0\}$	$\{\sigma_v^A\|\tau\}$	Irrep
1 2	2	-1	0	-2	1	0	K_3^-
3	1	1	-1	1	1	-1	K_2^+
4 5	2	-1	0	2	-1	0	K_3^+
6	1	1	-1	-1	-1	1	K_2^-
7 8	2	-1	0	-2	1	0	K_3^-
9	1	1	1	-1	-1	-1	K_1^-
10 11	2	-1	0	2	-1	0	K_3^+
12	1	1	1	1	1	1	K_1^+

Table 6.4: Symmetry eigenvalues and corresponding irreps for the 12 modes below the bandgap at the A HSP, which has C_{3v} symmetry.

Element Mode	$\{E\|0\}$	$\{C_3\|0\}$	$\{\sigma_d\|0\}$	Irrep
1 2 3 4	4	-2	0	A_3
5 6 7 8	4	-2	0	A_3
9 10	2	2	-2	A_2
11 12	2	2	2	A_1

Table 6.5: Symmetry eigenvalues and corresponding irreps for the 12 modes below the bandgap at the H HSP, which has D_{3h} symmetry. The two values for the improper rotation are complex conjugates of each other, and so are listed separately.

Element Mode	$\{E\|0\}$	$\{C_3^+\|0\}$	$\{C_2'^A\|\tau\}$	$\{\sigma_h\|0\}$	$\{S_3^+\|0\}$	$\{S_3^-\|0\}$	$\{\sigma_v^A\|\tau\}$	Irrep
1 2	2	-1	0	0	$-\sqrt{3}i$	$+\sqrt{3}i$	0	H_1
3 4	2	-1	0	0	$+\sqrt{3}i$	$-\sqrt{3}i$	0	H_2
5 6	2	1	0	0	0	0	0	H_3
7 8	2	-1	0	0	$+\sqrt{3}i$	$-\sqrt{3}i$	0	H_2
9 10	2	1	0	0	0	0	0	H_3
11 12	2	-1	0	0	$-\sqrt{3}i$	$+\sqrt{3}i$	0	H_1

Table 6.6: Symmetry eigenvalues and corresponding irreps for the 12 modes below the bandgap at the L HSP, which has D_{2h} symmetry.

Element Mode	$\{E\|0\}$	$\{\sigma_d\|0\}$	Irrep
1 2	2	2	L_1
3 4	2	-2	L_2
5 6	2	-2	L_2
7 8	2	2	L_1
9 10	2	2	L_1
11 12	2	-2	L_2

Chapter 7

Real Space Topology

There is an important connection between the physics of non reciprocity in periodic systems and the global topology of their bandstructure. Symmetry protected phases, including time reversal symmetry, chiral, and crystallographic have yielded innumerable topologically robust systems. A chief interest in these platforms has been their intrinsic robustness to the microscopic properties of their bulk. Photonic crystals have proven a simple platform to explore these forms of topological phases [6], which is the strategy we have employed for most of this dissertation.

The majority of the analysis presented so far has focused on analyzing the properties that possess some form of periodicity, but what if this cannot be established? There are many cases, such as amorphous systems [27, 97, 98], quasicrystalline systems [99, 100], and single defect states [101, 102, 103], which *cannot* be fully understood using purely reciprocal space methods. Tools such as the Bott index [99], Kitaev sum [26], and the local Chern marker [104] have proven useful in these settings, though full application of them remains a challenge in continuous systems.

In this chapter we study the effects of *both* forms of topology, real and reciprocal, on a time reversal symmetric photonic topological insulator platform, and reveal how the combined

topologies manifest in different measurable settings. Our primary platform will be the pseudospin-type duality cell explained in Chapter 3, and the main tool to analyze its behavior will be the Kitaev sum, described in Chapter 2.

7.1 Momentum Space Analysis

The model used here is the C_{6v}-symmetric unit cell employing electromagnetic (EM) duality, as demonstrated in Ref. [38], which has the bandstructure shown in Fig. 7.2(c). This model emulates the quantum spin Hall effect via the construction of pseudospin states composed of electric and magnetic fields via anisotropic coupling. Full details of the physics of this model can be found in Ref. [38].

We will be using this unit cell for two reasons:

1. The system is time reversal symmetric, and therefore does not require external magnetic fields or exotic materials. This makes for simpler experimental demonstrations, and

2. Although the cell is properly 3 dimensional, the effective topology exists in the form of the surface waves existing on the thin structures. As such, the behavior can be considered as 2D, permitting the full range of possible computational and experimental techniques developed for such systems.

To begin with, we can first characterize the model purely in reciprocal space, the result of which can be found in the supplemental material to Ref. [6]. The two spin-polarized bands display Berry curvature similar to those seen in topological insulators of electronic systems (e.g., those of Bi2Te3 and other compounds). Spikes are observed at the K/K' points, each with the same sign and magnitude. Integration of the curvature over the full BZ results in spin Chern numbers [1] come out to ± 1 for the pseudospin states $\psi^{\pm}$.

[1] Note that in this case there is no effective coupling terms equivalent to Rashba coupling, and as such the spin Chern number matrix [20] is diagonal and can be considered separately

This accumulation predicts robust surface states on interfaces of the material, which are indeed observed on properly chosen interfaces.

7.2 Real Space Analysis

The previous section examined the behavior of a periodic lattice of unit cells. In this section we employ a different method, here called the Kitaev sum, which can be likened to a Chern number localized to real space [26]. The benefit of this tool is that it permits us to probe the topology for *finite* systems, including those with defects or other breaks to the global symmetry.

7.2.1 The Kitaev Sum

Formally, the Kitaev sum is given by a sum of projector elements $P_{\alpha\beta}$ as [26, 27, 105]

$$C^{\mu} = 12\pi i \sum_{\alpha\in A,\beta\in B,\gamma\in C} (P^{\mu}_{\alpha\beta}P^{\mu}_{\beta\gamma}P^{\mu}_{\gamma\alpha} - P^{\mu}_{\alpha\gamma}P^{\mu}_{\gamma\beta}P^{\mu}_{\beta\alpha}). \tag{7.1}$$

In the above, $P^{\mu}_{\alpha\beta}$ is the projector element between sites α and β over a full band μ. Each of these points are chosen from three equal domains A, B, C, as illustrated in Fig. 7.1. Concretely, for an electromagnetic system we can define the projector elements as the sum over eigenfrequencies for pairwise locations of the chosen lattice as

$$P^{\mu}_{\alpha\beta} = \sum_{E_n\leq E_f} \phi(r_\alpha)\phi(r_\beta)^*. \tag{7.2}$$

Here, α and β are both points in the chosen region (e.g., $\alpha = (x_\alpha, y_\alpha)$ on a Cartesian grid). Within the usual tight binding methods these projectors are simply lattice sites, but for our purposes these projectors are *continuously defined*, since the electromagnetic modes themselves are spatially extended. Hence, within numerical calculations we must choose a sampling of the real space axis

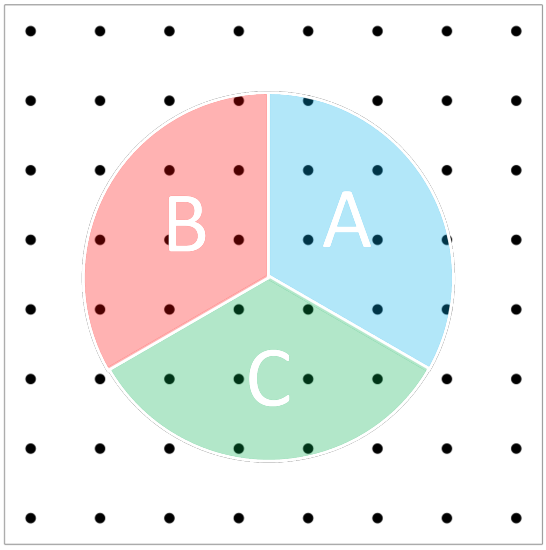

Figure 7.1: The computational domain of the Kitaev sum calculation. The three regions A, B, C are arbitrary in shape but roughly equivalent in area. The sum corresponds to the "real space Chern number" localized to the point where the three regions intersect.

that is sufficiently dense to resolve the behavior (see Section 7.6 for details).

To verify the expected behavior of the Kitaev sum, we may construct a finite sample of the base unit cells and apply closed boundary conditions (here we use perfect electric BCs, but others are possible). The geometry of such a sample is shown in Fig. 7.2(a). Corresponding eigenmodes are given in Fig. 7.2(d). We note a few features:

1. The exact geometry of the bulk (e.g., the shape of the edges) does not matter, provided there are enough cells included in the simulation.

2. The full-wave simulation reveals states within the expected bandgap region, which correspond to the edge modes excited on the outside boundary.

3. As the pseudospin degree of freedom is only weakly maintained, there are more modes within the bandgap that correspond to spurious numerical artifacts. They can be removed by tuning the edge geometry.

Using this data, we may then compute the Kitaev sum of Eq. (7.1), selecting a single

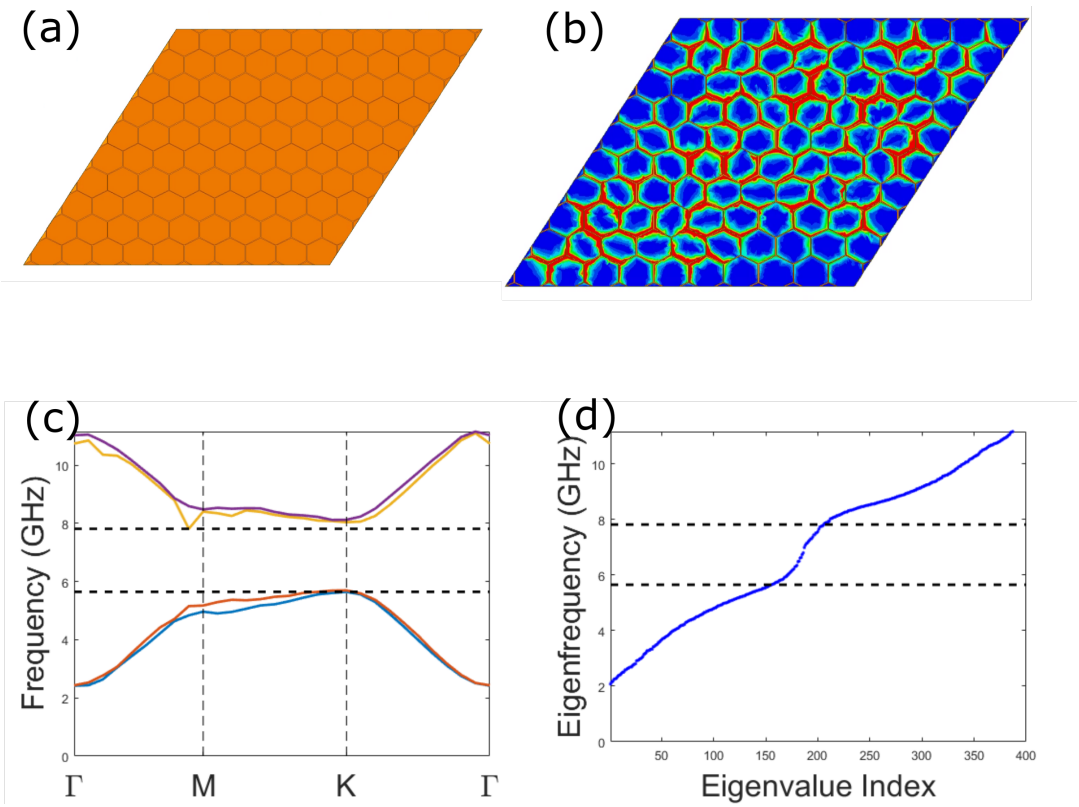

Figure 7.2: Spin-type photonic topological insulators on a finite lattice. (a) The supercell model of EM duality unit cells. (b) A typical eigenmode of the supercell for modes in the bulk spectra, showing the complex magnitude of the electric field. (c) The periodic unit cell band structure, with the expected two-fold degeneracy above and below the fundamental bandgap. The horizontal black lines denote the bandgap. (d) The supercell eigenspectra. Note that the bandgap region possesses a continuum of states, which correspond to the nontrivial topological modes.

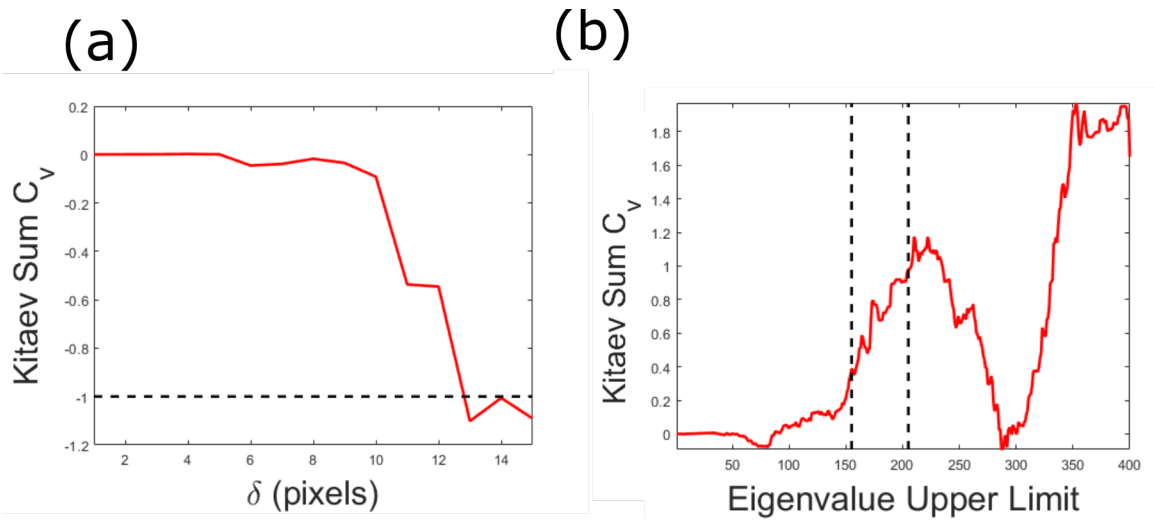

Figure 7.3: The Kitaev sum as applied to the duality spin cell on a finite sample. The simulated model is as shown in Fig. 7.2(a). (a) Kitaev sum convergence behavior taken in the middle of the simulated region as a function of the included bulk size δ, measured in pixels for an 81x81-sized domain. The black horizontal line is the expected spin Chern number of -1. (b) Behavior of the Kitaev sum as we increase the upper eigenlimit E_f. The region between the black vertical lines denotes the topological bandgap.

point at the center as the center of the computational domain. An example of sum vs included bulk size is given in Fig. 7.3(a), and against eigenspectra in Fig. (7.3)(b). We see that once a sufficient bulk is included, in Fig. 7.3(a) denoted by the side length δ, measured in pixels for a 81x81 sized data set, the value converges towards the bulk integer. For Fig. (7.3)(a), the input data were those of the hybrid spin down values, which have an expected spin Chern number of -1, which is reached when > 12 pixels is included in the computational domain. Fig. (7.3)(b) shows the computation for the spin up mode, which has a spin Chern number of +1. As the bulk size chosen here is $\delta = 11$, the value does not completely converge within the bandgap (denoted by the vertical lines), but as δ increases this behavior stabilizes. The behavior at values past eigenvalue 300 are from higher bands, which are not of interest here.

7.2.2 Adding Real Space Defects: The 5-Sided Inclusion

Although the previous sections of this chapter have used finite lattices, the underlying physics is still dominated by the behavior of the periodic unit cell underlying them. In this section, we show the result of applying the Kitaev some to a model with a special defect, which possesses topological characteristics in the real space.

If we apply the Volterra process to remove a sector of a hexagonal lattice, at the center we are left with a single pentagon surrounded by hexagons, Fig. 7.4(a). Far from the center, the hexagons are otherwise close to symmetric, and become increasingly regular the farther from the defect they become. Hence, such a defect is a *real space topological* defect [101, 102, 103]. As detailed in Ref. [101], such disclinations naturally have fractionalized charge behavior, with modes appearing in the center defect and remaining finite corners.

However, what is not immediately clear is what we should expect when we form the lattice not from a trivial unit cell lattice (e.g., like in [102]), but one made from a nontrivial topological lattice. Using the Kitaev sum, which can be localized for sufficient bulk sizes [27], we may observe the nonreciprocal pseudospin flow in the model, while including the real space defects. The results of such a calculation are shown in Fig. 7.4(b). Here 10% of the bulk is included, which is large enough to converge for the periodic case with expected spin Chern number of -1. We can see that for much of the bulk, far from the center, the value pushes towards the expected bulk value[2]. Meanwhile, at the center and towards the edges we see a large *positive* accumulation, caused by the *real space* defects.

The flipping of sign can be interpreted as a result of the trapped states at the defects naturally possessing a chirality that opposes that of the bulk. This behavior has been observed in models of different reciprocal space topology [106], though here the effect is seen from the view of a spin degree of freedom. Hence, when we connect real space defects together, as done in Ref.

[2]The top/bottom asymmetry is a numerical artifact caused by the finite number of modes chosen. If the mesh size is increased, or the model scaled appropriately, such fluctuations will eventually cancel out.

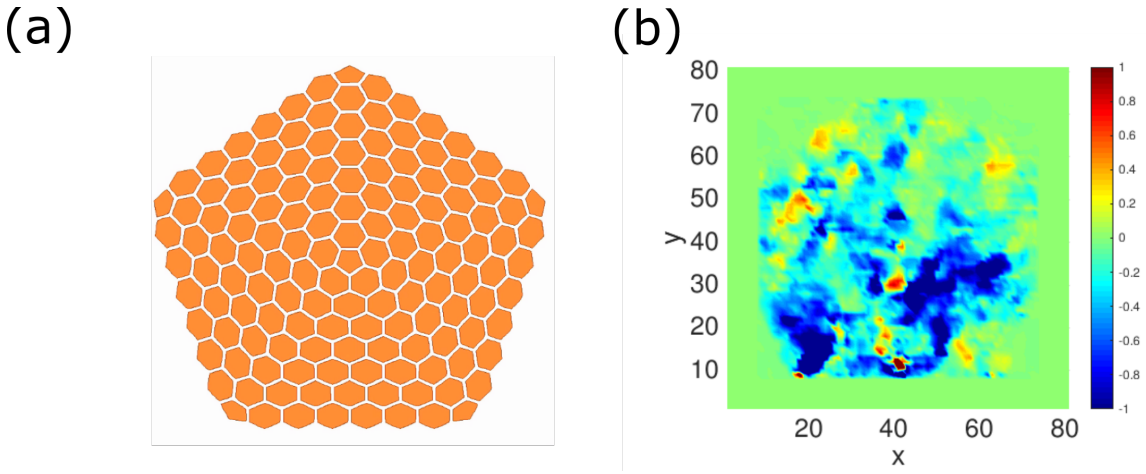

Figure 7.4: Combined real and reciprocal space defects. (a) A lattice of the 6-fold symmetric unit cells placed into a supercell, with a $1/6$ sector removed via the Volterra process. This results in nearly regular hexagonal unit cells everywhere except the geometric center, where the center cell is a heptagon. (b) The spatially resolved Kitaev sum for a fractional bulk inclusion of 10% and a lattice discretization of 81×81. The upper eigenvalue limit E_f is chosen to be at the upper end of the bandgap, including both center and corner states.

[106], we are constructing a topologically stable region for the spin states to propagate through, which is protected by both the real space nature of the defect as well as the underlying reciprocal space topology of the unit cell. The Kitaev sum shows this directly.

7.2.3 Amorphous Defect States

As mentioned, a major benefit of the locality of the Kitaev sum is that it permits us to weaken the lattice periodicity condition further still. Specifically, we can make the model in Fig. 7.4 semi-amorphous, breaking the C_{6v} symmetry that was retained far from the center and edges, as shown in Fig. 7.5(a). In such a case, the only symmetry retained are the internal EM duality as well as time reversal symmetry; all others are effectively broken. Nevertheless, the lattice behavior is retained enough to maintain the bulk bandgap behavior. The eigenspectra for this supercell is shown in Fig 7.5(b), where we observe a near continuum of states within the expected bandgap region. This differs from the semi-uniform defect model of the previous section, as the amorphous behavior results in numerous trapped states. These states are real-space in origin, like

the center defect, but are not tightly pinned (e.g., a small deformation may shift their location or frequency). The center and corner modes remain pinned, however.

We can then perform the same Kitaev sum analysis, scanning over the region to observe the behavior. As in the regular sample, we can choose to either include or exclude the center defect states via the upper eigenlimit E_f. However, as there are many additional trapped states within the bandgap, we will naturally get extra Chern accumulation at various points where these modes arise. This is seen in Fig. 7.5(c), where we have set the upper eigenlimit well within the bulk bandgap, but stopped before including the center and corner modes. As a result, we observe that most of the bulk displays the expected 1/2 value, but as it drifts towards different regions of more trapped states the value fluctuates. We still do not see a strong center mode.

If we then increase the upper eigenlimit to include the genuine defects, we then see a large spike in the Kitaev sum, seen in Fig. 7.5(d). The accumulation at the center directly corresponds to the topologically trapped defect states existing within the continuum of the (reciprocal) topological bandgap. Hence, we are able to observe the topology of the material arising from both real and reciprocal space effects, even in systems of dramatically reduced symmetry.

7.3 Measurements

To show that the previous simulation results are physically accurate, we have fabricated and measured a set of samples corresponding to the semi-uniform defect models shown in Fig. 7.4. The 5-sided defect model is shown in Fig. 7.6(a), and for the 7-sided is shown in Fig. 7.6(c). As expected, we observe trapped states for both, with the 7-sided modes clearly showing quadrupolar modes. The 5-sided should show dipolar modes, but this is made difficult to observe owing to the size of the same and the resolution of the near-field scanner. In the 5-sided model we also show the corner states, which are near enough to the source excitation to be visible for

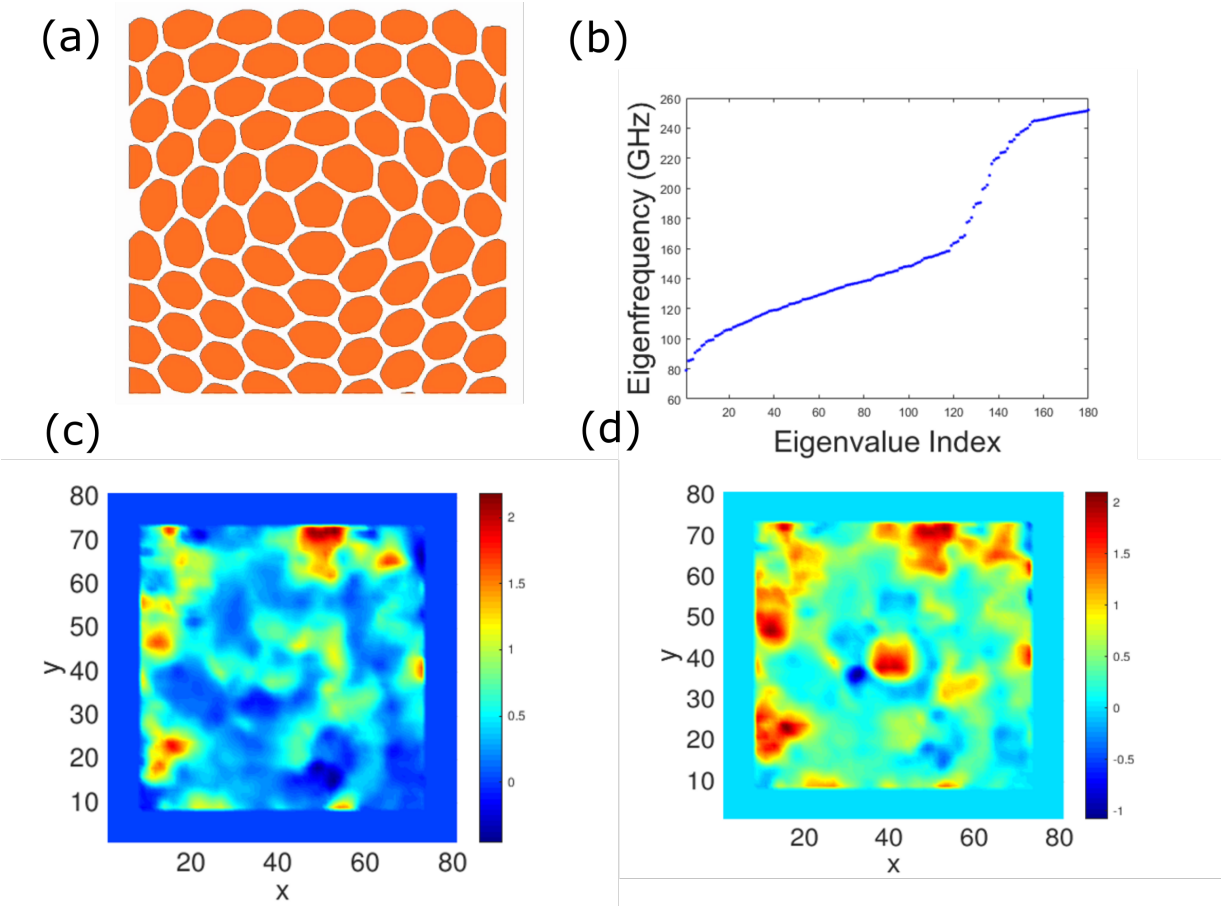

Figure 7.5: Amorphous combined topology states. (a) A 5-sided defect lattice, where the shapes of all unit cells is made semi-amorphous, breaking all long and short range periodicity. (b) The eigenspectra of the supercell, which includes a more continuous spectrum of eigenstates within the bulk bandgap. (c) The spatially resolved Kitaev sum for an upper eigenlimit E_f below the center states. The bulk region only displays the bulk (reciprocal) topology. (d) The spatial Kitaev sum with E_f including the center states. Here the center region contains a large build up, corresponding to the real space topology of the defect.

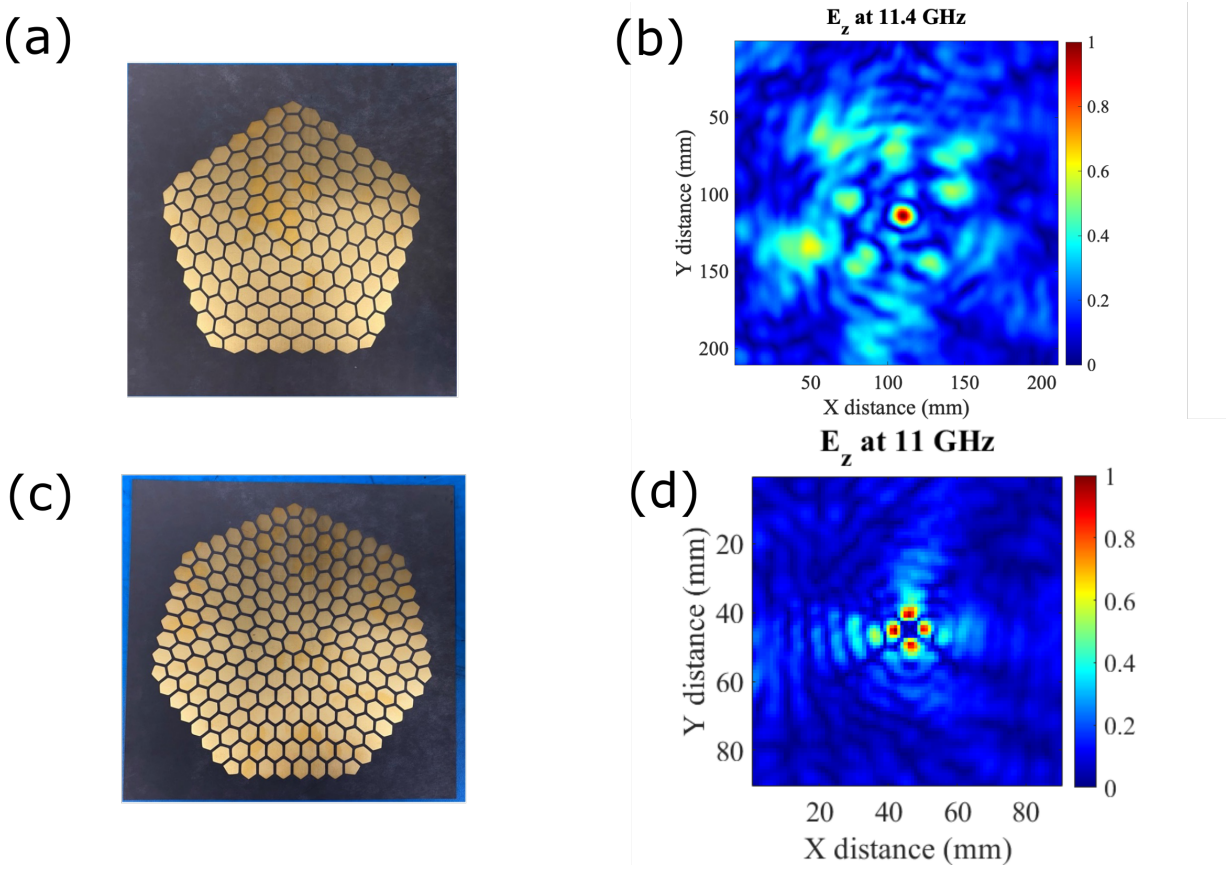

Figure 7.6: Measured defect states. (a) and (b) show the fabricated models for the 5 and 7-sided defect models, respectively. Note that only the top surface is shown, and the bottom layer is the geometric dual. (b) and (d) show the measured magnitude of the z component of the electric field E_z 1 mm above the top surface. In both cases the excitation probe was placed near the center defect. The 7-sided defect clearly shows the expected quadropole modes, while the smaller 5-sided model shows the dipolar modes (smeared together due to the spatial resolution), as well as the corner states.

this measurement. In the 7-sided case, the bulk size is large enough for these to be too weak to observe.

7.4 Tomographic Retrieval of Chern Numbers

A powerful feature of the Kitaev sum is that it permits a formulation that is measurable on an experimental platform. This is significant, since the experimental retrieval of topological invariants is very challenging. This process uses a tomographic technique as detailed in Ref.

[107] and [108], and is an area for future work.

7.5 Discussion

This chapter has demonstrated an electromagnetic system with *dual topologies*, both real and reciprocal, and shown their behavior via the Kitaev sum. This has revealed a number of interrelated phenomena, all in the same platform:

1. The base unit cell, the EM duality cell of Ref. [38], naturally possesses a pseudospin degree of freedom, for which we find a nontrivial reciprocal space topology of its bandstructure.

2. Placing this into a finite lattice, we can observe the bulk behavior via the Kitaev sum, which can be localized in space and is insensitive to boundary conditions.

3. Inducing a real space defect via a Volterra process results in trapped modes of real origin. Such states cannot be removed unless annihilated by a paired defect of one dimension higher or lower (e.g., a 5 sided defect merging with a 7 sided defect).

4. Such real space modes are required to have greater than monopolar charge. As such, we see bipolar and above, always in paired values.

5. The application of the Kitaev sum allows us to see how the dual topologies interact, with a large nonreciprocal build up occurring at the center of the defect.

6. Such effects are robust to a wide range of deformation, even in nearly amorphous settings.

One possible consequence of the build up of the Kitaev sum for the real space defect is in 3D stacking: if the 2D sheets of Fig. 7.4 are stacked along the out-of-plane z axis, strong coupling may result in a unidirectional mode propagating chirally along the defect. This is similar to the 3D phononic lattice examined in Chapter 6, but here the chirality is induced by the electromagnetic spin DOF, and constrained by the real space defect.

Another possibility is in examining the behavior of other finite systems. It is known that inducing 5 and 7 sided defects on the same finite lattice creates robust propagation channels, but the mechanism causing them has so-far been not fully studied. This is an ideal candidate for the spatially resolvable Kitaev sum, where the relative strength of nonreciprocal effects throughout the system can be plotted directly in real space.

A final option for this system and related analysis tools is in the area of quantum quench dynamics [109]. As the Kitaev sum can be measured experimentally [107], it is possible to construct a physical system using a suitably modified copy of the model in Fig. 7.4 (e.g., using diodes to ground different patches) which can be modulated in time to study the effects of dynamic changes in topology. These are ordinarily very challenging to see outside of simple toy models, which makes the platform here enticing.

7.6 Appendix: Example of the Kitaev Sum for a Chern Insulator PTI Model

To observe the computational aspects of the Kitaev sum as used on continuously defined models, like the electromagnetic ones shown in the main text, in this section we explore the celebrated Chern insulator model based on the work of Ref [110]. In Fig. 7.7 is shown the unit cell, which is a circular rod of YIG with period $a = 20$ mm, radius $r = 0.3$ mm, with the rest of the material made of vacuum. The top and bottom surfaces are set to perfect magnetic boundary conditions, to emulate an infinite 2D lattice. The corresponding band structure is shown in Fig. 7.7(c), with bandgaps denoted by the horizontal lines.

Fig. 7.7(b) shows a finite lattice of size 20×20. Here the boundary conditions on the $x-y$ planes are set to perfect electric BCs, but we note here that this is arbitrary, and the calculation will work for any BC provided enough unit cells are included. The corresponding eigenspectra for the full lattice is shown in 7.7(d). Note that the first bandgap does not have any states, while

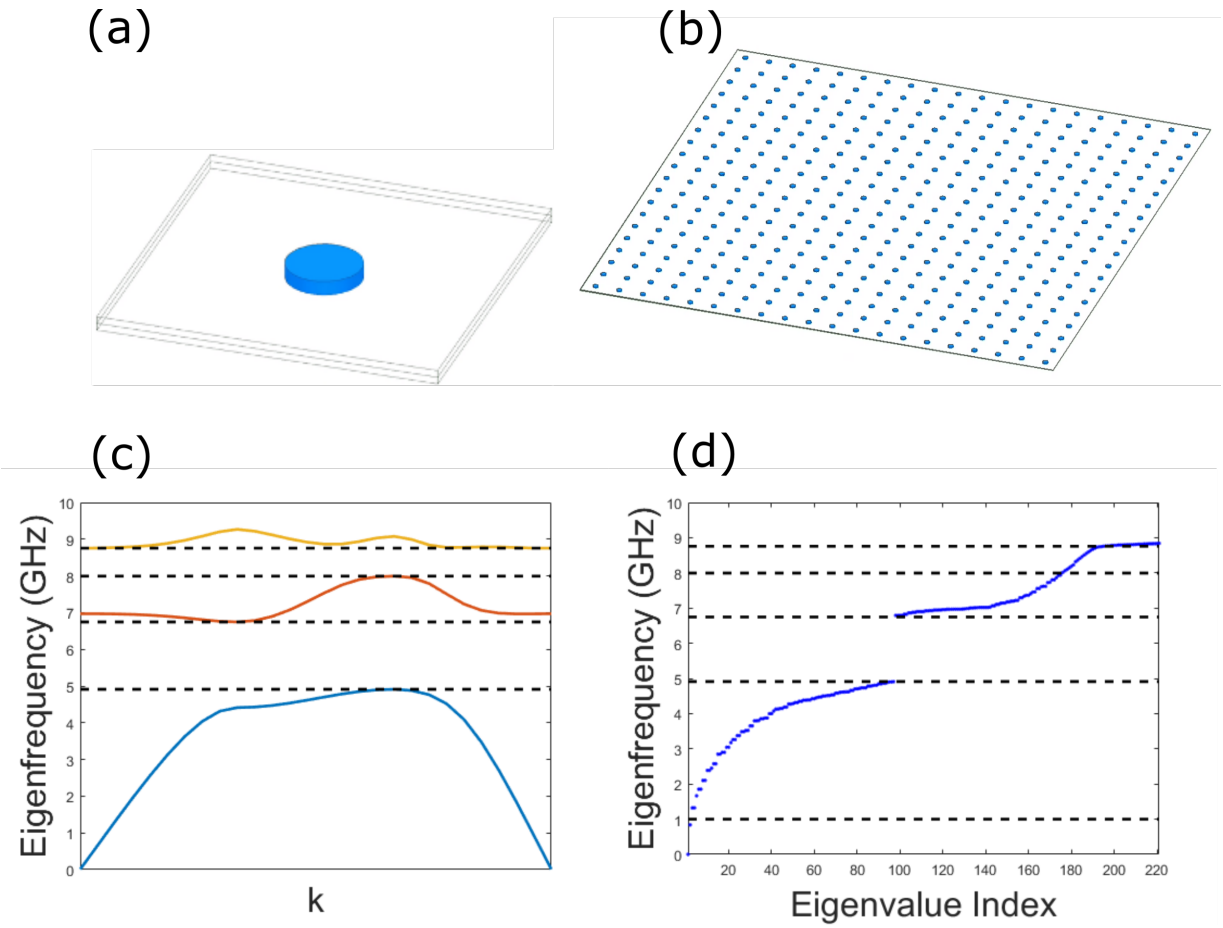

Figure 7.7: A Chern-type PTI model. (a) The periodic unit cell of YIG rods in a 2D lattice. (b) The finite lattice model. (c) The periodic band structure for the unit cell in (a). The second bandgap has (gap) Chern number of 1. (d) The eigenspectra of the finite model. Note that there are no states within the (trivial) first bandgap, while a continuum appears in the second (nontrivial) bandgap.

the second, topological bandgap has a continuum. These upper bandgap states represent the edge modes caused by the Chern insulator topology.

Using the field data of the finite lattice, we can calculate the Kitaev sum using a single point centered on a rod in the middle of the lattice. Knowing that we expect the (periodic) Chern number to be nonzero for the upper bands, we can initially set the upper eigenlimit E_f to a value within the second bandgap. We are free to choose any so long as it contains the lower bands (see later sections for a discussion on this), and as such we will initially select the eigenvalue halfway into the bandgap.

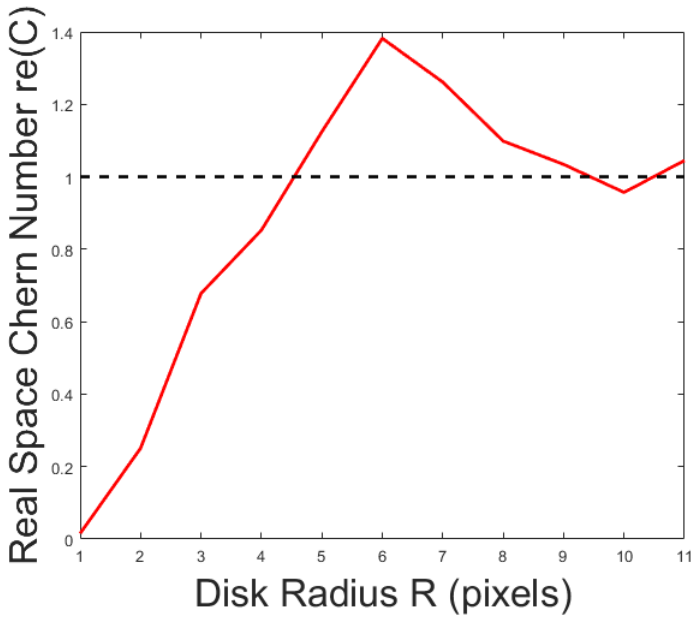

Figure 7.8: The convergence behavior of the Kitaev sum for the Chern-type model as a function of the size of the included bulk, using a fixed upper eigenlimit E_f within the second bandgap. The characteristic behavior shows a gradual rise, followed by a leveling out once sufficient sites are included within the computational domain. Here the calculation is performed for a region centered on a unit cell in the middle of the finite lattice.

The result of running the Kitaev sum calculation for increasing sizes of included bulk fraction is shown in Fig. 7.8. We see that the value initially rises, eventually saturating to the expected value of 1. There is overshoot, causes by the non-monotonic nature of the continuous calculation and discretized process. To see how this value manifests vs the eigenmode data being included (e.g., how E_f influences the computation), we can fix the fractional size of the bulk contained to a stable value of 40% and sweep E_f. The result is shown in Fig. 7.9

This chapter is based on the following paper: R. J. Davis, S. Singh, D. J. Bisharat, and D. F. Sievenpiper, "Topological Defects with Both Real and Reciprocal Space Signatures," In preparation, 2023. The dissertation author was the primary author of this material.

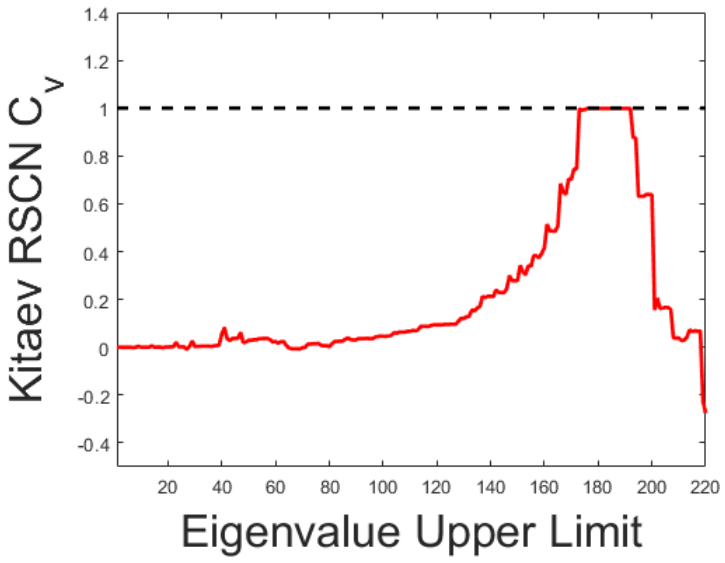

Figure 7.9: The convergence behavior of the Kitaev sum as a function of the upper eigenlimit E_f, assuming a fixed included bulk size of 30%. Note the value does not change significantly until the upper bands are reached, at which point the value plateaus upon reaching the nontrivial second bandgap.

Chapter 8

Summary and Discussion

8.1 Summary of Major Results

The unifying theme of this dissertation has been on the relationship between topological features in real and reciprocal space, and how we can use them to understand systems in practical settings. Much of the work presented here has made use of engineered crystals in classical wave systems, like photonics and phononics. Many of the tools, however, are general, and are explored here to illustrate the ease to which we can investigate features using these platforms.

The first chapters dealt with how we can use electromagnetic duality-based platforms to construct robust waveguides. Chapter 3 focused on a specific coupler design, which required an understanding of the inhomogeneous field behavior that topological structures give rise to. By carefully engineering the interface between the two domains, a highly efficient mode conversion was achieved. This naturally led to the work in Chapter 4, which dealt with lowering the crystal symmetry of the previous hexagonal model down to a rhombus. Doing so leads to a more useful design, having straight edges that can be more easily interfaced to other systems, but proved to have a far richer topology than initially expected. This was analyzed via reciprocal space tools, showing the behavior in Berry curvature, as well as via modifying the underlying Hamiltonian.

Crystal symmetries were used further in Chapter 5, where rotational eigenvalues and the gauge freedom of unit cell choice led to robust states in triangular lattices. This was shown using the modern tool set of symmetry indicators, which consider various symmetry-allowable states. Those same methods, suitably generalized, were then used again in Chapter 6, which covered an analysis of a hexagonal close packed structure with an induced screw discontinuity. Using the full space-group analysis of the bulk crystal, along with careful consideration of the preserved symmetries of the screw dislocation, we showed how the structure gives rise to robust edge states not readily explained by the standard theories.

All previous chapters worked with symmetries in both real and reciprocal space, but in Chapter 7 we show examples where such tool breakdown completely. Amorphous and defect states preclude any periodic explanation, even a perturbed one, and as such a different method, the Kitaev sum, was employed to probe their topology. It was shown that a rich set of topological signatures can be found via this method, where features with both fully real and fully reciprocal origins can be clearly probed. Such methods are even applicable to experimental platforms, which is rare for topological invariant calculations.

A major conclusion of this body of work is the both the value in using a wide range of topological analysis tools, as well as to point out the possibilities that classical wave and bosonic-based systems can have for demonstration. Practical applications generally stem from a clearer connection between pure theory (often worked out in the realm of electronic systems first) and the more concrete models employed here. Being able to calculate and utilize these theories to verify the topological origin, as well as gives clues to future designs.

Bibliography

[1] Xiao-Liang Qi and Shou-Cheng Zhang. Topological insulators and superconductors. *Reviews of Modern Physics*, 83(4):1057–1110, October 2011.

[2] C. L. Kane and E. J. Mele. Quantum Spin Hall Effect in Graphene. *Physical Review Letters*, 95(22), November 2005.

[3] Tomoki Ozawa, Hannah M. Price, Alberto Amo, Nathan Goldman, Mohammad Hafezi, Ling Lu, Mikael C. Rechtsman, David Schuster, Jonathan Simon, Oded Zilberberg, and Iacopo Carusotto. Topological photonics. *Reviews of Modern Physics*, 91(1):015006, March 2019.

[4] Hai-Xiao Wang, Guang-Yu Guo, and Jian-Hua Jiang. Band topology in classical waves: Wilson-loop approach to topological numbers and fragile topology. *New Journal of Physics*, 21(9):093029, September 2019.

[5] John Joannopoulos, Steven G. Johnson, Joshua N. Winn, and D. Meade Robert. *Photonic Crystals: Molding the Flow of Light*. Princeton University Press, March 2008.

[6] Dia'aaldin Bisharat, Robert Davis, Yun Zhou, Prabhakar Bandaru, and Dan Sievenpiper. Photonic Topological Insulators: A Beginner's Introduction [Electromagnetic Perspectives]. *IEEE Antennas and Propagation Magazine*, 63(3):112–124, June 2021.

[7] D. J. Thouless, M. Kohmoto, M. P. Nightingale, and M. den Nijs. Quantized Hall Conductance in a Two-Dimensional Periodic Potential. *Physical Review Letters*, 49(6):405–408, August 1982.

[8] F. D. M. Haldane. Model for a Quantum Hall Effect without Landau Levels: Condensed-Matter Realization of the "Parity Anomaly". *Physical Review Letters*, 61(18):2015–2018, October 1988.

[9] M. Z. Hasan and C. L. Kane. Colloquium: Topological insulators. *Reviews of Modern Physics*, 82(4):3045–3067, November 2010.

[10] Barry Simon. Holonomy, the Quantum Adiabatic Theorem, and Berry's Phase. *Physical Review Letters*, 51(24):2167–2170, December 1983.

[11] Mikio Nakahara. *Geometry, Topology and Physics*. CRC Press, Bristol ; Philadelphia, 2nd edition edition, June 2003.

[12] Yizhou Liu, Xiaobin Chen, and Yong Xu. Topological Phononics: From Fundamental Models to Real Materials. *Advanced Functional Materials*, 30(8):1904784, 2020.

[13] Yun Zhou, Prabhakar R. Bandaru, and Daniel F. Sievenpiper. Quantum-spin-Hall topological insulator in a spring-mass system. *New Journal of Physics*, 20(12):123011, December 2018.

[14] J. C. Slater and G. F. Koster. Simplified LCAO Method for the Periodic Potential Problem. *Physical Review*, 94(6):1498–1524, June 1954.

[15] Walter A. Harrison. *Electronic Structure and the Properties of Solids: The Physics of the Chemical Bond*. Dover Publications, New York, July 1989.

[16] Mike Finnis. *Interatomic Forces in Condensed Matter*. Oxford University Press, Oxford, June 2010.

[17] Michael Victor Berry. Quantal phase factors accompanying adiabatic changes. *Proceedings of the Royal Society of London. A. Mathematical and Physical Sciences*, 392(1802):45–57, March 1984.

[18] S. Ali Hassani Gangaraj, Mário G. Silveirinha, and George W. Hanson. Berry Phase, Berry Connection, and Chern Number for a Continuum Bianisotropic Material From a Classical Electromagnetics Perspective. *IEEE Journal on Multiscale and Multiphysics Computational Techniques*, 2:3–17, 2017.

[19] F Wilczek and A Shapere. *Geometric Phases in Physics*, volume 5 of *Advanced Series in Mathematical Physics*. WORLD SCIENTIFIC, July 1989.

[20] D. N. Sheng, Z. Y. Weng, L. Sheng, and F. D. M. Haldane. Quantum Spin-Hall Effect and Topologically Invariant Chern Numbers. *Physical Review Letters*, 97(3):036808, July 2006.

[21] Di Xiao, Wang Yao, and Qian Niu. Valley-Contrasting Physics in Graphene: Magnetic Moment and Topological Transport. *Physical Review Letters*, 99(23):236809, December 2007.

[22] A. Alexandradinata, Xi Dai, and B. Andrei Bernevig. Wilson-loop characterization of inversion-symmetric topological insulators. *Physical Review B*, 89(15), April 2014.

[23] Wladimir A. Benalcazar, Tianhe Li, and Taylor L. Hughes. Quantization of fractional corner charge in ${C}_{n}$-symmetric higher-order topological crystalline insulators. *Physical Review B*, 99(24):245151, June 2019.

[24] Hoi Chun Po, Ashvin Vishwanath, and Haruki Watanabe. Symmetry-based indicators of band topology in the 230 space groups. *Nature Communications*, 8(1):50, June 2017.

[25] Barry Bradlyn, L. Elcoro, Jennifer Cano, M. G. Vergniory, Zhijun Wang, C. Felser, M. I. Aroyo, and B. Andrei Bernevig. Topological quantum chemistry. *Nature*, 547(7663):298–305, July 2017.

[26] Alexei Kitaev. Anyons in an exactly solved model and beyond. *Annals of Physics*, 321(1):2–111, January 2006.

[27] Noah P. Mitchell, Lisa M. Nash, Daniel Hexner, Ari M. Turner, and William T. M. Irvine. Amorphous topological insulators constructed from random point sets. *Nature Physics*, 14(4):380, April 2018.

[28] Zheng Wang, Yidong Chong, J. D. Joannopoulos, and Marin Soljačić. Observation of unidirectional backscattering-immune topological electromagnetic states. *Nature*, 461(7265):772–775, October 2009.

[29] Wen-Jie Chen, Shao-Ji Jiang, Xiao-Dong Chen, Baocheng Zhu, Lei Zhou, Jian-Wen Dong, and C. T. Chan. Experimental realization of photonic topological insulator in a uniaxial metacrystal waveguide. *Nature Communications*, 5(1):1–7, December 2014.

[30] Xin-Tao He, En-Tao Liang, Jia-Jun Yuan, Hao-Yang Qiu, Xiao-Dong Chen, Fu-Li Zhao, and Jian-Wen Dong. A silicon-on-insulator slab for topological valley transport. *Nature Communications*, 10(1):872, February 2019.

[31] Robert J. Davis, Dia'aaldin J. Bisharat, and Daniel F. Sievenpiper. Classical-to-topological transmission line couplers. *Applied Physics Letters*, 118(13):131102, March 2021.

[32] R. J. Davis, D. J. Bisharat, and D. F. Sievenpiper. Efficient Transition from a Traditional Planar Transmission Line to a Topological Line Wave. In *2020 IEEE International Symposium on Antennas and Propagation and North American Radio Science Meeting*, pages 757–758, July 2020.

[33] Hui Feng Ma, Xiaopeng Shen, Qiang Cheng, Wei Xiang Jiang, and Tie Jun Cui. Broadband and high-efficiency conversion from guided waves to spoof surface plasmon polaritons. *Laser & Photonics Reviews*, 8(1):146–151, 2014.

[34] A. Kianinejad, Z. N. Chen, and C. Qiu. Design and Modeling of Spoof Surface Plasmon Modes-Based Microwave Slow-Wave Transmission Line. *IEEE Transactions on Microwave Theory and Techniques*, 63(6):1817–1825, June 2015.

[35] Zhixia Xu, Xiaoxing Yin, and Daniel F. Sievenpiper. Adiabatic Mode-Matching Techniques for Coupling Between Conventional Microwave Transmission Lines and One-Dimensional Impedance-Interface Waveguides. *Physical Review Applied*, 11(4):044071, April 2019.

[36] Gian Guido Gentili, Giuseppe Pelosi, Francesco S. Piccioli, and Stefano Selleri. Towards topological protection based millimeter wave devices. *Physical Review B*, 100(12), September 2019.

[37] Felix J. Lawrence, C. Martijn de Sterke, Lindsay C. Botten, R. C. McPhedran, and Kokou B. Dossou. Modeling photonic crystal interfaces and stacks: impedance-based approaches. *Advances in Optics and Photonics*, 5(4):385, December 2013.

[38] Dia'aaldin J. Bisharat and Daniel F. Sievenpiper. Electromagnetic-Dual Metasurfaces for Topological States along a 1D Interface. *Laser & Photonics Reviews*, 0(0):1900126, 2019.

[39] Alexander B. Khanikaev, S. Hossein Mousavi, Wang-Kong Tse, Mehdi Kargarian, Allan H. MacDonald, and Gennady Shvets. Photonic topological insulators. *Nature Materials*, 12(3):233–239, March 2013.

[40] Dia'aaldin J. Bisharat and Daniel F. Sievenpiper. Guiding Waves Along an Infinitesimal Line between Impedance Surfaces. *Physical Review Letters*, 119(10):106802, September 2017.

[41] S. A. R. Horsley and I. R. Hooper. One dimensional electromagnetic waves on flat surfaces. *Journal of Physics D: Applied Physics*, 47(43):435103, October 2014.

[42] Xianghong Kong, Dia'aaldin J. Bisharat, Gaobiao Xiao, and Daniel F. Sievenpiper. Analytic theory of an edge mode between impedance surfaces. *Physical Review A*, 99(3):033842, March 2019.

[43] Tzuhsuan Ma, Alexander B. Khanikaev, S. Hossein Mousavi, and Gennady Shvets. Guiding Electromagnetic Waves around Sharp Corners: Topologically Protected Photonic Transport in Metawaveguides. *Physical Review Letters*, 114(12):127401, March 2015.

[44] J.D.S. Langley, P.S. Hall, and P. Newham. Balanced antipodal Vivaldi antenna for wide bandwidth phased arrays. *Antennas and Propagation IEE Proceedings - Microwaves*, 143(2):97–102, April 1996.

[45] David M. Pozar. *Microwave Engineering*. Wiley, 4th edition, November 2011.

[46] R. J. P. Douville and D. S. James. Experimental Study of Symmetric Microstrip Bends and Their Compensation. *IEEE Transactions on Microwave Theory and Techniques*, 26(3):175–182, March 1978.

[47] Mehul P. Makwana and Richard V. Craster. Designing multidirectional energy splitters and topological valley supernetworks. *Physical Review B*, 98(23), December 2018.

[48] K. U-yen, E. J. Wollack, J. Papapolymerou, and J. Laskar. A Broadband Planar Magic-T Using Microstrip–Slotline Transitions. *IEEE Transactions on Microwave Theory and Techniques*, 56(1):172–177, January 2008.

[49] Xiaojun Cheng, Camille Jouvaud, Xiang Ni, S. Hossein Mousavi, Azriel Z. Genack, and Alexander B. Khanikaev. Robust reconfigurable electromagnetic pathways within a photonic topological insulator. *Nature Materials*, 15(5):542–548, May 2016.

[50] Rui Ting Yan, Hao Chi Zhang, Pei Hang He, Zheng Xing Wang, Xuanru Zhang, Xiaojian Fu, and Tie Jun Cui. A Broadband and High-Efficiency Compact Transition From Microstrip Line to Spoof Surface Plasmon Polaritons. *IEEE Microwave and Wireless Components Letters*, 30(1):23–26, January 2020.

[51] E. Hammerstad and O. Jensen. Accurate Models for Microstrip Computer-Aided Design. In *1980 IEEE MTT-S International Microwave symposium Digest*, pages 407–409, May 1980.

[52] D. Malterre, B. Kierren, Y. Fagot-Revurat, C. Didiot, F. J. García de Abajo, F. Schiller, J. Cordón, and J. E. Ortega. Symmetry breaking and gap opening in two-dimensional hexagonal lattices. *New Journal of Physics*, 13(1):013026, January 2011.

[53] Shreya Singh, Dia'aaldin Bisharat, and Dan Sievenpiper. Topological antennas: Aperture radiators, leaky-wave surfaces, and orbital angular momentum beam generation. *Journal of Applied Physics*, 130(2):023101, July 2021.

[54] Robert J. Davis and Daniel F. Sievenpiper. Robust Microwave Transport via Nontrivial Duality-Based Rhombic Unit Cells. In *2021 IEEE International Symposium on Antennas and Propagation and USNC-URSI Radio Science Meeting (APS/URSI)*, pages 619–620, December 2021.

[55] Liang Fu. Topological Crystalline Insulators. *Physical Review Letters*, 106(10):106802, March 2011.

[56] Feng Liu and Katsunori Wakabayashi. Novel Topological Phase with a Zero Berry Curvature. *Physical Review Letters*, 118(7), February 2017.

[57] Motohiko Ezawa. Higher-Order Topological Insulators and Semimetals on the Breathing Kagome and Pyrochlore Lattices. *Physical Review Letters*, 120(2):026801, January 2018.

[58] Xiang Ni, Matthew Weiner, Andrea Alù, and Alexander B. Khanikaev. Observation of higher-order topological acoustic states protected by generalized chiral symmetry. *Nature Materials*, 18(2):113–120, February 2019.

[59] Mengyao Li, Dmitry Zhirihin, Maxim Gorlach, Xiang Ni, Dmitry Filonov, Alexey Slobozhanyuk, Andrea Alù, and Alexander B. Khanikaev. Higher-order topological states in photonic kagome crystals with long-range interactions. *Nature Photonics*, 14(2):89–94, February 2020.

[60] Alexander Altland and Martin R. Zirnbauer. Nonstandard symmetry classes in mesoscopic normal-superconducting hybrid structures. *Physical Review B*, 55(2):1142–1161, January 1997.

[61] Shinsei Ryu, Andreas P. Schnyder, Akira Furusaki, and Andreas W. W. Ludwig. Topological insulators and superconductors: tenfold way and dimensional hierarchy. *New Journal of Physics*, 12(6):065010, June 2010.

[62] Frank Schindler, Ashley M. Cook, Maia G. Vergniory, Zhijun Wang, Stuart S. P. Parkin, B. Andrei Bernevig, and Titus Neupert. Higher-order topological insulators. *Science Advances*, June 2018.

[63] Chen Fang and Liang Fu. New classes of topological crystalline insulators having surface rotation anomaly. *Science Advances*, December 2019.

[64] Wenhui Fan, Simin Nie, Cuixiang Wang, Binbin Fu, Changjiang Yi, Shunye Gao, Zhicheng Rao, Dayu Yan, Junzhang Ma, Ming Shi, Yaobo Huang, Youguo Shi, Zhijun Wang, Tian Qian, and Hong Ding. Discovery of $${\hat{\boldsymbol{C}}}_2$$ rotation anomaly in topological crystalline insulator SrPb. *Nature Communications*, 12(1):2052, December 2021.

[65] Chen Fang, Matthew J. Gilbert, and B. Andrei Bernevig. Bulk topological invariants in noninteracting point group symmetric insulators. *Physical Review B*, 86(11), September 2012.

[66] Robert-Jan Slager, Andrej Mesaros, Vladimir Juričić, and Jan Zaanen. The space group classification of topological band-insulators. *Nature Physics*, 9(2):98–102, February 2013.

[67] Jorrit Kruthoff, Jan de Boer, Jasper van Wezel, Charles L. Kane, and Robert-Jan Slager. Topological Classification of Crystalline Insulators through Band Structure Combinatorics. *Physical Review X*, 7(4):041069, December 2017.

[68] Feng Tang, Hoi Chun Po, Ashvin Vishwanath, and Xiangang Wan. Comprehensive search for topological materials using symmetry indicators. *Nature*, 566(7745):486–489, February 2019.

[69] Feng Tang, Hoi Chun Po, Ashvin Vishwanath, and Xiangang Wan. Efficient topological materials discovery using symmetry indicators. *Nature Physics*, 15(5):470–476, May 2019.

[70] Marcos Atala, Monika Aidelsburger, Julio T. Barreiro, Dmitry Abanin, Takuya Kitagawa, Eugene Demler, and Immanuel Bloch. Direct measurement of the Zak phase in topological Bloch bands. *Nature Physics*, 9(12):795–800, December 2013.

[71] Jin-Kyu Yang, Yongsop Hwang, and Sang Soon Oh. Evolution of topological edge modes from honeycomb photonic crystals to triangular-lattice photonic crystals. *Physical Review Research*, 3(2):L022025, June 2021.

[72] Dia'aaldin Bisharat and Dan Sievenpiper. Valley polarized edge states beyond inversion symmetry breaking, January 2023.

[73] Yun Zhou, Naiqing Zhang, Dia'aaldin J. Bisharat, Robert J. Davis, Zichen Zhang, James Friend, Prabhakar R. Bandaru, and Daniel F. Sievenpiper. On-Chip Unidirectional Waveguiding for Surface Acoustic Waves along a Defect Line in a Triangular Lattice. *Physical Review Applied*, 19(2):024053, February 2023.

[74] Feng Liu, Hai-Yao Deng, and Katsunori Wakabayashi. Topological photonic crystals with zero Berry curvature. *Physical Review B*, 97(3), January 2018.

[75] Robert J. Davis, Yun Zhou, Dia'aaldin J. Bisharat, Prabhakar R. Bandaru, and Daniel F. Sievenpiper. Topologically protected edge states in triangular lattices. *Physical Review B*, 106(16):165403, October 2022.

[76] Jian Li, Alberto F. Morpurgo, Markus Büttiker, and Ivar Martin. Marginality of bulk-edge correspondence for single-valley Hamiltonians. *Physical Review B*, 82(24):245404, December 2010.

[77] E. Dobardžić, M. Dimitrijević, and M. V. Milovanović. Generalized Bloch theorem and topological characterization. *Physical Review B*, 91(12):125424, March 2015.

[78] Erda Wen, Dia'aaldin J. Bisharat, Robert J. Davis, Xiaozhen Yang, and Daniel F. Sievenpiper. Designing Topological Defect Lines Protected by Gauge-Dependent Symmetry Indicators. *Physical Review Applied*, 17(6):064008, June 2022.

[79] E. Lidorikis, M. M. Sigalas, E. N. Economou, and C. M. Soukoulis. Tight-Binding Parametrization for Photonic Band Gap Materials. *Physical Review Letters*, 81(7):1405–1408, August 1998.

[80] J. P. Albert, C. Jouanin, D. Cassagne, and D. Bertho. Generalized Wannier function method for photonic crystals. *Physical Review B*, 61(7):4381–4384, February 2000.

[81] Jacques Des Cloizeaux. Orthogonal Orbitals and Generalized Wannier Functions. *Physical Review*, 129(2):554–566, January 1963.

[82] Xianghong Kong, Yun Zhou, Gaobiao Xiao, Daniel F. Sievenpiper, Yun Zhou, Gaobiao Xiao, Gaobiao Xiao, Daniel F. Sievenpiper, and Daniel F. Sievenpiper. Spin-momentum locked modes on anti-phase boundaries in photonic crystals. *Optics Express*, 28(2):2070–2078, January 2020.

[83] Z. F. Wang, Kyung-Hwan Jin, and Feng Liu. Quantum spin Hall phase in 2D trigonal lattice. *Nature Communications*, 7(1):12746, November 2016.

[84] Wladimir A. Benalcazar, B. Andrei Bernevig, and Taylor L. Hughes. Electric multipole moments, topological multipole moment pumping, and chiral hinge states in crystalline insulators. *Physical Review B*, 96(24):245115, December 2017.

[85] Michael Tinkham. *Group Theory and Quantum Mechanics*. Dover, December 2003.

[86] Cristina Bena and Gilles Montambaux. Remarks on the tight-binding model of graphene. *New Journal of Physics*, 11(9):095003, September 2009.

[87] J. Zak. Band representations of space groups. *Physical Review B*, 26(6):3010–3023, September 1982.

[88] Hoi Chun Po. Symmetry indicators of band topology. *Journal of Physics: Condensed Matter*, 32(26):263001, April 2020.

[89] Jiewen Xiao and Binghai Yan. First-principles calculations for topological quantum materials. *Nature Reviews Physics*, 3(4):283–297, April 2021.

[90] Christopher Bradley and Arthur Cracknell. *The Mathematical Theory of Symmetry in Solids: Representation Theory for Point Groups and Space Groups*. Oxford University Press, Oxford, revised ed. edition edition, February 2010.

[91] Mildred S. Dresselhaus, Gene Dresselhaus, and Ado Jorio. *Group Theory: Application to the Physics of Condensed Matter*. Springer, Berlin, 2008th edition edition, December 2007.

[92] Thomas Christensen, Hoi Chun Po, John D. Joannopoulos, and Marin Soljačić. Location and Topology of the Fundamental Gap in Photonic Crystals. *Physical Review X*, 12(2):021066, June 2022.

[93] Yun Zhou, Robert J. Davis, Li Chen, Erda Wen, Prabhakar R. Bandaru, and Daniel F. Sievenpiper. Helical Phononic Modes Induced by a Screw Dislocation. *In preparation*, 2023.

[94] Ying Ran, Yi Zhang, and Ashvin Vishwanath. One-dimensional topologically protected modes in topological insulators with lattice dislocations. *Nature Physics*, 5(4):298–303, April 2009.

[95] Qiang Wang, Yong Ge, Hong-xiang Sun, Haoran Xue, Ding Jia, Yi-jun Guan, Shou-qi Yuan, Baile Zhang, and Y. D. Chong. Vortex states in an acoustic Weyl crystal with a topological lattice defect. *Nature Communications*, 12(1):3654, June 2021.

[96] Eran Lustig, Lukas J. Maczewsky, Julius Beck, Tobias Biesenthal, Matthias Heinrich, Zhaoju Yang, Yonatan Plotnik, Alexander Szameit, and Mordechai Segev. Photonic topological insulator induced by a dislocation in three dimensions. *Nature*, 609(7929):931–935, September 2022.

[97] Peiheng Zhou, Gui-Geng Liu, Xin Ren, Yihao Yang, Haoran Xue, Lei Bi, Longjiang Deng, Yidong Chong, and Baile Zhang. Photonic amorphous topological insulator. *Light: Science & Applications*, 9(1), December 2020.

[98] Zhixia Xu, Xianghong Kong, Robert J. Davis, Dia'aaldin Bisharat, Yun Zhou, Xiaoxing Yin, and Daniel F. Sievenpiper. Topological valley transport under long-range deformations. *Physical Review Research*, 2(1):013209, February 2020.

[99] Miguel A. Bandres, Mikael C. Rechtsman, and Mordechai Segev. Topological Photonic Quasicrystals: Fractal Topological Spectrum and Protected Transport. *Physical Review X*, 6(1):011016, February 2016.

[100] Ai-Lei He, Lu-Rong Ding, Yuan Zhou, Yi-Fei Wang, and Chang-De Gong. Quasicrystalline Chern insulators. *Physical Review B*, 100(21), December 2019.

[101] Tianhe Li, Penghao Zhu, Wladimir A. Benalcazar, and Taylor L. Hughes. Fractional disclination charge in two-dimensional ${C}_{n}$-symmetric topological crystalline insulators. *Physical Review B*, 101(11):115115, March 2020.

[102] Yang Liu, Shuwai Leung, Fei-Fei Li, Zhi-Kang Lin, Xiufeng Tao, Yin Poo, and Jian-Hua Jiang. Bulk-disclination correspondence in topological crystalline insulators. *Nature*, 589(7842):381–385, January 2021.

[103] Max Geier, Ion Cosma Fulga, and Alexander Lau. Bulk-boundary-defect correspondence at disclinations in rotation-symmetric topological insulators and superconductors. *SciPost Physics*, 10(4):092, April 2021.

[104] Raffaello Bianco and Raffaele Resta. Mapping topological order in coordinate space. *Physical Review B*, 84(24), December 2011.

[105] Noah P. Mitchell, Ari M. Turner, and William T. M. Irvine. Real-space origin of topological band gaps, localization, and reentrant phase transitions in gyroscopic metamaterials. *Physical Review E*, 104(2):025007, August 2021.

[106] Qiang Wang, Haoran Xue, Baile Zhang, and Y. D. Chong. Observation of Protected Photonic Edge States Induced by Real-Space Topological Lattice Defects. *Physical Review Letters*, 124(24):243602, June 2020.

[107] Ruichao Ma, Clai Owens, Aman LaChapelle, David I. Schuster, and Jonathan Simon. Hamiltonian tomography of photonic lattices. *Physical Review A*, 95(6), June 2017.

[108] Nathan Schine, Michelle Chalupnik, Tankut Can, Andrey Gromov, and Jonathan Simon. Electromagnetic and gravitational responses of photonic Landau levels. *Nature*, 565(7738):173–179, January 2019.

[109] M. D. Caio, G. Möller, N. R. Cooper, and M. J. Bhaseen. Topological marker currents in Chern insulators. *Nature Physics*, 15(3):257–261, March 2019.

[110] Zheng Wang, Y. D. Chong, John D. Joannopoulos, and Marin Soljačić. Reflection-Free One-Way Edge Modes in a Gyromagnetic Photonic Crystal. *Physical Review Letters*, 100(1):013905, January 2008.